5-2016

A Characterization Study on Catalyst Layers in Proton Exchange Membrane Fuel Cells

Luyue Li
The University of Tennessee, Knoxville, lli31@vols.utk.edu

To the Graduate Council:

I am submitting herewith a dissertation written by Luyue Li entitled "A Characterization Study on Catalyst Layers in Proton Exchange Membrane Fuel Cells." I have examined the final electronic copy of this dissertation for form and content and recommend that it be accepted in partial fulfillment of the requirements for the degree of Doctor of Philosophy, with a major in Chemical Engineering.

Thomas A. Zawodzinski, Major Professor

We have read this dissertation and recommend its acceptance:

Robert M. Counce, Alexander B. Papandrew, Matthew M. Mench

Accepted for the Council:

Carolyn R. Hodges

Vice Provost and Dean of the Graduate School

(Original signatures are on file with official student records.)

A Characterization Study on Catalyst Layers in Proton Exchange Membrane Fuel Cells

A Dissertation Presented for the
Doctor of Philosophy
Degree
The University of Tennessee, Knoxville

Luyue Li

May 2016

Acknowledgements

I would like to express my most sincere gratitude to Dr. Thomas Zawodzinski for his support, patience and guidance throughout my entire graduate school. I would like to thank Dr. Matthew Mench, Dr. Robert Counce and Dr. Alexander Papandrew for serving on my committee and giving me valuable advice towards my research. I also want to express my appreciation to Dr. Karren More and Dr. Shawn Reeves from ORNL for assisting me with my microscopic experiments. Thanks to 3M Company for proving the ionomer and catalyst samples.

Special thanks to Nelly Cantillo for co-researching on the 3M materials and to the entire research group from the University of Tennessee, it has been my privilege working amongst you. Especially Dr. Che-Nan Sun, Dr. Gabriel Goenaga, Dr. Zhijiang Tang and Dr. Yujia Bai for their countless experimental guidance.

I would like to thank my parents for their endless support. And finally, my dear husband Nick, for always being by my side and making everywhere feel like home.

Abstract

This thesis describes the work for the catalyst layer (CL) characterization study of proton exchange membranes (PEM) for fuel cells. In particular, both the structure and performance of catalyst layers with alternative ionomers were studied. Structure wise, the morphology, surface area and pore size distribution studies were accomplished with scanning electron microscopy (SEM), transmission electron microscope (TEM) and nitrogen adsorption processed through Brunauer–Emmett–Teller (BET) and Barrett-Joyner-Halenda (BJH) theory. Water uptake isotherms of the CLs have been developed under well controlled relative humidity (RH) levels. The performance characterization focuses on polarization study, catalyst layer proton conductivity measurement and estimation of the proton conduction tortuosity. Also, a thermal investigation between various components of the catalyst layer was performed.

Two different sets of CLs were examined, the in-house fabricated 3M ionomer CLs and free-standing 3M CLs directly provided from the 3M Company. A characteristic comparison of the structure and electrochemical performance have been carried out, along with further discussion on the formation of CLs containing 3M polytetrafluoroethylene (PTFE) ionomer.

Our data revealed that higher ionomer to carbon (I/C) ratio reduced the amount of micro- , meso- and macropores. This allowed the construction of a more completely developed ionic transport network, however, could potentially hinder the mass transfer. Also, our study showed that higher Pt:C ratio lead to a more intense Pt agglomeration. The

CL's porosity was strongly affected by such Pt clustering. Furthermore, energy dispersive X-ray analysis (EDS) revealed that the 3M ionomer preferred attaching to the carbon surface over the Pt particles.

According to our polarization study, in contrast of tradition Nafion fuel cells, the 3M fuel cells reached its optimal performance at 60%-70% RH and suffered dramatic mass transfer losses at saturated humidity level. Therefore, the 3M fuel cells are able to function fully under drier conditions than the Nafion units. However, the high sensitivity on the cells' water content requires efficient water management during operation, especially at higher current density. Polarization study also showed an optimal 3M ionomer loading of 36 wt.% at 30:70 Pt:C ratio, which is similar to traditional Nafion fuel cells.

Table of Contents

List of Tables

List of Figures

Chapter 1

Introduction and Literature Review

1.1 Fuel Cell Basics

A fuel cell is a device that converts chemical energy from a fuel, e.g., hydrogen and methanol into electricity. It is one of the most promising clean energy sources for residential and industrial power supply or backup, since there is no pollutant generated, unlike a combustion engine. The fuel cell operates at a significantly lower temperature at high efficiency because it uses a direct conversion of chemical to electrical energy. The fuel cell was invented in 1838 by W.R. Grove [1]. A simple fuel cell is shown in Figure 1.1. During the cell operation, the hydrogen combustion reaction can be divided into two half reactions:

$$H_2 \rightleftharpoons 2H^+ + 2e^-$$

$$\frac{1}{2}O_2 + 2H^+ \rightleftharpoons 2e^- + H_2O$$

The electrolyte keeps these two reactions apart so they occur separately. Electrolyte is a substance that only allows ions to cross through and blocks the electrons. The different kinds of electrolytes distinguish fuel cells into different types, e.g., polymer electrolyte membrane fuel cells (PEMFC), alkaline fuel cells and solid oxide fuel cells (SOFC). In this study, the PEMFC is our main focus.

As shown in Figure 1.1, the resistance throughout the electrolyte is high because of the long distance between the two electrodes and the small contact area between the electrolyte and electrode. To resolve this problem, in a typical fuel cell design, two highly porous electrodes are separated with a thin membrane which cuts down the internal resistance. The porous electrodes also allow gas transport to a catalyst within the structure.

A schematic of a single cell hydrogen/oxygen fuel cell is shown in Figure 1.2. It consists of feeding channels, diffusion layers, catalyst layers and a membrane. The sandwich-like structure compact unit which includes the anode/cathode catalyst layers and membrane is known as the membrane electrode assembly (MEA). The MEA is the heart of fuel cell. During operation, hydrogen and oxygen are constantly being pumped into the system, and through means of an electrochemical reaction, electricity, heat and byproducts are produced. In a hydrogen/oxygen fuel cell, hydrogen is continuously pumped through the anode side while oxygen is supplied through the cathode side. In the anode catalyst layer, the hydrogen splits into a proton and an electron, each taking a different path to the cathode. The electron travels through the outer circuit while the proton crosses through the proton exchanging membrane. After the electron and proton reunite in the cathode, they react with oxygen into water. Theoretically, the cell will never run out of power as long as the fuel is fed.

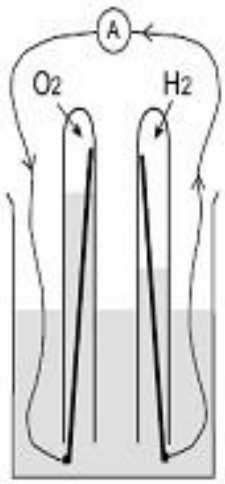

Figure 1.1 Simple Fuel Cell Device [2]

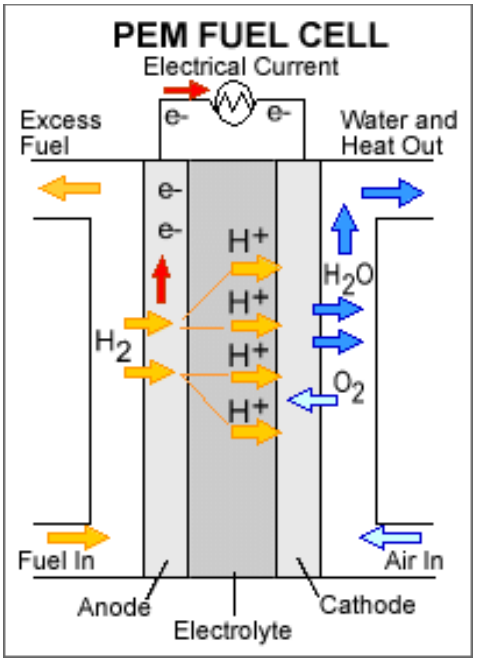

Figure 1.2 Single Cell Hydrogen/Oxygen Fuel Cell [3]

1.2 Fuel Cell Types

As mentioned above, according to the different kinds of electrolytes used, fuel cells can be divided into various types.

1.2.1 Alkaline Fuel Cells (AFC)

Alkaline fuel cells use potassium hydroxide as the electrolyte and compressed hydrogen and oxygen as fuel. The potassium hydroxide solution circulates in the cell, this can block the gas leak and also act as a coolant for the cell. The purity of the fuel is crucial to the cell's performance since the electrolyte is extremely sensitive to the presence of carbon dioxide:

$CO_2+2OH^- \rightarrow (CO_3)^{2-}+H_2O$

The carbonate that forms can precipitate out to block pores in the electrode or the electrolyte pathways [4]. The circulation of the electrolyte solution can prevent such a reaction to some degree.

AFCs have inherently faster kinetics on many metals than do fuel cells using acid conditions, allowing the use of non-precious metals as the catalyst in the cathode. The reactions inside an AFC are shown below:

Anode: $H_2+2OH^- \rightarrow 2H_2O+2e^-$

Cathode: $1/2O_2+2e^-+H_2O \rightarrow 2OH^-$

As shown above, the anode produces twice the amount of water than that used in the cathode. If not removed efficiently, the water can dilute the electrolyte solution or flood the electrode and cause a decrease in the performance.

Because of its fairly high power density, long durability and relatively low cost, AFCs were greatly favored in the 1970s and 1980s. However, due to the rapid development of proton exchange membrane fuel cells, studies on AFCs have stagnated [5].

1.2.2 Molten Carbonate Fuel Cell (MCFC)

Molten Carbonate Fuel Cells use a potassium or lithium molten salt, or a combination of alkali carbonates, impregnated in a ceramic matrix. MCFCs work at a higher temperature of 650°C, under which conditions carbon monoxide will not poison the electrode but can even be used as fuel. Hydrogen, natural gas, propane and coal gasification products are also candidates as fuel source. The reactions inside the cell are shown below:

Anode: $H_2+CO_3^{2-} \rightarrow CO_2+H_2O+2e^-$

Cathode: $1/2O_2+CO_2+2e^- \rightarrow CO_3^{2-}$

As shown, during operation, carbon dioxide is produced in the anode and consumed in the cathode. Nickel usually is used as a catalyst in MCFCs, which makes catalysts costs less expensive than for platinum used in most other kinds of fuel cells. MCFCs can be used as small scale power supply units, typical MCFCs have a 90% efficiency when both the electricity and heat are utilized [6].

1.2.3 Phosphoric Acid Fuel Cell (PAFC)

One of the first-commercialized fuel cells, phosphoric acid fuel cells, use liquid phosphoric acid as electrolyte. The cathodes in PAFCs usually consist of a silicon carbide structure with platinum dispersed in between. Such a structure can contain the phosphoric acid electrolyte from mixing with the fuel [7]. The reaction inside a PAFC is given below：

Anode: $H_2 \rightarrow 2H^+ + 2e^-$

Cathode: $1/2O_2 + 2H^+ + 2e^- \rightarrow H_2O$

The cell operation temperature is between 180°C-210°C to keep the phosphoric acid stability, though the low end of this range is favored to minimize effects of carbon support corrosion. PAFCs are the most commercialized and mature type of fuel cell at present. However, there are several issues concerning this type of cells, such as the high cost of platinum, electrode poisoning from carbon monoxide and evaporation of the phosphoric acid during operation [6].

1.2.4 Solid Oxide Fuel Cells (SOFC)

Solid oxide fuel cells usually use non-corrosive metal oxide ceramic as electrolyte, such as ytria stabilized zirconia [8]. They operate at a fairly high temperature of 800-1000°C, and the cell voltage and efficiency of such cells are very temperature sensitive [9]. The reactions inside a SOFC are shown below:

Anode: $H_2 + O^{2-} \rightarrow H_2O + 2e^-$

Cathode: $1/2O_2+2e^- \rightarrow O^{2-}$

Unlike PEMFC, water is produced in the anode instead of the cathode. The materials used for the anode and cathode are different: the typical anode consists of nickel zirconia while the cathode is made of magnesium or strontium doped lanthanum manganite [10]. Due to the high operation temperature, the cells are more tolerant to carbon monoxide poisoning compared to low temperature fuel cells. There are various choices to use as fuel for SOFCs, such as coal, natural gas, alcohols and even carbon monoxide. The electrical efficiency of SOFCs are 50%-60%, but when the heat is also utilized, the total efficiency can reach 90% [6].

1.2.5 Proton Exchange Membrane Fuel Cell (PEMFC)

The PEMFC is considered a promising clean energy technology in the twenty-first century. A PEMFC is a fuel cell that uses a proton exchange membrane as the separator to keep the anode and cathode apart. The most common membrane for PEMFCs uses tetrafluoroethylene based fluoropolymer-copolymers, such as Nafion and Flemion. The reactions inside a PEMFC are shown below:

Anode: $H_2 \rightarrow 2H^+ + 2e^-$

Cathode: $1/2O_2+2H^+ + 2e^- \rightarrow H_2O$

Other than using hydrogen as fuel, methanol and formic acid can also be applied as fuel in PEMFCs with lower output power [8]. The PEMFC operation temperature is kept below 90°C because the membrane has to be humidified at a high level. Due to the low operation

temperature, so far platinum is the only promising catalyst. Pt is a limited resource and very costly. There are several advantages of PEMFCs compared to other types of energy-producing technologies: no mobile parts, higher efficiency and no emissions of polluting gases such as CO, CO_2, SO_x [11]. However, the high cost of the proton exchange membrane and platinum is the main disadvantage and the main focus of PEMFC studies.

1.3 Proton Exchange Membrane (PEM)

PEM fuel cells have attracted much attention due to its solid electrolyte, which enables utilization in transportation systems and portable electronic systems [12]. The proton exchange membrane is a solid electrolyte that transfers the proton from anode to cathode and separates the two from contacting each other. According to previous studies [8][13], this solid polymer membrane should have good isolation against electronic current while providing high proton conductivity. Also, it needs to be mechanically and chemically stable at harsh temperature and humidity levels. DuPont's Nafion is a commonly used membrane in the fuel cell industry. Its stability in performance, low gas permeability, high proton conductivity and good availability makes it one of the most competitive membranes on the market. However, like most of the perfluorinated proton exchange membranes, Nafion needs to be fully humidified during cell operation to supply a sufficient proton conductivity. This limits the cell operation temperature to be below 100°C, which demands more platinum to be used as catalyst in the system. There is considerable interest in finding an alternative membrane and extending the PEMs' durability. The chemical structure of perfluorosulfic polymer electrolyte is shown in Figure 1.3. As shown, the polymer has a Teflon-like flouoro 3, 6-dioxo 4, 6-octane sulfonic acid with PTFE backbone. This

backbone structure gives the polymer a partly hydrophobic nature while the SO_3H groups in the side chain are hydrophilic. In Nafion, m≥1, n=2, x=5-13.5, y=1000. Meanwhile there are other polymer membranes from other manufacturers with shorter sidechains and higher SO_3H to CF_2 group ratio. For example, the Dow Chemical Company synthesized a perfluorosulfic membrane where m=0, n=2, x=3.6-10; Asahi Chemical Company produced a perfluorosulfic membrane Flemion where m=0/1, n=1-5 [11, 14, 15]. The polar side chains have shown to form ionic aggregates amongst the more nonpolar backbones. Such behavior lead to a complex membrane structure comprised of hydrophilic sulfuric domains dispersed inside the semi-crystalline, hydrophobic backbone matrix [16-18].

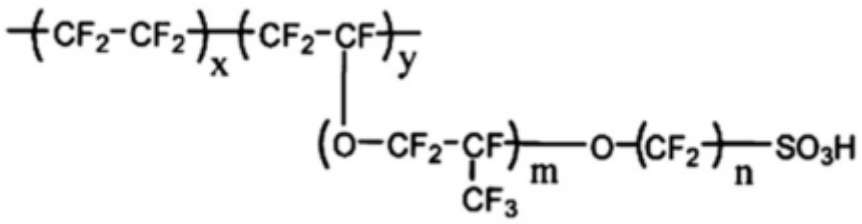

Figure 1.3 Chemical structure of perfluorosulfic polymer electrolyte

The PEM proton conductivity is affected by the extent of cell humidity and the thickness. Higher proton conductivity is usually achieved at higher humidity level. A thinner membrane lowers the water requirements for the membrane hydration and cuts down cost and membrane resistance. T. E. Springer et al. [19] demonstrated theoretically and experimentally that the decrease in membrane thickness can alleviate membrane resistance problems. This study indicated that the decrease of the membrane thickness reduces the membrane resistance in a non-linear fashion. Also, with thinner membranes, the electrodes tend to stay humidified during operation, resulting in some performance benefits.

However, thinner membranes do face durability and fuel crossover challenges. An early attempt was made in this thesis work to study the behavior of a MEA with an ultra-thin (1-10μm) proton exchange membrane. However, the high quality requirement for the preparation of such MEAs hindered progress.

1.4 Catalyst Layer (CL) in PEMFC

One important challenge for PEMFC design is the catalyst layer. A typical CL consists of a porous matrix of Pt/carbon particles and an ionomer network amongst the pores. A successful CL design should allow a high rate of selective (4 e^-) reaction with a minimal amount of catalyst used. Due to the low rate of oxygen reduction reaction (ORR) in the cathode, compared to the hydrogen oxidation reaction (HOR) on the anode side, the cathode CL design attracts more attention. In this section, the impact and function of the CL will be discussed.

Even though many studies have been carried out on PEMFC, the detail of the complex and heterogeneous microstructure of the CLs or the interfacial bonding layer between the CL and PEM is still an important topic for study. A better understanding of the connection between the catalyst layer structure and the fuel cell performance can provide insight into controlling the structure to optimize the cell performance. The typical catalyst layer contains a thin layer of recast ionomer around the carbon and platinum agglomerations. To introduce a distribution of these components in the CL ink, additives are commonly used during the CL ink preparation. There are three main transport processes inside the catalyst layer:

1. Protons between the electrode and membrane;
2. Electrons between the catalyst layer and the current collector;
3. The product and reactant gas between the catalyst layer and the fuel/air channel [20].

A simplified schematic of an ideal three-phased-boundary (TPB) is shown in Figure 1.4, formed by the proton, electron and gas inside the catalyst layer. This model has been widely employed in the study of PEMFCs. In many recent studies, the idea of such an ideal TPB structure throughout the CL has been proven to be unrealistic [21-24]. Instead, it is considered that TPB zones are distributed in the CL. The structural and chemical properties of the TPBs are related to the reaction and diffusion processes, and depend on the interplay amongst the individual components in the CL ink.

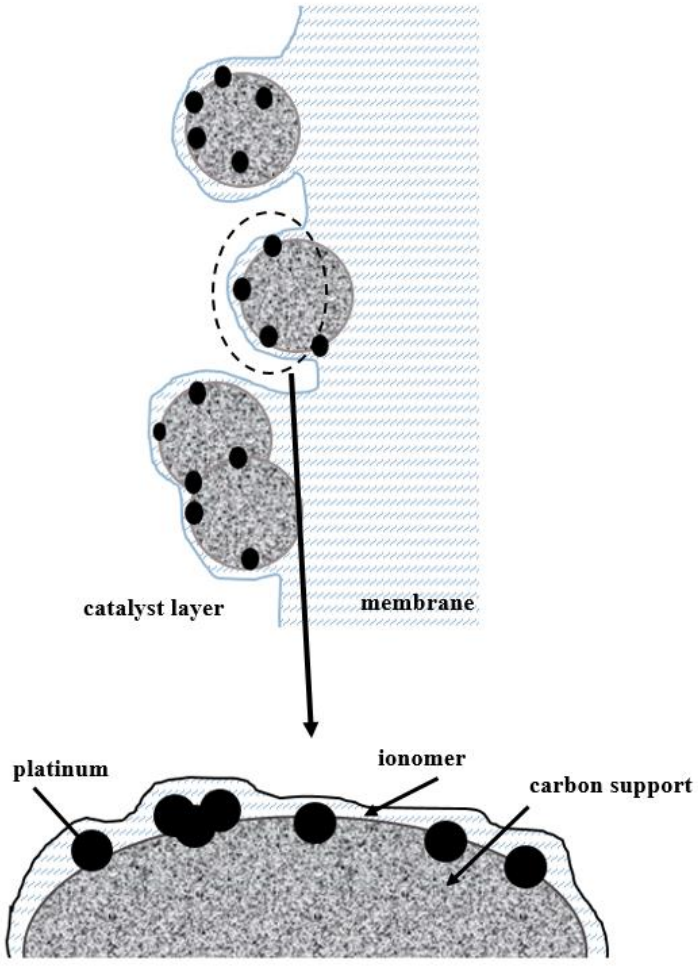

Figure 1.4 Three-phase-boundary structure inside the catalyst layer

There are several points to be considered when it comes to designing an effective PEMFC CL: (1) ensuring a large three phase area; (2) providing a sufficiently high proton conductivity allowing the protons to transport to the reaction sites; (3) constructing an efficient pathway for the reactant gas transport and produced water removal; (4) assuring a continuous electronic passage between the current collectors and reaction sites [25].

One of the drawbacks of PEM fuel cells is the high cost of Pt. In fact, the U.S. department of energy have set a goal to reduce the Pt loading to 0.05mg/cm^2 in a 50KW fuel cell stack [26]. In early studies, the conventional cathode Pt loading is around 4mg/cm^2, but a vast amount of research has been carried out to reduce the Pt level required in the CL [26-30]. Through novel sputtering techniques, Pt loading as low as 0.014mg/cm^2 has been reported [26, 29].

Studies regarding the CL microstructure have been widely reported. Uchida *et. al.*[31] discussed how the microstructures of the carbon supports can affect the performance of the PEMFC. His study provided novel insight on the ionomer distribution inside the porous structure of the CL, addressing that PTFE is mainly presence in the secondary pores (>40nm). Wei *et. Al.*[32] investigated the CL microstructure using a random cluster model. His results showed that a proper Pt: C: Nafion ratio is required to maximize the Pt utilization, and overall, lower Pt:C ratio is especially sensitive to the change in ionomer loading. Farhat's model [33] suggested that a reduction in Pt particle size could significantly increase the cell performance. Indeed, it was predicted that, based on the same Pt loading per geometric area, using 1nm size Pt particles attained an exchange current density that was three orders of magnitude higher than that of 1μm Pt particles.

The preparation method of the CL can greatly affect the formation and performance of the CL. Typical reported CL preparation methods include painting, spraying, rolling and screen printing [25]. M.S. Wilson [34] first introduced the fabrication of a thin film CL which is commonly used today. The CL was prepared by mixing Pt/C, Nafion solution and glycerol and sonicated overnight. The ink was then simply brush-painted onto a clean Teflon backing to the required Pt loading. This thin film CL was then hot pressed onto the proton exchanging membrane. Compared to the preparations of MEAs, this method significantly dropped the Pt loading and allowed the formation of a large three-phase binding area. The brush painting technique however has its own disadvantages, such as the difficulty in controlling the uniformity, its time consuming and the effect of the uptake of ink and solution onto the brush. These factors limit the reproducibility of the brush-painted MEAs. Bender et al. [35] introduced the utilization of the doctor's blade method [36] to screen print the catalyst ink onto the substrate. This process better homogenizes the paint distribution and is less time assuming for large scale CL fabrication. However, this method is less suitable for laboratory scale operation due to the large demand in ink material. Spray painting is another technique that can provide a more evenly distributed CL and is less time consuming compared to the brush-painting method [37]. This process can be easily automated and requires as little as an air pressure line and a spray gun. Since then, different fabrication methods have been introduced. Xu et al. [38] introduced sulfonic acid groups onto the surface of carbon particles and greatly reduced the Nafion content and resistance. Morikawa et al. [39] reported the utilization of electrophoretic deposition (EPD) in CL fabrication. Using this method, the thickness of the CL can be strictly controlled by

changing the concentration of the ionomer ink. Fernandez et al. [40] reported on the influence of the solution used in the catalytic ink on the CL microstructure. His study showed that the ink deposition process was affected by the physical properties of the ink such as viscosity and boiling point. For the in-house fabricated 3M ionomer CLs, the spray painting method was utilized.

The effect of ionomer loading inside the CL has also been investigated. E. Passalacqua et al. [41] studied the effect of Nafion content on structure and performance of the PEFC catalyst layers. The optimum Nafion loading was reported to be 33 wt%. The study suggested that at lower Nafion content, the lack of continuous ionomer structure prohibited the ionic conduction. Yet when the Nafion loading was too high, the excess ionomer content can obstruct the electronic pathway and block the gas diffusion. Xie et al. [42] reported 27±6% wt. % was the optimized Nafion content for cathode catalyst layer with E-TEK carbon and a 0.2 mg/cm^2 loading. Higher ionomer loading resulted in smaller carbon aggregate size and a thicker layer of Nafion film covering the aggregates.

Another factor that affects the fuel cell performance is the thermal stability of the CLs. Carbon is most commonly used as a catalyst support in the CL because it enables a good dispersion of the Pt, provides electronic continuity and possesses good physical and chemical stability. However, one issue with the carbon support is that, at higher temperature and overpotential, carbon can corrode with the presence of Pt [43]. This can cause the structure destruction and Pt detachment. Baturina et al. [44] reported a decrease in the onset decomposition temperature when Pt is introduced to Vulcan XC 72 carbon. (400°C vs. 700°C). Samms et al. [45] reported that the Pt also lowers the decomposition

temperature of Nafion by 40°C. The consensus is a higher graphitization of carbon provides better resistance against oxidation and carbon corrosion. However, it is more challenging to support metal onto the more graphitized structure [46].

The physical properties of the carbon support can also influence the electrochemical performance of the CL. One important requirement of the carbon support is a high surface area, since it enables uniform dispersion of the Pt nanoparticles [47]. A proper dispersion of the Pt particles makes lower Pt loading feasible for fuel cell operation. Besides high surface area, the carbon support should also have a high chemical stability. This is to limit the carbon corrosion in the presence of oxygen and Pt, which becomes more crucial under elevated temperature and higher operating potential [48]. Some of the commonly used carbon supports for metal catalysis are activated carbon, carbon black, graphite and other graphitized material [49]. Carbon blacks were almost used exclusively until the 1990s [50] when novel carbon was being developed. A large amount of work has been devoted to the effect of carbon support on the Pt dispersion. McBreen et al. [51] evaluated the dispersion of Pt on five different kinds of carbon supports with widely varying chemical and physical properties. His results showed that carbon with high volatile content and acidic pH inhibited the metal dispersion. On the opposite side, high internal porosity and certain Pt-C interactions can improve the distribution. Rao et al. [52] studied the carbon material in the Sibunit family as a support for anode catalyst of direct methanol fuel cells. He calculated the Pt utilization factor by dividing the electrochemically active surface area (EASA) by the total metal surface area (TSA). The former was determined from the CO stripping using cyclic voltammetry (CV) while the latter was derived from the amount of CO chemisorbed

from the gas phase. According to his results, PtRu nanoparticles showed an increase in utilization as the BET total surface area of the carbon support decreased. Such behavior was explained to be due to the compatibility between the size of pores in the carbon supports and Nafion micelles. To be more specific, pores with diameter smaller than 20nm have a detrimental effect on the specific activity of PtRu/C. A higher amount of these pores lead to a lower specific activity of PtRu, since these pores were considered to be too small for the Nafion micelles to reach. Therefore, the uncovered metal particles could not take part in the CO stripping during CV. Rodrigues-Reinoso et al. [53] found that the dispersion of Pt particles increased linearly with the increase of 9-11nm mesopores in the activated carbon. Another factor that can affect the Pt dispersion is the chemical nature of the carbon surface [54]. In fact, many researchers recognized that the properties of the catalyst is not merely affected by its porosity but also by surface functional groups [55-58]. Prado-Burguete et al. [56, 57] investigated the influence of oxygen surface groups on the Pt dispersion. His study showed that the introduction of oxygen groups made the carbon surface more hydrophilic, thereby making the surface more accessible to the aqueous solution during impregnation.

Furthermore, the nanostructure of the ionomer in the bulk membrane, thin film and solution have been widely studied. In the membrane, the ionic groups was reported to cluster in a reverse micelles structure connected by small channels [59]. Rubatat et al. [60] described Nafion as elongated polymer aggregates connected together to form the membrane which would separate during the water swelling process. For the ionomer solution, Nafion adopts a rod-like structure. The hydrophobic backbones form the core of

the rod and the sulfonic groups are located on the end of the pendant chains facing outwards [60-63]. Ngo [61] investigated the influence of the isopropyl alcohol (IPA) content in the ionomer solution on the recast ionomer formation over the Pt/C aggregates. Transmission electron microscope (TEM) images showed that the Nafion adopted a coil-like structure when the IPA concentration is above 70wt%. Ngo concluded that lower IPA/water content in the Pt/C/Nafion ink would result into a thinner ionomer film over the Pt and carbon particles, enhancing the cell performance.

Since the nanostructure of the CL is complex and sub-micron-scale, direct measurement of transport resistances inside the CL can be challenging. Therefore, modeling is an effective tool to further investigate the transport of reactant gas, water, electrons and protons. The agglomerate model is commonly used to represent the CL, in which the agglomerate particles consist of Pt/C particles and ionomer surrounding the agglomerates. To fit the experimental data, different studies had to assume various agglomerate sizes ranging from 100 nm to 2000 nm with various ionomer film thicknesses ranging from 10 to 100nm [64-70]. However, such a wide range of agglomerate sizes and ionomer film thicknesses may not be physically correct in reality [71]. For example, Greszler et al. [72] used a simple agglomeration model with bulk-like ionomer resulting in an agglomeration size of 380nm and ionomer film thickness of 20nm. This assumed structure was not observed under microscopic images. Epting et al. [73] demonstrated the importance of an agglomerate size distribution in the agglomeration models. By comparing the model-derived and the nanoscale X-ray computed tomography (nano-CT) measured agglomeration sizes, Epting found a substantial error when assuming a single agglomerate

size throughout the CL. A more in-depth model is certainly required for a more accurate CL analysis.

In conclusion, the combination of microstructure and electrochemical studies can provide us with much valuable insight on the CL functionality. In hope of controlling the Pt/C/ionomer distribution on a nano-structure level in the future, such investigations will allow us to predict a more efficient CL model.

1.5 Confined Ionomer Thin Film

As mentioned previously in Chapter 1.3, the PEM is a crucial component in PEMFCs. There have been many studies focused on the structure and performance properties of different PFSA bulk membranes under various conditions [8, 11, 13-15. 74]. However, the properties of a confined thin-film ionomer are still not well understood. It has been shown that Nafion is heterogeneously distributed inside the electrode and usually confined to a 2-10nm thick thin film [75, 76]. Such confinement can affect both the ionomer morphology and performance, i.e. proton conductivity

The intrinsic ionic conductivity can be affected by the nanostructure of the ionomer film. Several studies investigating the proton conductivity have used a simplified transmission line model for their measurement [77- 83]. However, most of these calculations assume that the ionic conduction in the confined thin film follow the same mechanism as the bulk membrane, which may not hold true. Devproshad et al. [84] measured the proton conductivity and activation energy of a 50nm thick Nafion thin film adsorbed onto a silicon substrate. The conductivity of the thin film was determined to be 31 mS/cm at 60°C and

96% RH, which is lower but in the same order of magnitude as the bulk membrane (90-100 mS/cm) in fully humidified conditions at room temperature. The activation energy of the thin film ionomer was calculated to be 20 KJ/mol at 96% RH. This is similar to that of bulk Nafion membranes (9-14 KJ/mol). In contrast, at 20% RH, the activation energy of conduction in the adsorbed Nafion film was 115 KJ/mol, which was 3.5 times higher than that for Nafion 112 [85]. The difference in the activation energies suggested a difference in conduction mechanism between the bulk membrane and the adsorbed thin film. More studies on water uptake of confined ionomer films in CLs are reviewed in Chapter 3.

The water adsorption and transport in Nafion thin films have also been examined by several studies [86-88]. Eastman et al. [86] studied the swelling, water solubility and transport kinetics as a function of relative humidity of adsorbed Nafion films thinner than 222nm. The equilibrium water adsorption was analyzed using specular X-ray reflectivity (SXR), and a model based on neutron reflectivity was utilized to confirm that the confinement effect originated from the Nafion film (not the silicon substrate). The result showed that the amount of swelling was suppressed when the Nafion was confined to a film thinner than 60 nm. Also, the water uptake was lower in these <60nm thin films, which was verified with further quartz-crystal microbalance analysis. These effects were attributed to the macromolecular and morphological confinement of the Nafion thin film. In fact, the results from small angle x-ray scattering under grazing incident angles (GISAXS) suggested that the ionic domains were able to construct a more ordered structure as the thickness increased. More studies on water uptake of confined ionomer films in CLs are reviewed in Chapter 4.3.

Chapter 2

Experimental Methods

Different experimental techniques are introduced in this chapter, along with the experimental protocols.

2.1 Microstructure Studies

2.1.1Scanning Electron Microscope (SEM)

Morphology studies of the catalyst layers and whole MEAs were carried out using a LEO 1525 high resolution SEM. The microscope was run at 5kV-15kV for different materials. In the cross-section studies, the samples were freeze fractured under liquid nitrogen.

2.1.2 Transmission Electron Microscope (TEM)

A Hitachi HF-3300 TEM-STEM was used to study the ionomer distribution and carbon agglomeration inside the catalyst layers before and after operation. Two main methods were used in preparation of CL samples for TEM, full embedding and partial embedding. Both methods allow the samples to stabilize sufficiently for further ultrathin sectioning. While fully embedding is a simple and typical preparation method for TEM samples, partial embedding limits the inference of epoxy during the ionomer observation. At the beginning of both techniques, Araldite 6005, DDSA and DMP-30 (Spi Supplies) were mixed at a certain content. The resin was then poured into a silicon flat embedding mold to fill up approximately half of each cavity. The mixture was cured in an oven at 60°C for at least 8 hours to harden. After this, for fully embedding, the samples were cut into small

slices to fit into the cavity, sitting on top of the hardened half-epoxy block. More resin (Araldite 6005, DDSA and DMP-30) was then poured to fill up the cavities and cured in the oven for at least another 8 hours. On the other hand, to do the partially embedding, the samples were cut into small pieces and their surfaces were lightly smeared over with 10 resin: 1 hardener G1 epoxy (Epoxy Technology). The G1 covered samples were then placed onto the hardened half-epoxy blocks. The mold was then filled with more resin (Araldite 6005, DDSA and DMP-30) and cured at 60°C for at least 8 hours. These epoxy blocks were then trimmed with a Leica EM Trim, and sliced into 50-100nm pieces on a Leica EM FCS microtome, using an Ultra 35° Diatome diamond knife.

2.1.3 Porosity

A porosity study was carried out using Quantachrome Instruments autosorb IQ. Nitrogen gas was used as absorbate. A 9mm tube with bulb cell was used in all the measurements. The samples were first degassed at 120°C under high vacuum until the pressure rise is lower than 20μmHg/min. Afterwards, the samples were quickly transferred to the gas adsorption station where nitrogen is admitted, adsorbed and then desorbed on the samples' surface and inside the pores. The adsorbed/desorbed volume of nitrogen was measured at different relative pressures (0.001-1.0). The data was analyzed with the software built-in multipoint Brunauer-Emmett-Teller (BET) method and Barrett, Joyner and Halenda (BJH) method to compute the surface area and pore size distribution.

The porosity terms used in this study follows the terminology defined by previous IUPAC documents [89-91]:

Micropores have diameters smaller than 2nm;

Mesopores have diameters between 2 and 50nm;

Macropores have diameters above 50nm.

BET is the most widely used theory in surface area measurement. Its concept is an extension to Langmiur theory, with the following hypotheses: 1) the gas molecules can physically adsorb onto a solid surface in layers infinitely; 2) no interaction occurs in between different adsorption layers; 3) Langmuir theory can be applied to each layer[92]. The BET equation is shown below [93]:

$$\frac{1}{W((P_o-P)-1)} = \frac{1}{W_m C} + \frac{C-1}{W_m C}\left(\frac{P}{P_O}\right) \qquad (2.1)$$

Where, W is the weight of the gas adsorbed at a relative pressure, P/P_o; W_m is the weight of the adsorbate that builds a monolayer of surface coverage; C is the BET constant, it's related to the energy of adsorption in the first adsorbed layer and consequently its value indicates how strongly the adsorbent/adsorbate interact. During a multipoint BET measurement, the value of $\frac{1}{W((P_o-P)-1)}$ is measured at various relative pressures, generating a linear plot. According to equation 2.1, the weight of the monolayer adsorbate can be calculated from the slope s and intercept i.

$$s = \frac{C-1}{W_m C} \qquad (2.2)$$

$$i = \frac{1}{W_m C} \qquad (2.3)$$

Therefore, $$W_m = \frac{1}{s+i} \quad (2.4)$$

The pore size distribution reflects the distribution of pore volume. In most cases, the desorption isotherm is applied to evaluate this since the desorption process is more thermodynamically stable. Assuming cylindrical pore geometry, the mesopore size can be calculated using the Kelvin equation [33]:

$$r_K = \frac{-2\gamma V_m}{RT \ln(P/P_o)} \quad (2.5)$$

Where, γ is the surface tension of the adsorbate at its boiling point; V_m is the molar volume of the liquid form adsorbate; T is the boiling temperature of the adsorbate and r_K is the Kelvin radius of the pore. When nitrogen is used, the equation reduces to:

$$r_K = \frac{4.15}{\log(P/P_o)} \quad (2.6)$$

In the Barrett, Joyner, and Halenda (BJH) method, it is assumed that the initial relative pressure is close to unity and all pores are filled with liquid nitrogen. The pore volumes at a certain relative pressure can be expressed as [33]:

$$V_{pm} = \left(\frac{r_{pn}}{r_{Kn} + \Delta t_n/2}\right)^2 (\Delta V_n - \Delta t_n \sum_{j=1}^{n-1} Ac_j) \quad (2.7)$$

Where, Δt_n is the thickness of the adsorbed nitrogen; Ac is the area exposed by the pore where the nitrogen gas is being desorbed; r_{Kn} is the inner capillary radius; r_{pn} is the radius

of the largest pore that has a physically adsorbed layer of nitrogen and ΔV_n is the liquid volume reduced by the nitrogen desorption.

To be noted, the BJH method is based on the Kelvin model, where a bulk condensation behavior is assumed. In other words, it is presumed that nitrogen condenses to its liquid form inside the pores, which is not true for the micropores. Therefore, BJH fails to accurately reflect the distribution of micropores.

2.2 Electrochemical Approach

2.2.1 Polarization Curve

Polarization curve measurement is one of the most common electrochemical characterization methods for PEMFCs [94]. Before executing polarization study, the fuel cell was conditioned at 80°C, 60-70% RH under H_2/O_2 and 13 psi overnight. The conditioning steps were carried out in a loop as the following: OCV for 2 minutes→ 0.6V for 10 minutes→ 0.9V for 4 minutes→ chronoamperometry (CA) method from OCV to 0.4V, with a 0.2V increment and 30s stabilizing time at each polarization point→ 0.6 for 10 minutes→ OCV for 2 minutes…

Polarization curves were then acquired with a Fuel Cell Technology fuel cell test stand unit. A steady state *I-V* curve measurement was used for the polarization study. The cell operating temperature was set at 80°C during all the electrochemical experiments. The flow rate and pressure of pure hydrogen gas is 1.5 stoich with a minimum flow rate of 50mL/min and 13psi; oxygen and air are 2 and 2.5 stoich with minimum flow rate of 100 mL/min and

13 psi. The relative humidity of the cell varies from 30%-100%, which was achieved by altering the temperature of the inlet gas humidifiers.

2.2.2 Proton Conductivity

Inside the PEM catalyst layers, the ionomer provides a channel for the proton transport. Therefore, even though the amount of polymer electrolyte used in the CL is significantly smaller than that in the membrane, it is still crucial to the overall fuel cell performance. The main impedance in a PEMFC is due to the cathode since the oxygen reduction is much slower than the hydrogen reaction on the anode. Electrochemical Impedance Spectroscopy (EIS) is a commonly used measurement method that can be applied to determine the catalyst layer resistance [77]. During EIS, AC signals of various frequencies are applied to the electrochemical interface; the impedance derived from the response signal upon cell current or voltage oscillation gives information on the polarization behavior of the electrodes [95]. The depth of the current penetration depends on the current frequency and phase angle. At low frequency, the current can penetrate the whole electrode and access all the pores; the entire capacitance is represented. Vice versa, at high frequency, only a small part of the capacitance is accessed and the pores behave in a semi-infinite manner [96]. A typical Nyquist plot of the impedance spectra of a fully humidified N_2/H_2 fuel cell is shown below in Figure 2.1.

The difference between the value of the real resistance where the Nyquist plot turns vertical (which would be $0.202\Omega cm^2$ in Figure 2.1) and the high frequency resistance (HFR) ($0.182\Omega cm^2$ in Figure 2.1) is one third the value of the catalyst layer's resistance R_{CL}.

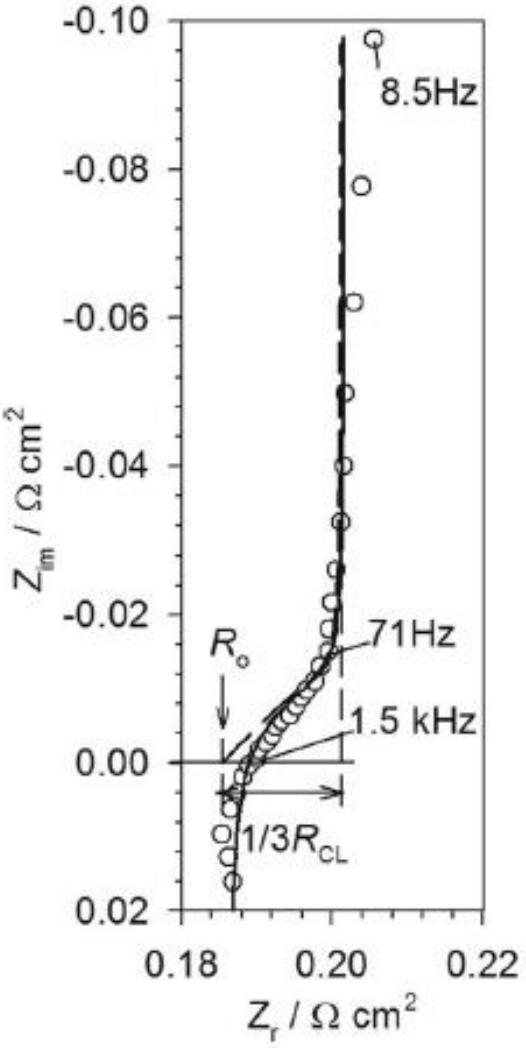

Figure 2.1 Nyquist plot of a fully humidified N_2/H_2 fuel cell [77]

Also, the ionic resistance R_{ionic} is the main contributor to the R_{CL}. This allows the estimation of the CL's ionic resistance through image plotting [77].

Another way to extract the ionic resistance from the impedance response is fitting the ionic resistance R_{ionic}, the membrane resistance $R_{membrane}$ and the catalyst layer capacity C_{CL} to a transmission line model. One of the most popular electrode models is the transmission-line model of the uniform pore. As shown in Figure 2.2, the catalyst layer contains electronic resistance $R_{electronic}$ which is caused by the electrons travelling through the carbon support and ionic resistance R_{ionic} which is caused by the proton transported through the ionomer. $R_{electronic}$ and R_{ionic} are connected by capacitors C_i and resistances R_{ct} in parallel. The capacitors present the electrochemical double layer and the resistances represent the charge transfer resistance from the oxygen reduction reaction (ORR) [97].

It is assumed that the resistance and the capacitance due to the electrochemical double layer are distributed along the uniform pores [98]. When running H_2/N_2, there is no charge transfer resistance. Therefore the transmission line can be simplified into the model shown in Figure 2.3.

Under such conditions, the total impedance of the electrode is:

$$Z(jw) = \sqrt{\frac{R_{CL}}{jwC_{CL}}} coth\sqrt{jwR_{CL}C_{CL}} \qquad (2.7)$$

Where C_{CL} is the total electrode capacitance, w is the frequency (rad/s).

To further interpret the impedance spectra, at a high frequency, the Nyquist plot of the impedance shows a Warburg-like 45° slope.

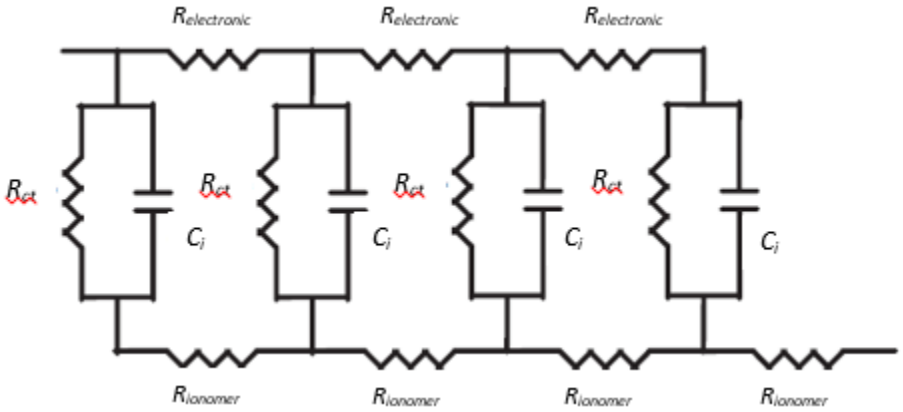

Figure 2.2 Transmission line model of a porous electrode [97]

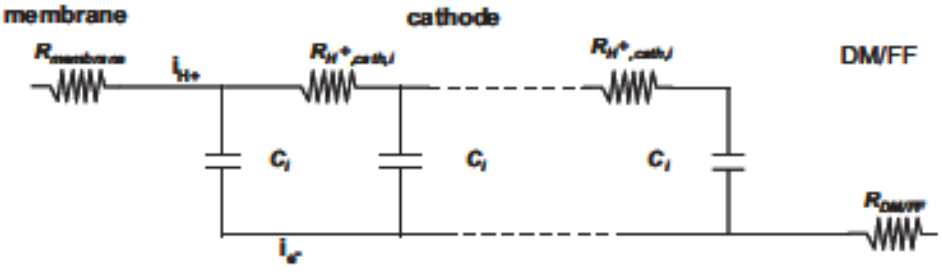

Figure 2.3 Simplified Transmission-line model [78]

$$\underset{w\to\infty}{Z(jw)} = \sqrt{\frac{R_{CL}}{jwC_{CL}}} \qquad (2.8)$$

This 45° slope region is used to fit the values for proton resistance. Furthermore, when running H_2/N_2, the losses in the polarization curve due to proton resistance is around R/3 and the kinetic resistance is infinitely high. So, the impedance at low frequencies can be described as [96, 99-101]:

$$Z_{(w=0)} = \frac{R_{CL}}{3} + \frac{1}{jwC_{CL}} \qquad (2.9)$$

Therefore, theoretically, the impedance plot curves up to 90°C vertical which corresponds to the total capacitance and resistance of the catalyst layer. The ionic resistance R_{ionic} can be calculated according to the length of the Warburg-like region projected onto the x axis, which equals $R_{ionic}/3$ [102]. Further discussion and specific details of this study is explored in chapter 3.

2.3 Thermal Studies

The thermal stability of the CL and its components were studied by thermogravimetric analysis (TGA) method. TGA is a commonly used method to characterize the weight gain/loss of the material during a change of temperature. It provides information about physical (adsorption, evaporation, sublimation) and chemical (decomposition, chemisorption, desolvation) phenomena. All TGA experiments in this study were carried out under nitrogen atmosphere in order to avoid the interaction between carbon and oxygen at elevated temperature in the presence of Pt. The examined samples were kept at room temperature in air beforehand. Therefore a certain amount of water was expected inside the

samples. Prior to each TGA run, the platinum sample holder was cleansed by heating it quickly with a propane torch.

Differential scanning calorimetry (DSC) was used for thermal studies of the catalyst layer and components of the catalyst layer. DSC is a thermoanalytical equipment that measures the difference in amount of heat required to raise the sample and reference to a certain temperature. During the measurement, the temperature increases linearly as a function of time. At some temperature, the sample will go through a physical transformation and will require or release heat. By observing the difference in heat flow between the sample and reference, DSC can measure the amount of heat adsorbed or released during the transition [103]. For ionomer samples, the membrane was cut into tiny pieces (~0.25 cm^2) and placed into the aluminum sample pan, weighed and pressed shut with a pan cover using a Tzero sample press. For the CL and the cross-referencing of individual elements, components were mixed into a solution then sonicated for 15 minutes. The ink was then dropped into the pan through a pipette till the pan is completely filled. The pans were then placed at room temperature until the alcoholic solution fully evaporated; for the samples in water solution, the pan was placed in the oven at 60°C to allow the water to slowly evaporate. The dry powder samples were then weighed and pressed shut, and tested in the calorimeter under a flowing nitrogen atmosphere at 5°C/min heating rate.

2.4 MEA Preparation

In the catalyst study, the in-house MEAs are prepared using a direct spray method. First, the proton exchange membrane is boiled in 3% hydrogen peroxide solution at 90°C for 30

minutes then boiled in 0.5M sulfonic acid at 90°C for 30 minutes. This ensures the PEM is in H^+ form. The membrane is then set on a spray painting station at 60°C, ready for spraying. As for the cathode, 30wt% platinum on Vulcan carbon, 5wt% 3M ionomer in alcohol or water solution and methanol were mixed to different ionomer to carbon (I/C) ratios as the catalyst ink. The ink is then stirred overnight and sonicated for 30 minutes before spraying onto the pretreated membrane. The mass difference of the pre-sprayed and sprayed membrane are measured to calculate the exact Pt loading (~0.4 mg/cm^2). For the anode, an I/C=1, platinum loading of 0.2 mg/cm^2, Nafion as ionomer electrode was used as standard reference. PTFE treated carbon fiber composite carbon paper was used as gas diffusion layer (GDL). The GDLs are pressed onto both sides of the MEA in the single cell fuel cell hardware. No hot pressing procedure was used during the MEA preparation.

Chapter 3

Proton Conductivity Measurement of the CL in PEMFC

3.1 Introduction

Improving the CL proton conductivity is essential for optimizing the fuel cell design. However, the measurement of the proton conductivity in the CL can be fairly challenging due to several reasons. For instance, the microstructure of the CL needs yet to be fully discovered. Moreover, during the cell operation, the mass and proton transport both contribute to the overall loss in the cell. It is challenging to separate the mass (gas transport) loss from the proton conduction loss though polarization and modeling work. This chapter attempts to unveil a path to and evaluate these losses.

For a perfluorosulfonic acid (PFSA) membrane, there are two different proton transport mechanisms: one is the "Grotthus mechanism"/ "proton hopping"; another is the "diffusion mechanism"/ "vehicular mechanism" [104-106].

For the Grotthus mechanism, the proton is 'hopping' from one water molecule to another by forming, breaking and reforming hydrogen bonds. In PFSAs such as Nafion, these water molecules exist in phase-separated pores bounded by acid sites. During the diffusion process, instead of only the proton moving along the ionic sites, the proton is weakly attached to one or more water molecules in the aqueous medium. Zawodzinski et al. [107] suggested in his study that the Grotthus mechanism contributes more greatly in the well-hydrated Nafion membrane and is limited at low water content.

In most of the previous CL proton conductivity studies, it is assumed that the recasted ionomer film possesses the same proton conduction mechanism as the bulk ionomer membranes [78, 79, 82, 83, 108, 109]. However, it has been questioned whether the two may be different [110, 111]. Paul D.K. et al. [110] revealed through his study that transport through the thin adsorbed Nafion film has a significantly higher activation energy than that in a bulk Nafion membrane, indicating a difference in the conduction mechanism between the two. Paul further suggested that such deviation can be caused by the different orientation of the polymer chain structure. This can lead to a strong interaction between the sulfonate and other surface functional groups, lessening the water adsorption.

3.2 Method Development

Various studies have reported experimental determination of the ionic conductivity of the CL in PEMFCs [77-83] applying various transmission line models. Because of the very fast kinetics of the hydrogen oxidation reaction (HOR) in the anode, the reaction takes place close to the interface between the GDL and the CL. Therefore the proton transfers through a very short pathway for the reaction at this electrode. The proton resistance created by the HOR is negligible compared to the cathode resistance. For proton transport studies, EIS measurements are required and usually operated under H_2/N_2. Therefore the charge resistance created by the ORR is eliminated. The EIS measurement is required to be carried out at a sufficiently high potential to ensure the experiment is running under limiting current and therefore the AC impedance signal is not influenced by the hydrogen crossover and to ensure that the CL capacitance becomes independent from the RH level. One of the most commonly used models for this study is shown in Figure 3.1.

When the number of elements in this transmission line model is considered to be infinite, and the value of the resistance and capacitance are equal, it can be replaced by a finite length diffusion element with a reflective boundary. Thus the MEA transmission line can be expressed as the equivalent circuit in Figure 3.2. The inductance was added for completion to the model representing a CL artifact, and is often set to 0.

The impedance response of the equivalent circuit can be described as:

$$Z = R_o + R_{CL}\frac{\coth\sqrt{j2\pi f\tau}}{\sqrt{j2\pi f\tau}} \qquad (3.1)$$

Ro is the sum of the membrane and contact resistance, R_{CL} is the protonic resistance in the CL, j is the imaginary unit, f is the frequency and τ is the diffusion time constant which equals $R_{CL}\cdot C_{CL}$.

Several assumption underlies in this calculation [80]:

(1) The pores are uniform in cross-section and semi-infinite in length;

(2) Ionomer is homogeneously distributed throughout the CL;

(3) The electronic resistance of the electrode material is negligible;

(4) Sufficient amount of ionomer exist in the CL to cover the Pt/C agglomerate surfaces;

(5) Any curvature of the equipotential surface in the pores is negligible.

As the frequency approaches 0, a Taylor-series expansion yields:

$$Z = R_o + \frac{R_{CL}}{3} + \frac{R_{CL}}{j2\pi f\tau} \qquad (3.2)$$

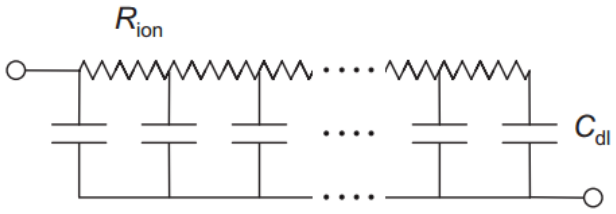

Figure 3.1 Simplified Transmission Line model for PEMFC electrodes under H_2/N_2.

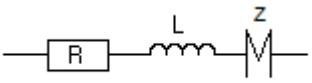

Figure 3.2 Equivalent Circuit for MEA with a homogeneous CL. This is the actual model used in the Z fit software.

During the impedance measurement, theoretically, at very high frequency, the impedance equals the value of *R*. As the frequency decreases, both the imaginary and the real portion of the impedance increase at the same rate resulting in the 45 degree slope area in the higher frequency region. When the frequency approaches zero, the AC signal penetrates the whole CL, reaching the limiting resistance as the impedance increases infinitely. In the low frequency region, the capacitance inside the CL becomes fully charged, blocking all current, exhibiting a vertical line. A graphical method can be used to determine the ionic conductivity in the CL [108] by obtaining the difference between two intersections, that between the vertical line and the real impedance axis and that between the high frequency 45 degree line and the real impedance axis. That difference is approximately equal to $R_{CL}/3$.

3.2 Experimental

MEAs with 5cm^2 active area were prepared using the previously described method of directly spraying an ink onto Nafion 212 membrane. 30% Pt on Vulcan carbon (Taneka) was mixed with 5% 3M ionomer in n-propanol solution to 0.8 I/C ratio for the cathode. For the anode, 30% Pt on Vulcan carbon (Taneka) was mixed with 5% Nafion solution (1100 EW, Ion Power) in alcohol-based solution to I/C=1. The Pt loading was approximately 0.2mg/cm^2 on the anode and 0.4mg/cm^2 on the cathode. This catalyst coated membrane (CCM) was then placed between two carbon paper diffusion layers (Toray paper 030, 110μm), assembled into a single cell fuel cell hardware (Fuel Cell Technology). The cell was connected to a Fuel Cell Technology fuel cell test station and a Bio-Logic SP-150 potentiostat was used to perform the EIS.

H_2 and N_2 were purged at 100 mL/min, the cell temperature was set at 80°C, and set at 0.2 V vs $E_{reference}$. The frequency ranged from 0.5 Hz to 20 kHz with a voltage perturbation of 30mV voltage perturbation.

Prior to the EIS, the cell underwent H_2/O_2 and H_2/Air polarization studies at various RH (35%-100%) and was set overnight at 80% RH at OCV purging H_2/N_2. Between each different RH setting, the cell rested for 45 minutes at OCV to reach equilibrium.

3.3 Result and Discussions

During the hydrogen pump process, the hydrogen diffuses from the anode through the membrane into the cathode catalyst layer. The hydrogen then is oxidized into protons and these protons transport back from the cathode through the membrane to the anode. Figure 3.3 compares the Nyquist plot obtained from the model and the experimental AC impedance signal obtained with 0.8 I/C ratio 3M ionomer CL at 80% RH. As shown, the ideal response of the equivalent circuit deviates from the experimental obtained data. In the Warburg-like region the actual data shows a larger slope than the expected 45 degree and the transition to the low frequency region is more gradual than the fitted result. Furthermore, the actual Nyquist plot of the low frequency region veers from the theoretical vertical line. In Figure 3.4 one can observe that the HFR decreases as the RH level increase, which is expected due to the humidification of the Nafion membrane. Also, the deviation behavior show to be more severe at lower RH. One of the more obvious explanation for this is that under dryer condition, the RH is non-homogeneously distributed throughout the CL forming a non-uniform electrochemical system. Similar observations and more

discussions can be found from previous studies. Ikeda et al. [112] reported both deviations in the vertical and 45° slope region, stating such behaviors as the result of the agglomeration structure in the CL and non-homogeneous distribution of the ionomer, respectively. A.P. Young [79] proposed that this deviation occurs because the transmission line model was built under the assumption that all the CL contained a series of uniformed cylindered pores even though the CL structure in reality contained pores with various shapes and sizes. Therefore the deviation between the ideal and experimental data can be due to the difference in local pore geometry. Indeed, Eloot et al. [113, 114] reported the influence of different pore shapes and sizes on the conductivity. Cimenti et al. [81] claimed the possible causes to be internal shortening, hydrogen crossover and/or capacitive dispersion of the double layer. However, during A.P. Young's study [79], an internal resistance was added into the equivalent circuit, yet the deviation was still observed. Recently, Malevich et al. [77] compared the typically used transmission line model and a "nested" transmission line model that included the effect of the CL agglomerate-type. His result showed that the low-frequency area still exhibited a vertical line despite the consideration of the agglomeration distribution. Further on, he computed Nyquist plots for equivalent circuits with non-homogeneously distributed resistance and capacitors. The result still showed a 90° low-frequency region indicating that the heterogeneity of the resistance and capacitor distribution does not yield a sloped Nyquist plot. However, a deviation in the low-frequency region was observed in two different accounts: introducing a constant phase element into the transmission line model or considering the faradaic current contribution that was caused by an unlimited hydrogen crossover. Furthermore,

most of the transmission line models used in CL proton conductivity studies assume that the mechanism of proton transport is the same in recast thin ionomer film as that in bulk ionomer membrane [77, 78, 81]. However, several studies reported that the intrinsic ionic conductivity can be affected by the nano-structure of the ionomer film [110, 115]. The effect of the difference in transport mechanism to the slope area of the Nyquist plot has yet to be revealed.

A different approach to modeling the impedance response of the porous electrode with a frequency dispersion is by introducing a constant phase element (CPE) to the equivalent circuit. According to previous reports, the dispersion may have arose from the inhomogeneous pore structure throughout the CL [116]. The impedance of the CPE can be described as the following [117]:

$$Z_{CPE} = \frac{1}{Q(2\pi jf)^n} \qquad (3.3)$$

Q is the CPE coefficient; *n* varies between 0 and 1, when *n*=1 the CPE behaves as a normal capacitor.

The CPE results into a non-vertical impedance curve in the low frequency area. Therefore, another transmission line model is introduced by substituting the capacitances with CPEs as shown in Figure 3.5 [118]. By fitting the impedance response to this model, shown as the dot-dash line in Figure 3.5, both a 45 degree Warburg area and a "sloped" low frequency area were observed.

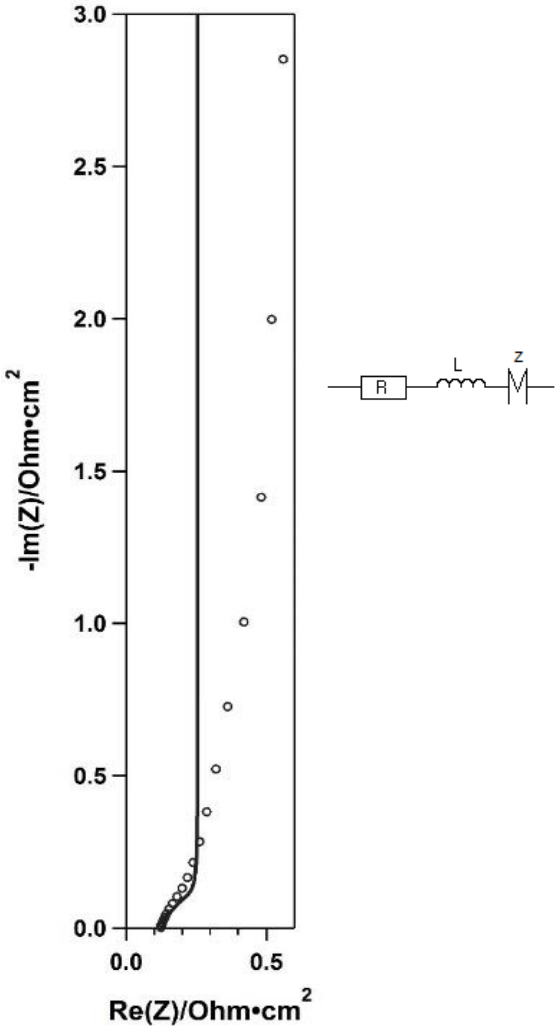

Figure 3.3 Nyquist plot of 3M ionomer CL at I/C=0.8, 80% RH. The hollow circles represent the experimental data and the solid line represents the fitted line using the equivalent circuit shown.

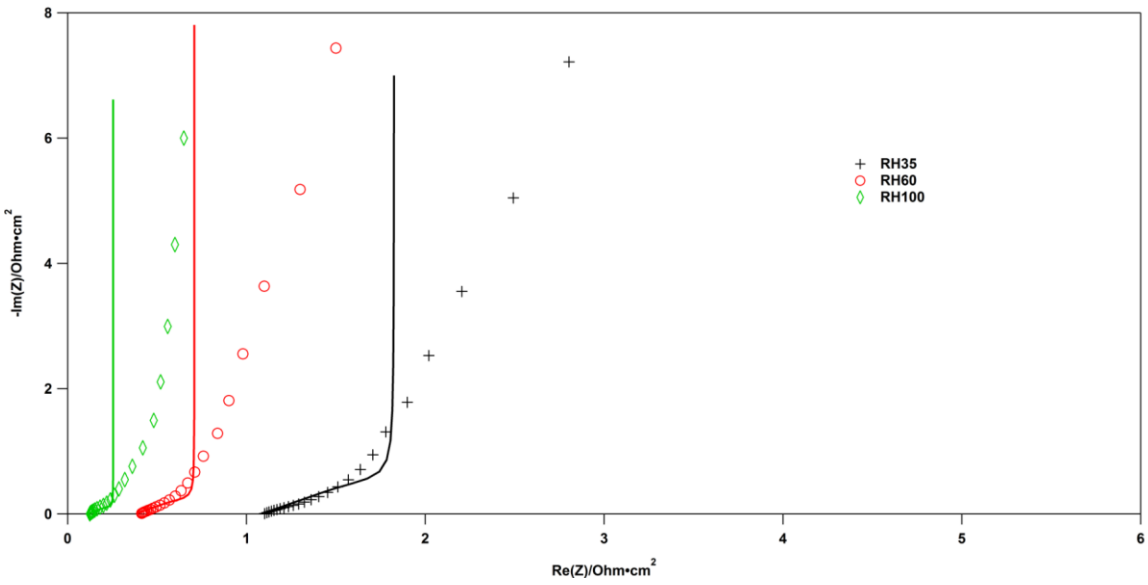

Figure 3.4 Dependence of Nyquist Plot to the RH level. I/C=0.8 3M ionomer cathode CLs were measured at 35%, 60% and 100% RH. The fitted data is shown as solid line.

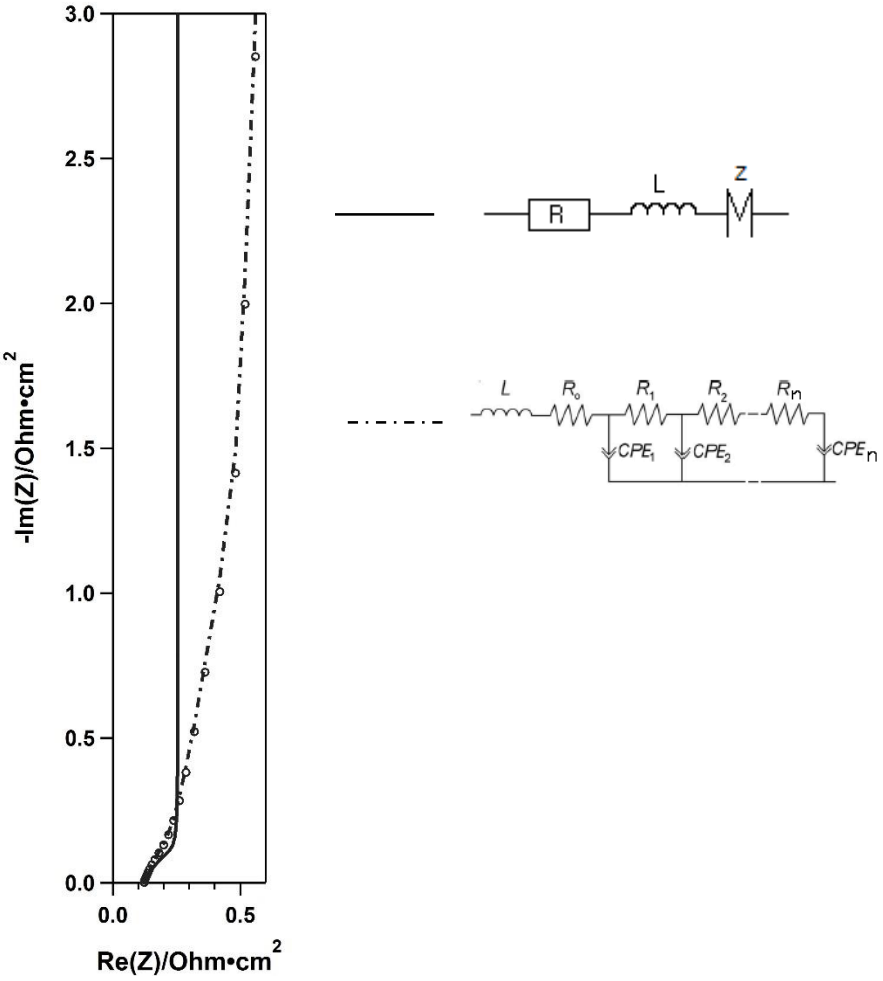

Figure 3.5 Comparison between the fitted lines using two different models. The hollow circles represent the experimental data.

Two different graphical fitting approaches were examined to determine the proton conductivity, as shown in Figure 3.6. $R_{vertical}$ was obtained by determining the real impedance value at the inflection point of the impedance curve; $R_{extension}$ represents the intersection between the extension of the post-Warburg region and the real impedance axis. The ionic resistance was then determined using the following equation:

$$R_{CL} = 3 \times (R_{vertical/extension} - HFR) \qquad (3.4)$$

Figure 3.7 illustrates the comparison of the ionic resistances of an in-house made 3M CL (I/C=0.8) at different RH values calculated with different graphical fitting methods. As expected, the calculated $R_{vertical}$ is consistently higher than $R_{extension}$. However the difference between these two values decreases as the RH level increases. The obvious cause of this is that, as mentioned before, the low frequency impedance response veers away more from the vertical line at lower humidity level resulting in a steeper slope for the extension line for the $R_{extension}$ calculation. Comparing the proton resistance obtained by the two different models, the values show a smaller variant at higher humidified level. This suggests that at higher RH level, the simple transmission line model containing a finite length diffusion element is more appropriate since the low frequency impedance slope is smaller which also means that the value of n is close to 1 and the CPE behaves more like a capacitor. Meanwhile, at lower RH (35%, 50% and 60%), a 2-3 fold difference is observed between the resistance obtained from a vertical fit using the CPE model and that using the traditional model. However, it is arguable to declare that either of these models gives a more accurate R_{CL}. On one hand, for the typical transmission line model (with the finite length diffusion

elements or distributed capacitors), it has been reported that if the resistance is not distributed uniformly, even if the real impedance reaches a limiting value, it might not accurately represent 1/3 of the CL resistance. Lefebvre et al. [108] studied the impedance response of a simulated transmission line model where the resistance increases from the CL/membrane interface towards the CL/GDL interface. The result indicated that the limiting real impedance value at low frequency is significantly lower than the total CL resistance. Malevich et al. [77] also reported a difference between the limiting real impedance value and the actual total CL in-series resistance in a non-homogeneous CL system. On the other hand, for the CPE model, the fact that the two approximation methods (vertical and extension) yield different R_{CL} values suggests that the factors that cause deviation between the actual CL resistance and graphically fitted resistance not only result in a non-vertical low frequency area in the Nyquist plot, but also alter the real impedance value of the inflection point between the 45 degree Warburg like region and the low frequency region. Furthermore, while using the CPE model, whether it is accurate to convert the real impedance to the actual CL resistance by simple math (multiplied by 3) needs to be examined by further modelling work.

In conclusion, our experiments showed that the divergence of the fitted and experimental Nyquist plot can be lessened by employing an equivalent circuit containing a constant phase element. Two different graphical fitting methods were applied, and yield more distinct results than the traditional transmission line model at lower RH levels. However, the accuracy of this graphical method needs to be further evaluated with further modeling work. Due to the reasons above and in order to make our proton conductivity

data more compatible with the previous conductivity studies reported, the traditional transmission line model was used in our following CL studies.

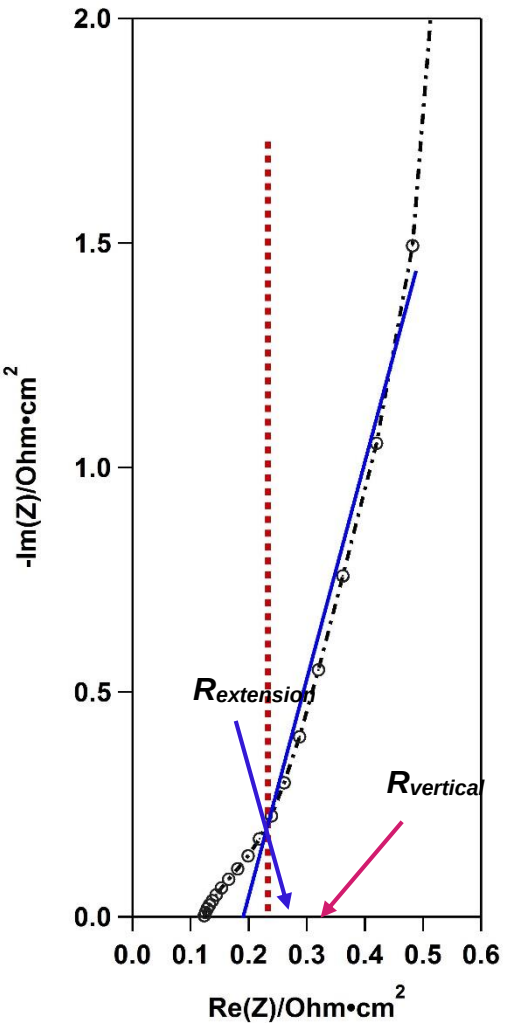

Figure 3.6 Different graphical approaches to determine the CL resistance. The hollow circles are the experimental data; the dot-and-dash line represents the fitted data with the transmission model containing CPEs. One approach is drawing a vertical line through the inflection point where the Warburg region ends, the intersection between this vertical line and the real impedance axis yields $R_{vertical}$; the other approach is extending the fitted line towards the x-axis, the intersection between the extension and the real impedance axis yields $R_{extension}$.

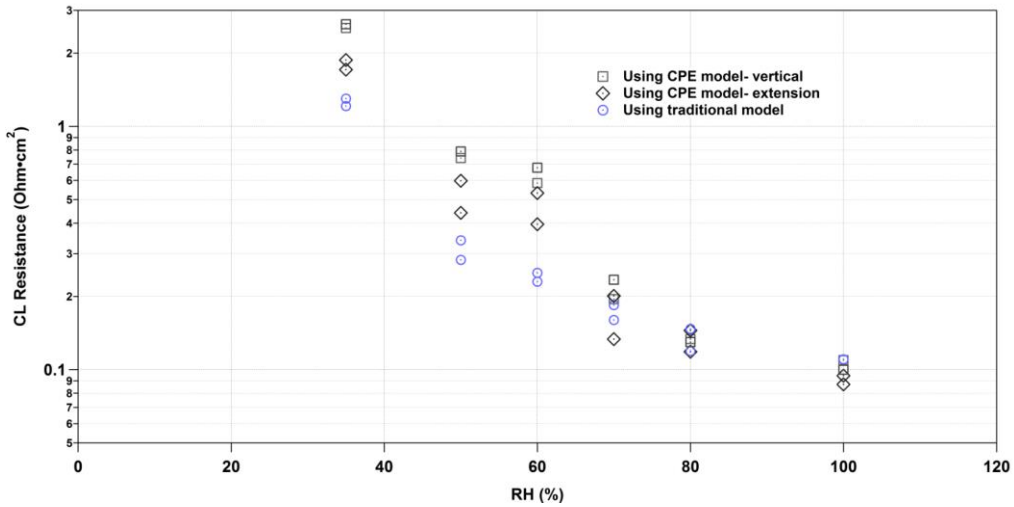

Figure 3.7 Proton resistance of the in-house made I/C=0.8 3M CL at various RH level.

Chapter 4

In-house Made 3M Ionomer Catalyst Layers

The complex structure of PFSAs has been studied extensively over the years. A key aspect of their behavior as membranes is their phase segregation. In many PFSA ionomers, the Teflon-like hydrophobic PTFE backbone contributes to the mechanical strength of the membrane. Meanwhile, the sulfonic acid groups form ionic aggregations under dry conditions. These hydrophilic ion "clusters" will absorb water when the membrane is humidified. These sulfonic acid groups provide the protons and the connected network of aggregates provide the path for conduction. However, too high of a loading of sulfonic acid groups will lower the content of backbone structure and crystallinity. It will also allow too much water to be adsorbed. This can cause complete disintegration in water. Aside from the typically used Nafion, there are several different PFSAs commercially available, such as polymers developed by Dow chemical and 3M Company. The main difference between the PFSAs is the molecular weight and structure of the side chain containing the sulfonic acid group [119].

In this chapter, catalyst layers that contain 3M ionomer were studied. As shown in Figure 4.1, the 3M ionomer contains a shorter side chain (lower formula weight of the repeat unit). Therefore at a given equivalent weight, such an ionomer has a higher content of PTFE backbone, which improves the mechanical properties (higher T_α) and leads to a higher proton conductivity at higher temperature and dryer operation conditions. Recently, an ionomer having the same chemical structure as the 3M PFSA has been studied by Asahi Kasei [74]. A comparison between Nafion (EW950) and 3M ionomer (EW800) showed that

the 3M polymer had a higher T_α and higher conductivity and thermal stability in TGA tests under both air and Argon.

Our in-house 3M ionomer CLs were prepared with 30% Pt/Vulcan XC-72 carbon and 5wt% 3M ionomer in n-propanol solution at different I/C ratios. The mixture was then stirred overnight to prepare it for characterization or further MEA assembling, which will be introduced in the electrochemical sub-chapter.

4.1 Morphology

Catalyst layers were prepared and subjected to microscopic examination to determine the overall morphology of the layer. Under SEM study, we observed a porous ionomer covered particle structure. However, it is difficult to identify the ionomer distribution inside the CL microstructure under SEM. We expected thicker ionomer coverage around the carbon particles as the ionomer/carbon ratio increases.

Through TEM study, the dispersion of individual components in the CL was studied. A partial-embedding method in epoxy block was used to prepare the samples slices. The reason for this choice of sample preparation instead of the typical full-embedding is to avoid a blend of ionomer and epoxy resin, so that we can study the ionomer distribution without the influence of epoxy. Figure 4.2 shows the TEM photograph of a partially embedded CL sample. This cross section can be divided into four different areas, the epoxy section, the membrane section, the epoxy-embedded area and the non-epoxy-embedded area. The last section will be our main focus since the CL microstructure can be observed most accurately.

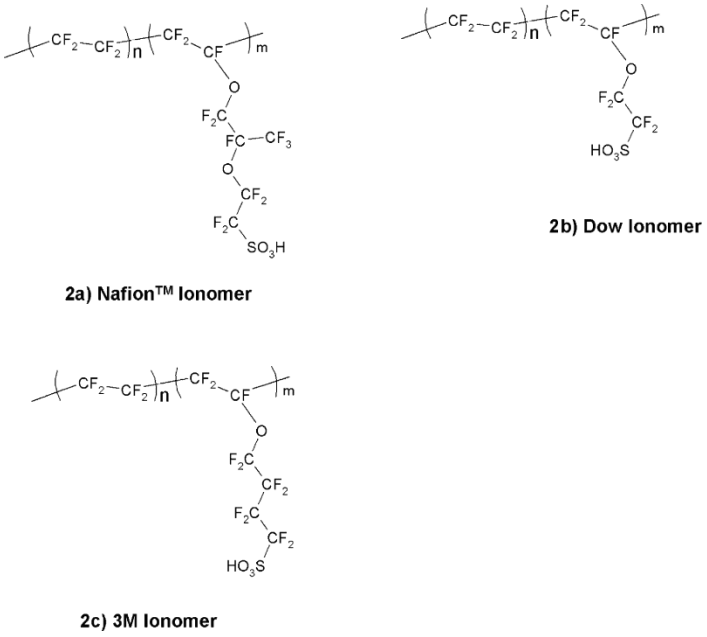

Figure 4.1 Structure of 2a) Nafion ionomer from DuPont. 2b) PTFA ionomer from Dow Chemical. 2c) PTFA ionomer from 3M Company.

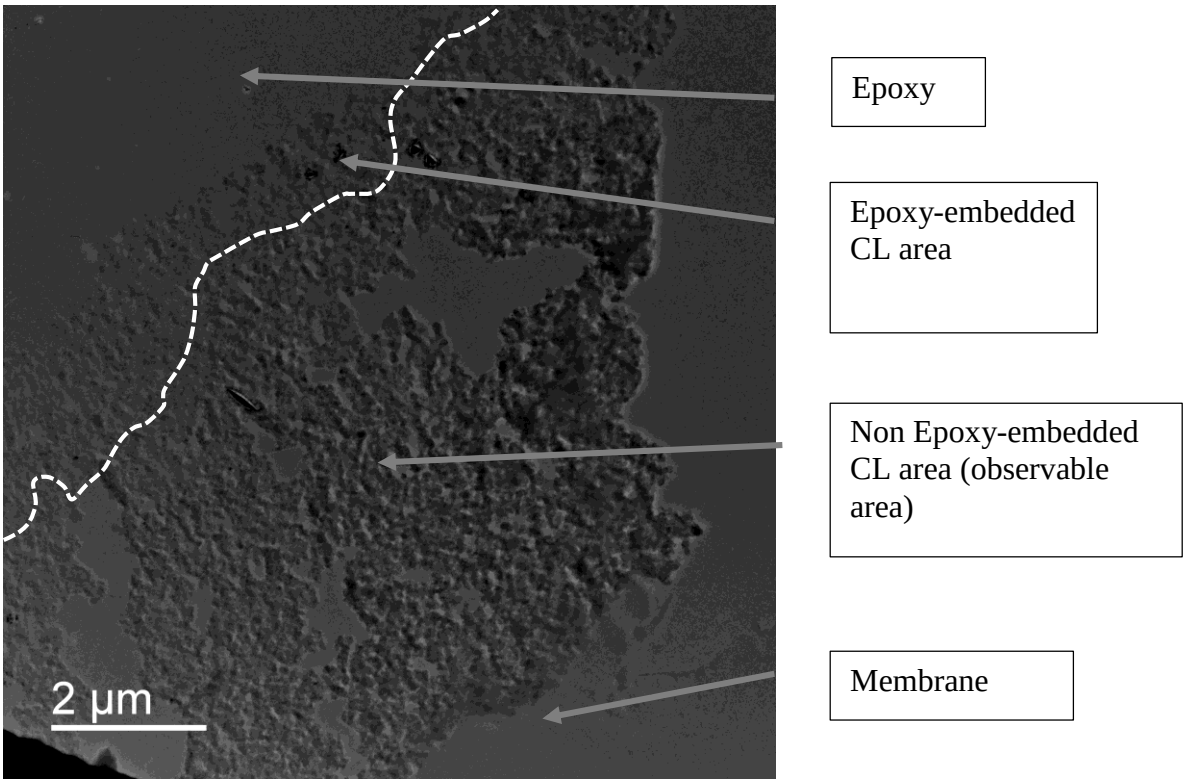

Figure 4.2 TEM image of Partially-embedded CL sample, I/C=1.2

Figures 4.3 and 4.4 show the TEM images of CLs with I/C ratios of 0.2, 0.8, 1.2 and 2. Under the electron microscopy, each individual component has a distinctive appearance. Amongst the CL components, Pt has the highest atomic number and crystallinity. Therefore, Pt should be the darkest component in the TEM images. Under higher magnification, as shown in Figure 4.5, the Pt appears to be quasi-circular particles that are on the order of 2-4 nm. Furthermore, the transmission electron microscopic images reveal that these Pt nanoparticles are dispersed on the Vulcan carbon support. Vulcan carbon possesses high surface area and graphitic structure that leads to high electronic conductivity. Its graphitic structure appears to be between ideally graphitic and amorphous. As shown in Figure 4.5, under higher magnitude, graphene layers with different orientations can be observed inside the carbon structure. Distinct from Pt and Carbon, the ionomer has a worm-like amorphous structure. Figure 4.6 shows an ionomer bridge-like structure that was damaged by the electron beam. The microscopic images show gaps that range in size from smaller than 2nm to larger than 400nm. It should be noted that since these micrographs only display a two-dimensional image, the actual pore sizes and shapes are not directly presented. Therefore, further pore size distribution studies were carried out with a nitrogen adsorption system to reveal the CL pore geometry more comprehensively.

As shown in Figure 4.3, under lower magnitude we observed large vacant pores amongst carbon agglomerates at lower I/C ratio with a diameter above 200nm. As the ionomer content increases, the ionomer fills or partially fills into the open pores, creating an ionomer web-like structure and lowering the pore sizes. This suggests that 3M ionomer can sufficiently penetrate into the pores between carbon agglomerates. Also, the lack of

ionomer web-like structure causes a more tortuous ionomer pathway at lower ionomer content. The ionomer appears to be closely adhered to the particle surface. Meanwhile, protons can transport through a wide ionomer network at higher I/C ratio, which is expected to result in a lower proton transport resistance at a given relative humidity level. Also, inside the ionomer web we observed Pt particles and agglomerates that were detached from the carbon support. These Pt particles are unable to perform electrochemical reactions because of their lack of electronic conduct. Such detachment could be caused by the stirring and sonication process during the CL ink preparation. Another possible cause is the mixing process. When mixing an alcohol based ionomer solution with Pt/C, if the mixture is not kept moist the alcohol can react with the Pt particles resulting in a brief heat burn. Such a reaction could damage the carbon support causing the detachment of the Pt particles. However, in the CLs that contain 3M ionomer in water-based solution, the detachment of Pt particles can still be observed, as shown in Figure 4.7. Since the procedure of mixing these CL ink didn't involve any contact between alcohol and Pt/C, we suggest that the stirring and sonication are the main contributors to the Pt detachment.

4.2 Porosity

Because of the partially amorphous structure Vulcan carbon, it was difficult to identify the ionomer coverage to a certain extent in the microscopic images. Nevertheless, the two dimensional images do not illustrate the actual pore size and shape. Therefore, a nitrogen adsorption/desorption system was used to measure the total surface area and pore size distribution of the CLs.

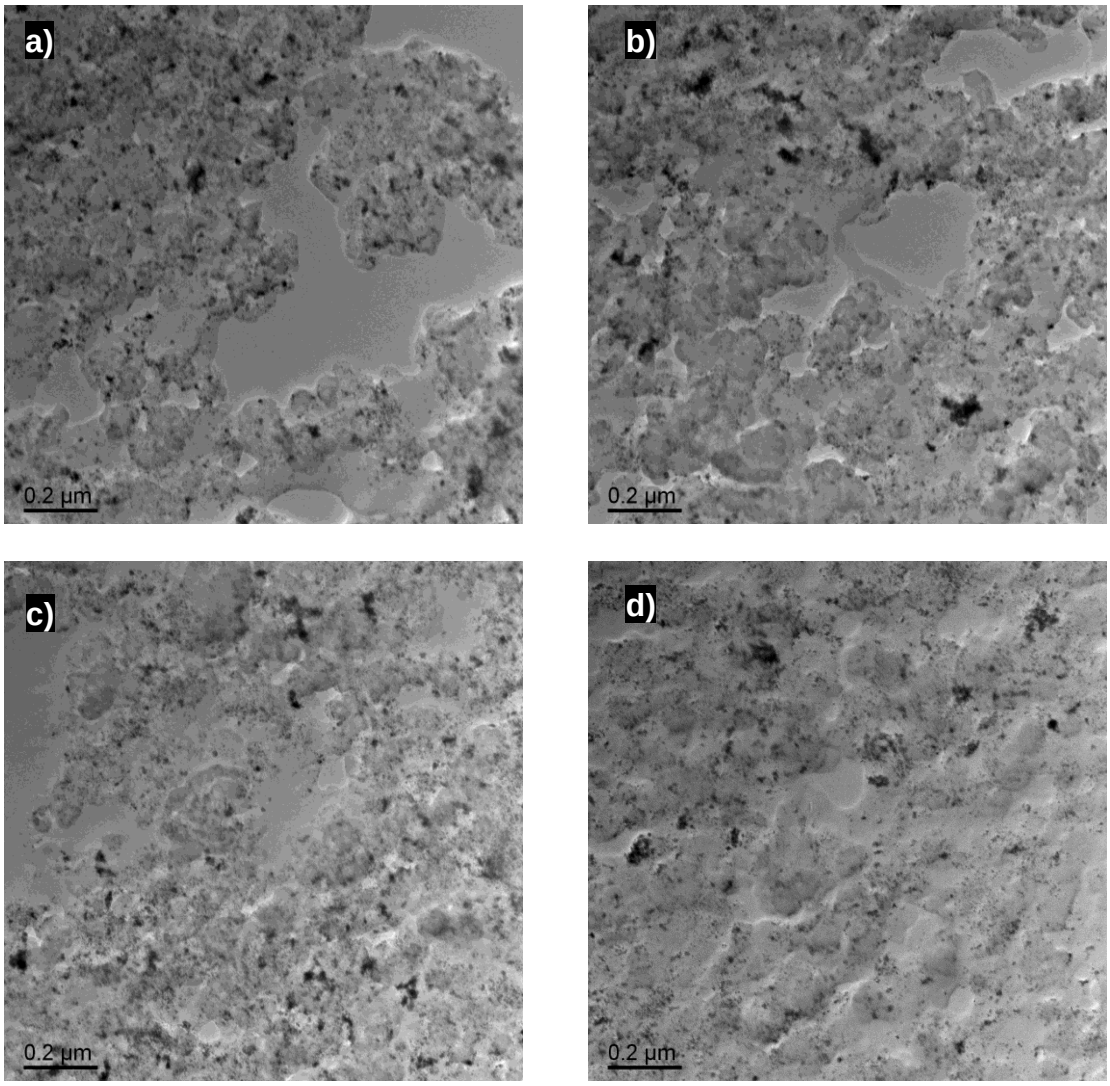

Figure 4.3 TEM images of alcohol based 3M CLs a) I/C=0.2; b) I/C=0.8; c) I/C=1.2; d) I/C=2

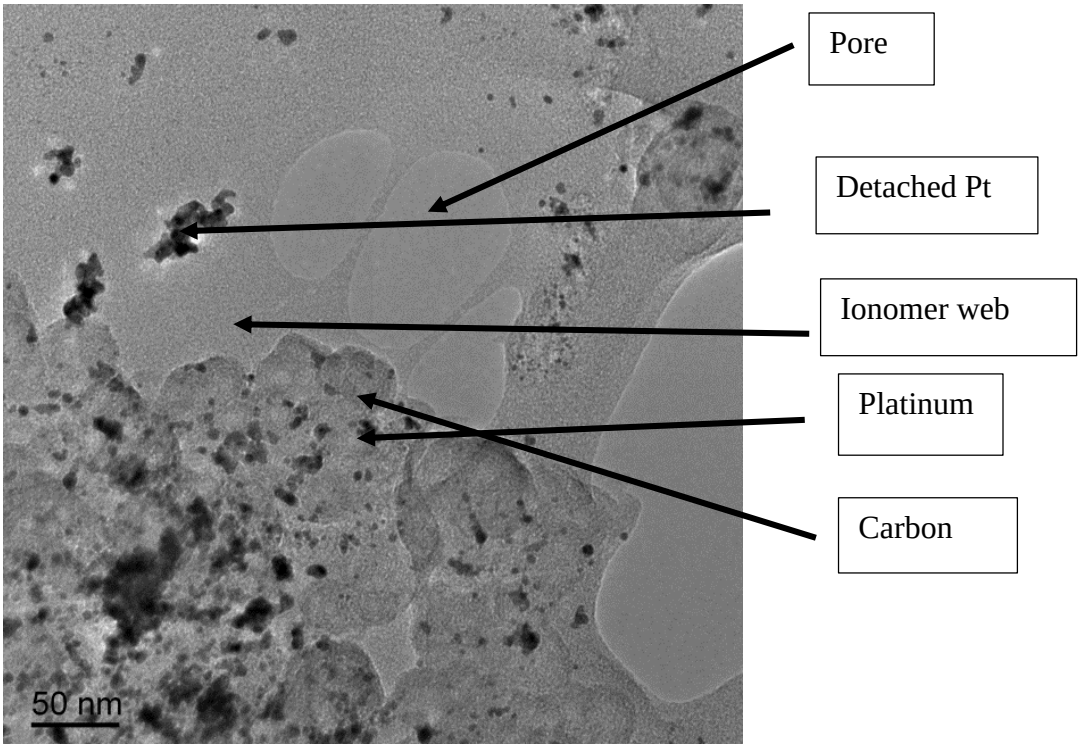

Figure 4.4 TEM images of alcohol based 3M CLs I/C=1.2

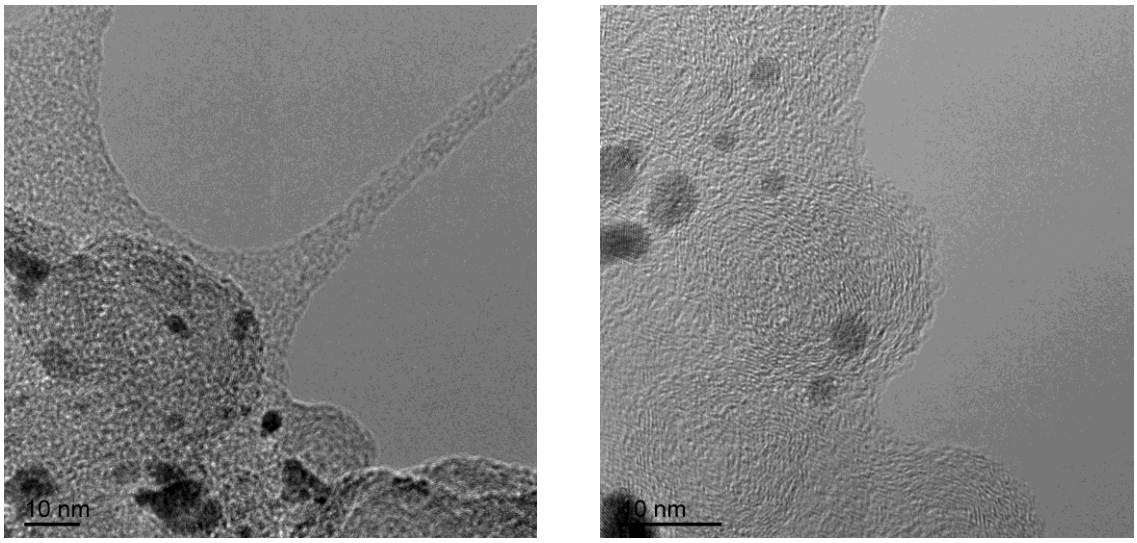

Figure 4.5 TEM image of 3M ionomer CL under high magnification

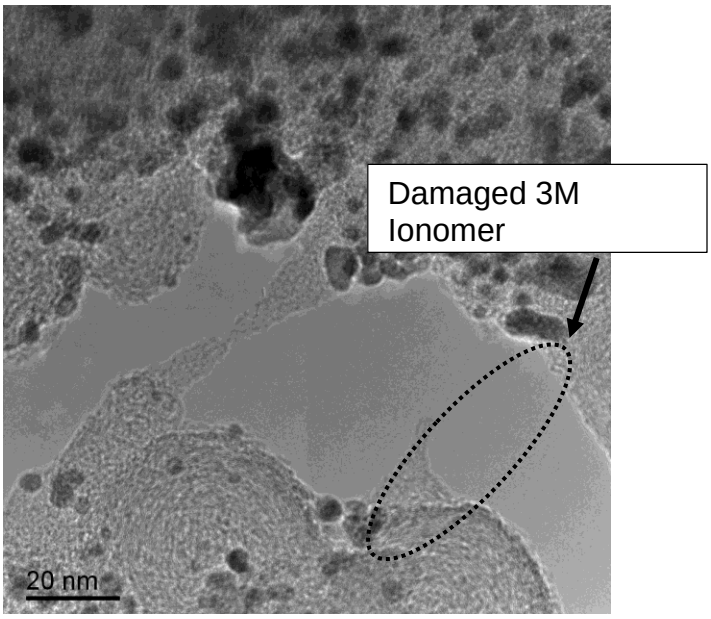

Figure 4.6 TEM Image of Damaged Ionomer

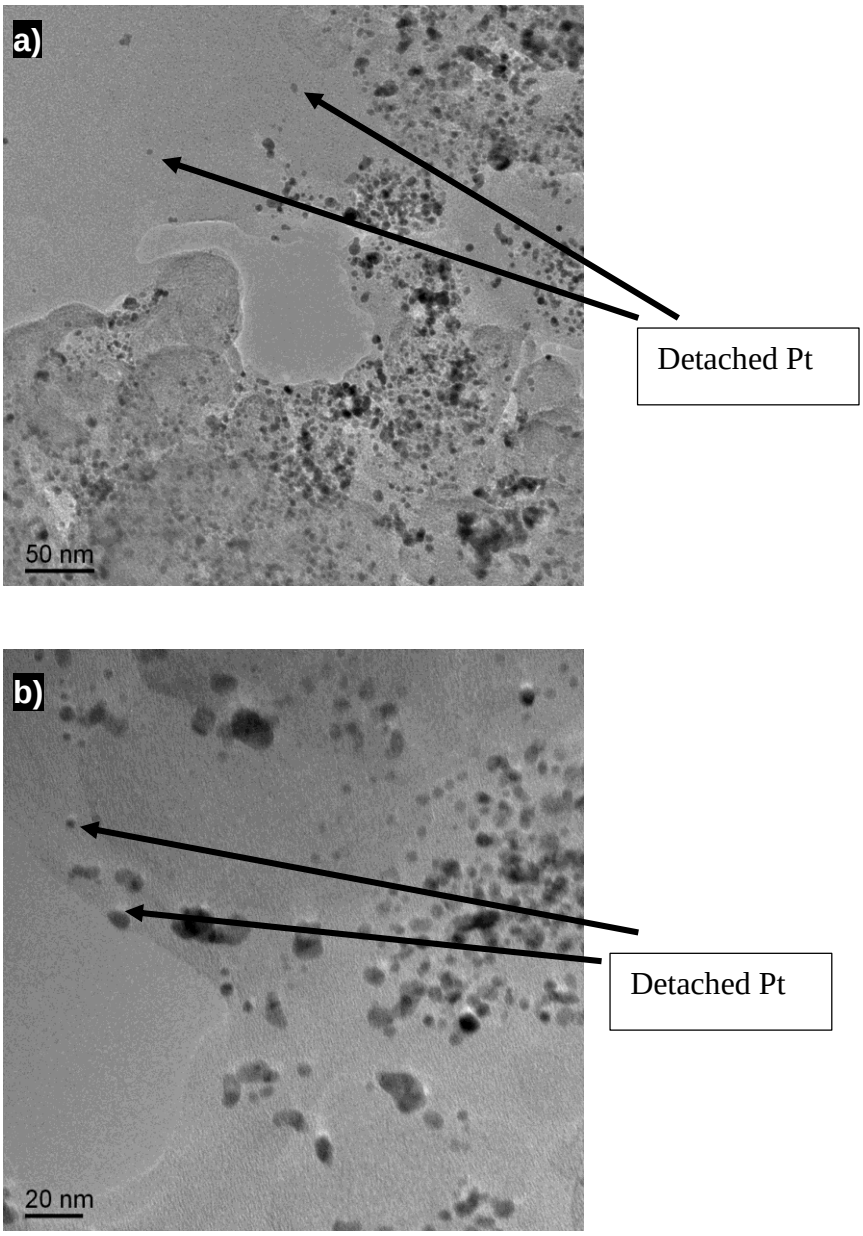

Figure 4.7 Detached Pt particles in CL with 3M ionomer in water solution

CL inks with various I/C ratio were painted onto a ~5mm wide Teflon strip as samples. To avoid contamination, the samples were outgassed by vacuum pumping at 120°C. Most of the humidity will be removed during this process.

Using the nitrogen adsorption technique, pores larger than the nitrogen molecular of 3.5 Å diameter can be observed [120]. Figure 4.8 illustrates the isotherms obtained for 30% Pt on Vulcan XC-72 carbon powder in 3M ionomer CLs with 0.2, 0.8 and 2.0 I/C ratios. All these isotherms are type II adsorption according to the IUPAC classification [120, 121]. This suggests that the samples contain macropores where monolayer and multilayer nitrogen adsorption can take place. At very low relative pressure (P/P_0), the steep rise indicates the presence of micropores (<20Å) and the monolayer coverage is the dominant process. As the partial pressure increases, the inflection point indicates the complete filling of micropores and the multilayer process proceeds. In this region, the mesopores in between the Pt/Carbon agglomerates are filled. As the partial pressure reaches unity, the sharp increase is due to the rapid filling with capillary condensation. Also, the lack of a plateau region at higher pressure indicates the existence of macropores in the samples. After the pressure saturation is reached, desorption is carried out. The samples exhibit a hysteresis between the adsorption and desorption isotherms. The shape of such hysteresis provides more information on the sample's structure, such as pore geometry, pore size distribution and connectivity. According to the IUPAC classification, the isotherms follow the behavior of the H3 type hysteresis. This shape implies two things: first, the existence of aggregates of particles that form pores with non-uniform size and/or shape; second, the

limited amount of large pores trapped between smaller pores. The different behavior during adsorption and desorption inside the pores results in the hysteresis [120].

The result shown in Figure 4.8 reveals that a larger amount of nitrogen was adsorbed as the I/C ratio decreases. This can be due to more complete ionomer coverage over the carbon agglomerates and infilling of ionomer in between the agglomerates, which hinders the nitrogen adsorption. Also, there is no significant decrease of the amount of gas adsorbed in the micro-pore filling region (before the infliction point). This indicates that the 3M ionomer loading does not have a significant impact on the coverage and filling inside the micropores. Indeed, earlier studies [31, 122] have reported that due to the polymer particle size, Flemion PFSA was unable to penetrate the primary pores (<40nm). Therefore, the Pt that is inside these pores is inaccessible to gas and cannot take part in the ORR reaction. Furthermore, all isotherms with the various I/C ratios exhibit the same type of hysteresis indicating that the ionomer loading has no strong effect on the CL pore network texture.

For the total surface area measurement, Brunauer–Emmett–Teller (BET) theory was used to analyze the data. First of all, the surface area of the Teflon substrate was measured to be 0.5±0.11 m^2/g, which is negligible compared to the surface contribution of the CL samples. Figure 4.9 shows the dependence of total surface area on I/C ratio. Results indicate that the surface area decreases as the ionomer content increases. This can be due to the more complete coverage and filling of the ionomer in between the carbon agglomerates, blocking high surface area adsorption sites.

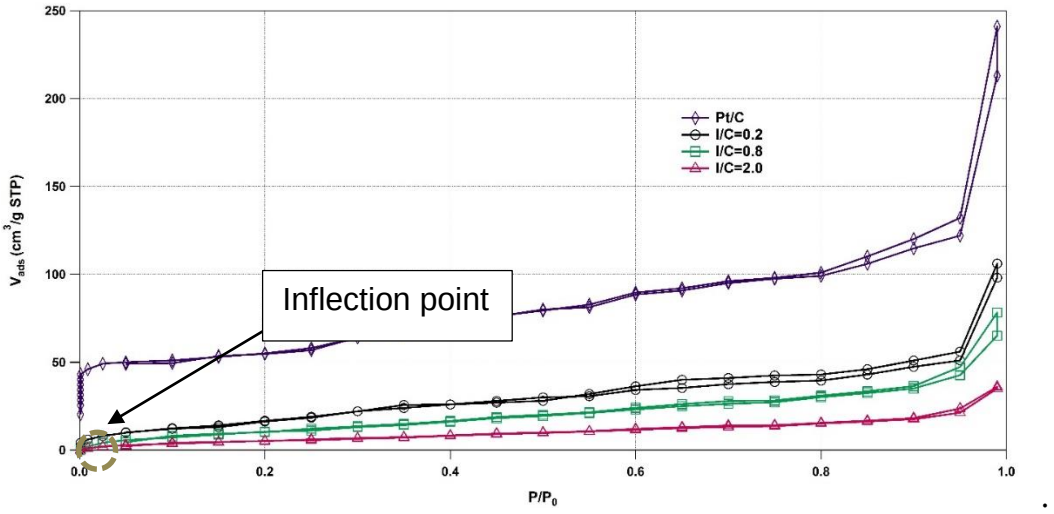

Figure 4.8 Nitrogen adsorption/desorption isotherm of 30% Pt/Carbon and 3M CLs with various I/C ratios.

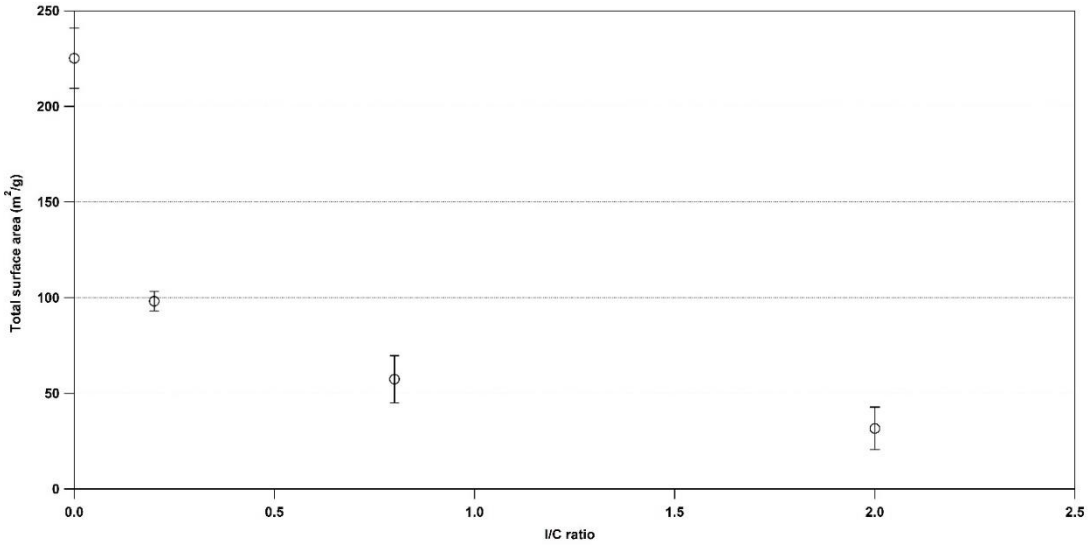

Figure 4.9 Total BET surface area of 3M ionomer CLs with various I/C ratios

Earlier TEM images showed that at lower I/C ratio, more vacant secondary pore (>40nm) structures were observed (Figure 4.3a, 4.3b), providing a larger surface on which the nitrogen molecules are adsorbed. As the ionomer content increases, the polymer enters these secondary pores and partially or fully fills up the void spaces, reducing the surface area (Figure 4.3c, 4.3d).To be noted, the nitrogen adsorption BET method only accounts for the micro- to macropores (2nm-100nm). Therefore, the effect of ionomer inside the larger pores (>100nm), which were observed in the previous TEM studies, are not represented in the total BET surface area.

The pore size distribution was analyzed using the Barrett-Joyner-Halenda (BJH) approach [120]. The result was normalized with the weight of the CL that was painted on top of the Teflon strip, shown in Figure 4.10. As for primary pores (<40nm), a dramatic loss in volume was observed as the 3M ionomer was introduced into the raw Pt/C carbon (I/C ratio rises from 0 to 0.2). This could be due to the binding effect of the ionomer, connecting the powder particles into a Pt/C and ionomer network and building a more compact structure. As the ionomer content increases (I/C ratio rises from 0.2 to 2), a further loss in the amount of primary pores was revealed. This indicates that the 3M ionomer content does affect these smaller pores. Two possible explanations for this are: first, in contrast with previous findings with Flemion CLs [31], the 3M ionomer is able to penetrate the primary pores and cover the surface of the agglomerates; second, the ionomer itself does not fill into the primary pores, and, instead, the larger amount of ionomer forces the agglomerates together, confining the establishment of such pores. In the secondary pore region, a significant decrease was observed as the I/C ratio increases.

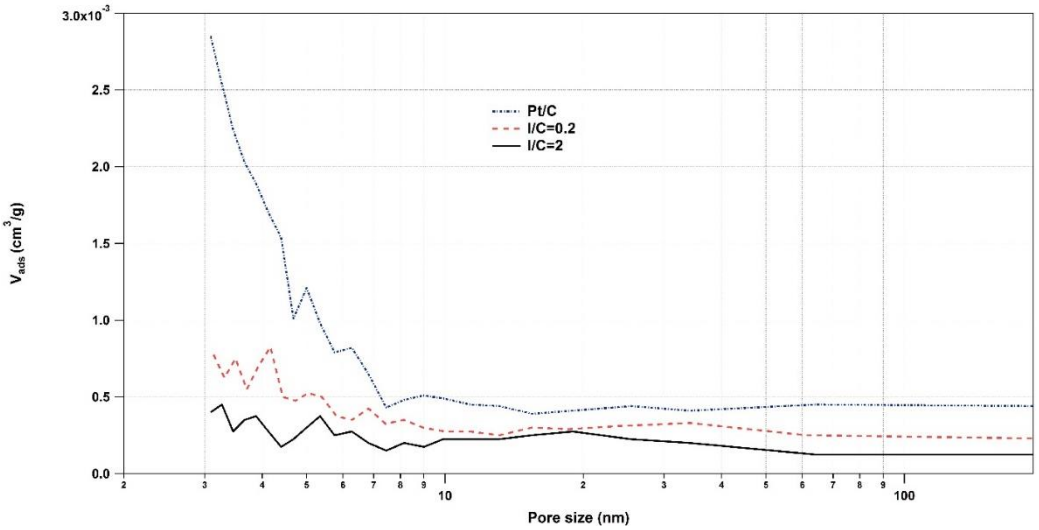

Figure 4.10 Pore Size Distribution of 3M ionomer CLs with various I/C ratios

As shown in previous TEM images (3a-d), there is a more complete filling of ionomer inside these larger pores, which limits the access of the adsorbent gas. Therefore, it is further implied that a higher 3M ionomer content can lead to a better developed ionomer network and hence, a more efficient pathway for proton transport, although a potential blockage for the reactant gas.

4.3 Water Uptake

The CL plays an essential part in the PEMFC water management, especially the cathode CL during the ORR process. The ionomer needs to be hydrated to provide high proton conductivity yet the water produced locally would fill the pores in the CL leading to cell flooding. The study of water uptake in the CL can provide valuable information for the water management in PEMFC.

There has been a significant amount of water uptake studies focusing on the proton conducting membrane. Zawodzinski et al. [20] investigated the water uptake (λ) and transport properties of Nafion 117 at 30°C, reporting λ=14 with the membrane exposed to saturated water vapor and λ=22 with the membrane immersed in liquid water. Bai et al. [123, 124] studied the water uptake of a series of 3M of ionomer membranes including 3M's PFSAs with 825 EW, the bulk membrane form of the ionomer used in the CL of this study. For the recast ionomer inside the CL, there is strong evidence that its transport and morphology differs from the bulk membranes [85, 110, 125, 126]. Siroma et al. [85] reported the conductivity of a Nafion thin film of about 100nm thick was about an order of magnitude less than that of bulk material. Also, the thin film showed a higher activation energy for

proton conduction suggesting an intrinsic change as the ionomer thickness decreases. Concurring with Siroma's study, the proton conductivity of the CL has been reported to be an order of magnitude smaller than the bulk membrane [111,125].

Here, the water uptake of in-house made 3M ionomer CLs with various I/C ratios is measured. We faced a challenge in using the fully liquid immersed method due to the fragile nature of the CL samples. Therefore, samples were suspended in water vapor with different water activities.

Homemade CLs with different I/C ratios (0.2, 0.8, 1.2, 2) were prepared. For alcohol based 3M ionomer CL ink, 30% Pt/Vulcan carbon powder and 5% 3M ionomer 825EW in alcohol solution were mixed to certain I/C ratios. As for the water based 3M ionomer CL ink, 30% Pt/Vulcan carbon powder was mixed with 5% 3M ionomer 825EW in water solution. The ink was then stirred overnight and sprayed onto 5cm^2 Teflon backings.

The CL coated Teflon pieces were then suspended over P_2O_5 for 7 days to dry out. The weight of the completely dried out samples were measured at a fast pace in order to avoid the re-humidification of the CLs in the air as much as possible. Afterwards, the samples were suspended over aqueous lithium chloride solutions in sealed glass vials under room temperature. The samples were suspended for 7 days to reach equilibrium and weighed.

The water uptake, which represents the average number of water molecules associated with each sulfonic acid charge site, was calculated using the following equation [127]:

$$\lambda = \frac{\frac{(W_{wet}-W_{dry})}{W_{dry}}\times EW\times 100}{M_{H_2O}\times Ionomer\ wt\%} \qquad (4.1)$$

W_{wet} is the weight of the hydrated CL; W_{dry} is the weight of the completely dried out CL samples; M_{H2O} is the molecular weight of water which is 18 g/mol; *ionomer wt%* is the ionomer weight composition, for I/C=0.2, 0.8, 1.2 and 2, the *ionomer wt%* is 12%, 36%, 46% and 58% respectively; *EW* is the equivalent weight of the ionomer.

Figure 4.11 illustrates the water uptake of CLs with different I/C ratios compared to that of the bulk membrane from previous studies [123, 124]. Notably, the water molecules are not evenly distributed throughout the CL and the water uptake value λ is an average number. Therefore, when λ<1, it means that some acidic sites might not be in contact to any water molecules, not that a part of the water molecule is attached at each ionic site.

Results show that the thin ionomer film has a much smaller water uptake than that of the membrane. Moreover, the water sorption tends to decrease as the amount of ionomer decreases in the CL. To display the difference more clearly, the water uptakes of the ionomer film and membrane at unity water activity were plotted as a function of ionomer content in Figure 4.12. While λ reaches around 7 for 58wt% CLs, it was reported to be around 11~12 for the bulk membrane [124].

This suggests that there is some sort of surface interaction between the ionomer and the Pt/C agglomeration. For instance, at low ionomer loading, only several layers of ionomers have adsorbed onto the Pt/C surface. At this state, the surface interaction between the Pt/carbon and ionomer, according to the data, strongly weakens the water uptake. We

propose that the surface of Pt/C agglomerates influences the ionomer to assemble in such a way that less sulfonic group is accessible to the water uptake. For instance, a bonding of sulfonic group onto the carbon surface (this should only hold effect when the ionomer coverage is on a monolayer scale) or a certain bundling action of the ionomer chains causing the sulfonic group to be "trapped" inside the hydrophobic backbones. In fact, previous studies have suggested a strong interaction between Nafion's sulfonic group and the functional groups on the carbon surface [75, 128]. On the other hand, it has been reported the actual casting process can affect the ionomer's nanostructure. Devproshad et al.[84] detected a change in hydrophobicity of cast thin Nafion films dependent on the different concentration of ionomer solution used. Recent studies showed that casting a Nafion film onto a hydrophobic surface results in the acidic domains orienting parallel to the substrate. Since the ionomer sites are deeply imbedded, it limits the water uptake and keeps the film from swelling [129].

As the I/C ratio increases, a thicker layer of ionomer film is adsorbed onto the Pt/C surface. The above-mentioned surface influence is less important to the part more distant from the Pt/C surface. Therefore, these ionomer films exhibit intrinsic properties closer to the bulk membranes.

The water uptake measured in our study is significantly lower than that of the bulk membrane. Similar findings have been reported by Iden [128] and Kusoglu [130] in their studies on the CL water uptake. Meanwhile, water uptake studies on recast thin ionomer film showed a less dramatic difference between the thin film and bulk membrane [86, 131]. On the one hand, this further indicates that the interaction between the ionomer and Pt/C

lowers the water uptake. A reevaluation of the CL water uptake calculation could be required, since the recent method ignored the possible water adsorption on the high surface area carbon. Indeed, Iden [128] corrected the water uptake data with a heterogeneous Do-Do model (HDDM), which is a semi-empirical model for analysis of water adsorption on activated carbon. The corrected water uptake result showed a less dramatic difference from the bulk membrane.

One result of a lower water uptake in the CL is that in the presence of excess water, instead of its being sorbed onto the sulfonic site in the ionomers, it may be left in the CL structure. If not removed efficiently, the extra water can stagnate inside the primary and secondary pores, blocking the oxygen from reaching the reaction site, therefore hindering the oxygen reduction reaction. This would be a vital issue for the 3M ionomer CL in particular, since as mentioned below during the polarization study, the 3M cells suffer greatly from mass transfer resistance.

4.4 Polarization Studies

For polarization and EIS experiments, the MEA was prepared using the spray painting method. The Pt loading is 0.4 mg_{Pt}/cm^2 on the cathode and 0.2 mg_{Pt}/cm^2 on the anode. Toray paper 030 (110μm) was used as gas diffusion layers on both the anode and cathode. The cell was assembled in a $5cm^2$ single stack fuel cell hardware (Fuel Cell Technologies, Inc.) with a single serpentine flow pattern. The effect of ionomer loading and relative humidity level were studied. Since the majority of electrochemical loss occurs on the cathode side, for easy comparison in this study, the I/C ratio was varied in the cathode CL

while a standard anode CL (I/C=1, Nafion ionomer) was used throughout all the fuel cell testing. The MEAs were conditioned in the cell at 70% relative humidity overnight. For each RH level, the cell was set at OCV for 30 minutes to reach a steady state before testing. The polarization curve was obtained through the chronoamperometry method. A stepwise decreasing cell voltage from OCV was applied to trigger electrochemical reaction at various overpotentials. For each step, a constant voltage was set for 1 minute to reach the steady state.

For the convenience of data comparison, Table 1 shows both the I/C ratio and its corresponding *Ionomer loading (IP)*. I/C ratio was determined as the ionomer weight to carbon weight ratio using the following relation:

$$\mathrm{I/C\ ratio} = \frac{\mathrm{mg\ Ionomer\ cm^{-2}}}{\mathrm{mg\ carbon\ in\ CL\ cm^{-2}}} \qquad (4.2)$$

IP was determined as the percentage of ionomer weight and the total weight of the catalyst layer, calculated as the following:

$$NFP = \frac{\mathrm{mg\ ionomer\ cm^{-2}}}{(\mathrm{mg\ ionomer\ cm^{-2}})+(\mathrm{mg\ Pt\ cm^{-2}})+(\mathrm{mg\ carbon\ cm^{-2}})} \times 100 \qquad (4.3)$$

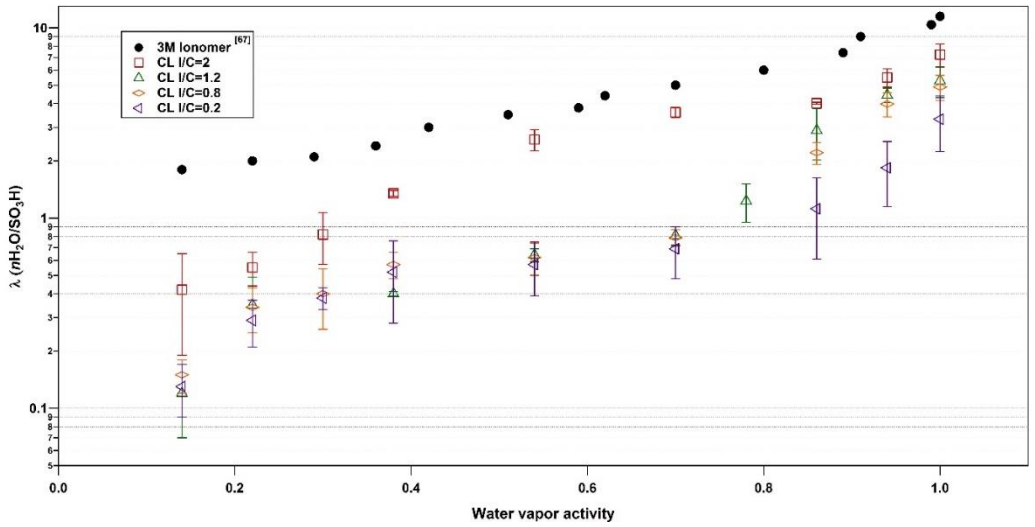

Figure 4.11 Water uptake for 3M bulk membrane (EW825) and in-house made 3M CLs with different I/C ratios.

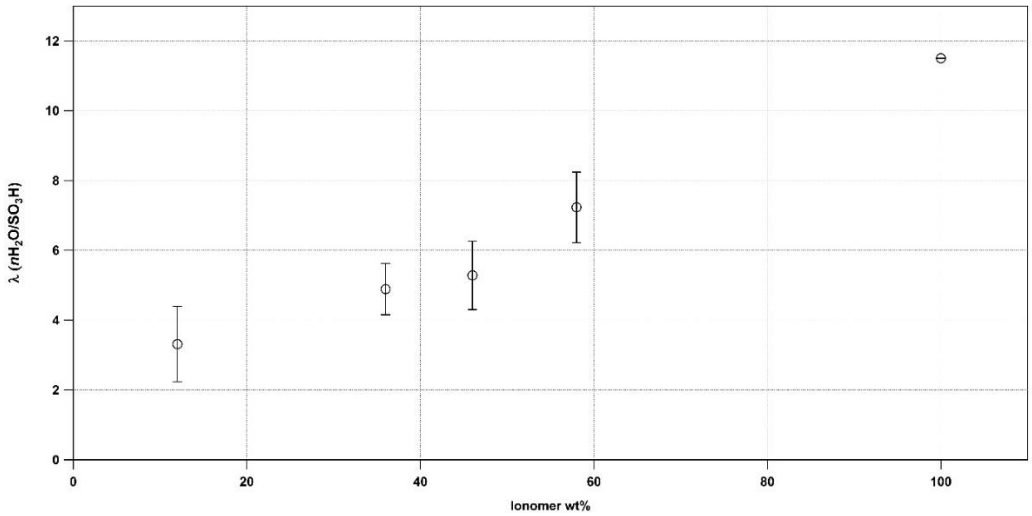

Figure 4.12 Water uptake of 3M membrane and CL at unit water activity as a function of the ionomer weight content.

Table 1. I/C ratio and its corresponding IP value

I/C ratio		0.2	0.4	0.8	1.2	2
Ionomer loading (IP)		12%	22%	36%	46%	58%

Figure 4.13 and 4.14 show the cell voltage and resistance as a function of the current density at 80°C at different RH levels – 35%, 50%, 60%, 80% and 100%. The cell performance was examined under H_2/O_2 in Figure 4.13 and then H_2/Air in Figure 4.14. The flow rate was 1.5 stoichiometry for hydrogen, 2 stoichiometry for oxygen and 2.5 stoichiometry for air. The backpressures were fixed at 13 psi for both the anode and cathode side.

The polarization curves can be divided into three regions: low, medium and high current density range. In the low current density region, the cell performance is dominated by the activation polarization in the cathode; the kinetic loss attributed to the slow oxygen reduction rate is most pronounced in this region. The barrier for the electron transfer reaction causes a steep drop in voltage. In the medium current density region, ohmic loss arises due to the resistive loss in the electrolyte and electrodes. At high current density, the

mass transfer of the reactant gases to the electrode/ electrolyte interface limits the reaction and the current reaches its limiting value.

In analyzing the data, there are several points to be noted. At lower RH level, the ASR reduces more dramatically as the working voltage decreases. This is because, under such dry conditions, the ionomer is extremely dehydrated, and therefore struggling to transport proton through the sulfonate sites. As the working potential decreases, the ORR, produces extra water that is taken up by the ionomer, greatly improving the membrane conductivity. As the working potential decreases, the ASR reaches a steady value, indicating that the cell has reached a steady state humidification level. The decrease of the stabilized ASR upon increase of the RH level further indicates that enough time was given for the cell to reach equilibrium. Second, for I/C range of 0.2 to 2, the cell reached peak performance at 50%-60% RH, and suffers a rather significant drop in performance as RH increased from 60% to 100%. This is certainly different from Nafion CL fuel cells, which are expected to reach peak performance around saturated humidification level under such operating temperatures [132- 134]. This indicates that 3M ionomer fuel cells can operate more efficiently under dryer condition than can those using Nafion. However, the sharp drop amongst most I/C ratio CLs in the high current density region reflects 3M ionomer's high sensitivity to the water content inside the fuel cell. Nonetheless, it is premature to attribute the dramatic mass transfer loss solely to the CL, since the gas diffusion layer plays an important role [135, 136].

The RH at 60% was selected to evaluate the cell performance at various I/C ratios, as shown in Figure 4.15.

Figure 4.13 Polarization Curve and area specific resistance of alcohol based 3M ionomer CL fuel cells at various relative humidity. a) I.C=0.2; b) I/C=0.4; c) I/C=0.8; d) I/C=1.2; e) I/C=2. Inlet gas: H_2/O_2; flow rate: 1.5 stoich/2 stoich; cell temperature: 80°C; back pressure: 13psi/13psi.

a)

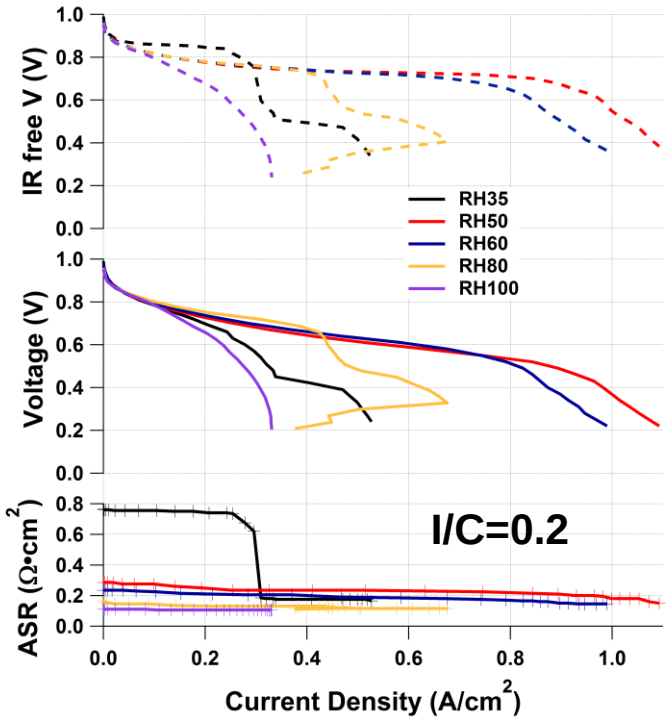

b)

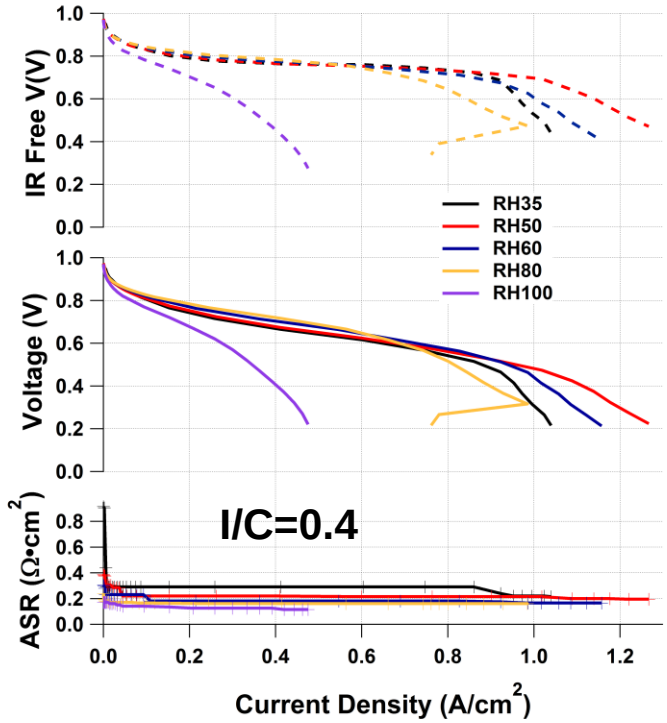

Figure 4.13 continued.

c)

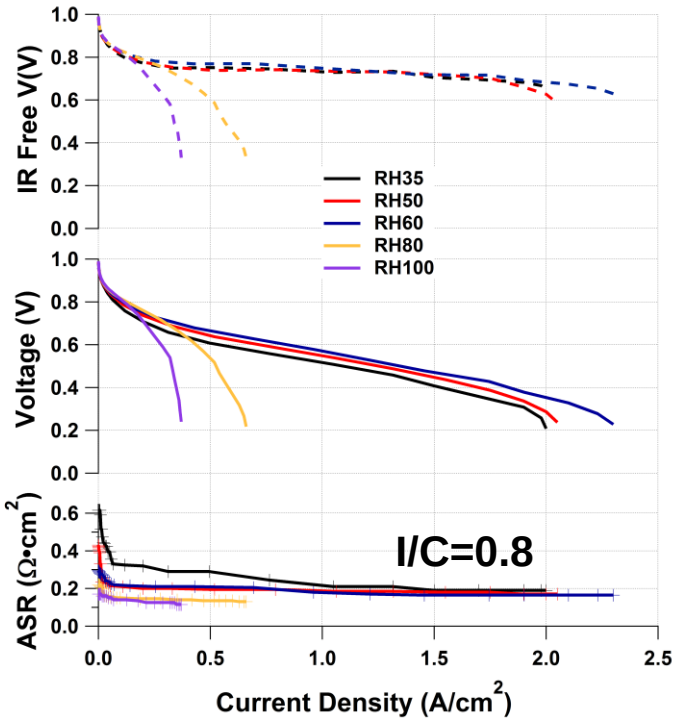

d)

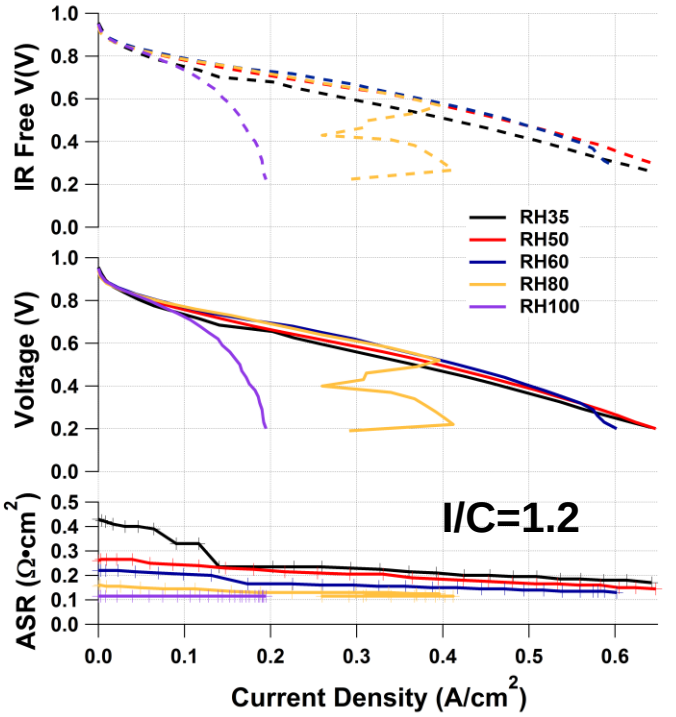

Figure 4.13 continued.

e)

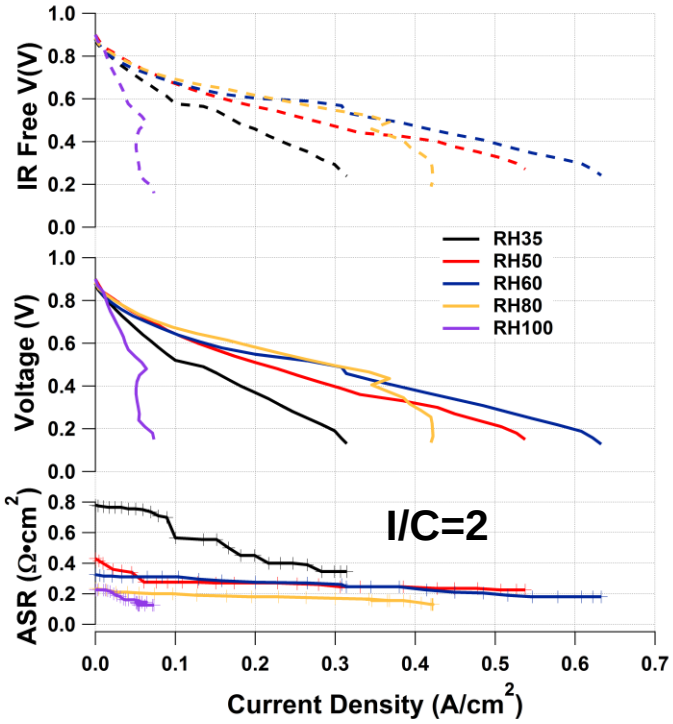

Figure 4.13 continued.

Figure 4.14 Polarization curve and area specific resistance of alcohol based 3M ionomer CL fuel cells at various relative humidity. a) I.C=0.2; b) I/C=0.4; c) I/C=0.8; d) I/C=1.2; e) I/C=2. Inlet gas: H_2/Air; flow rate: 1.5 stoich/2.5 stoich; cell temperature: 80°C; back pressure: 13psi/13psi.

a)

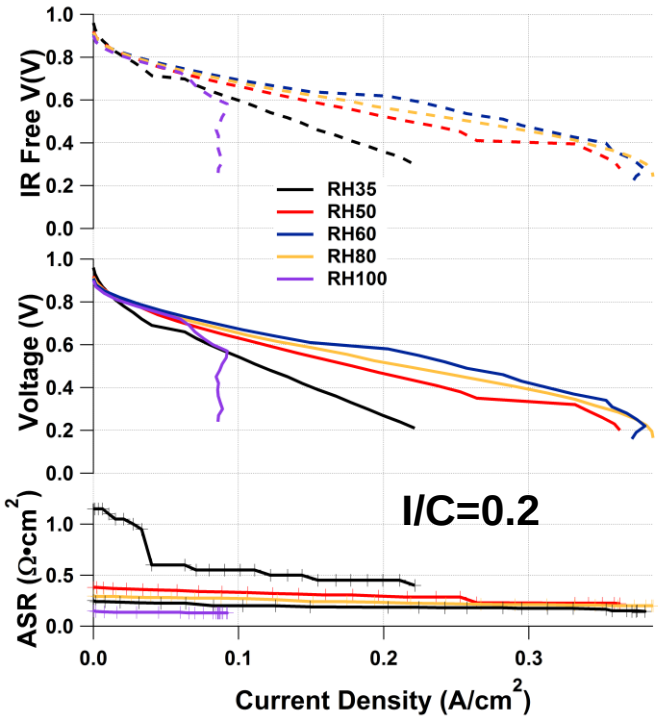

b)

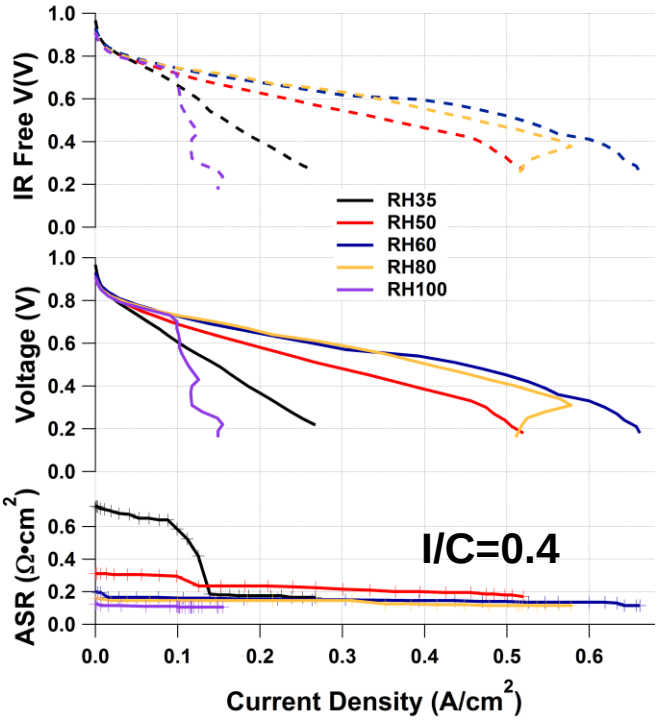

Figure 4.14 continued.

c)

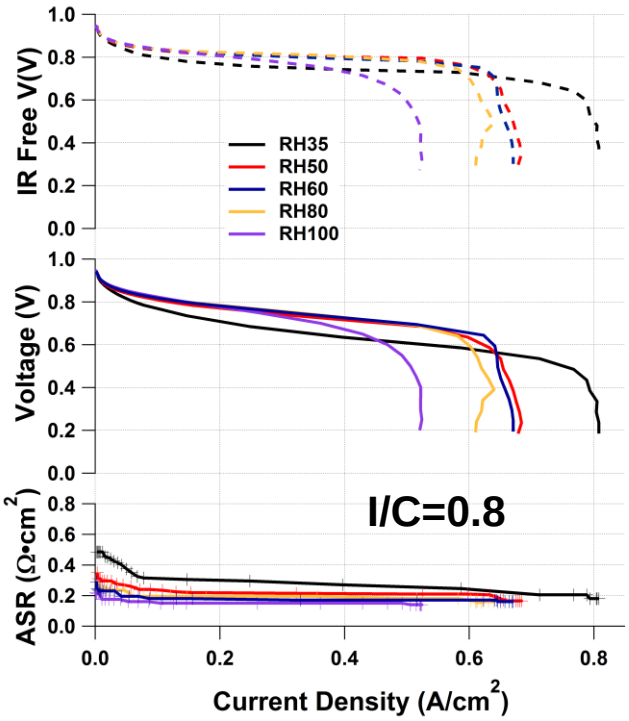

d)

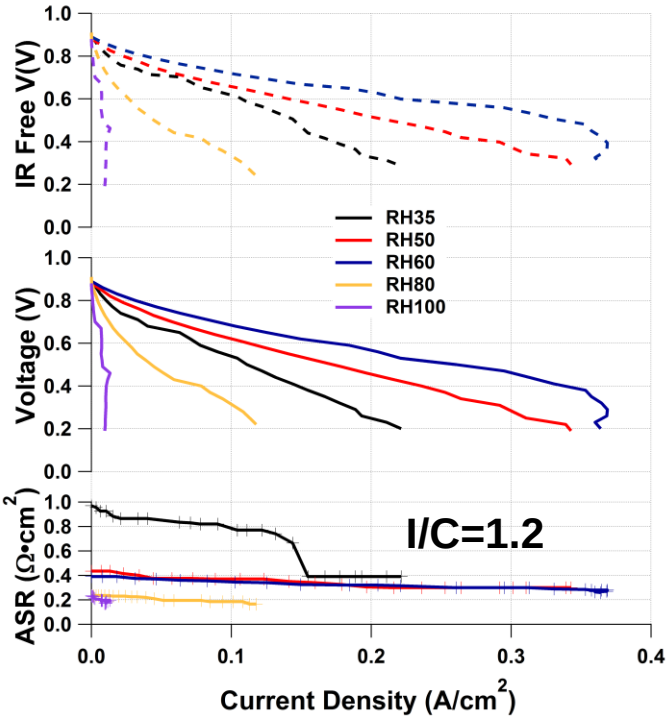

Figure 4.14 continued.

e)

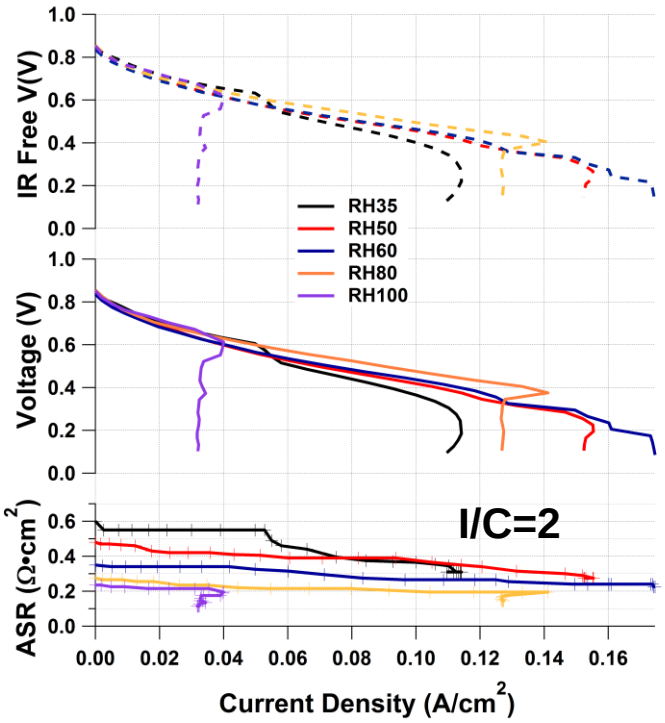

Figure 4.14 continued.

a)

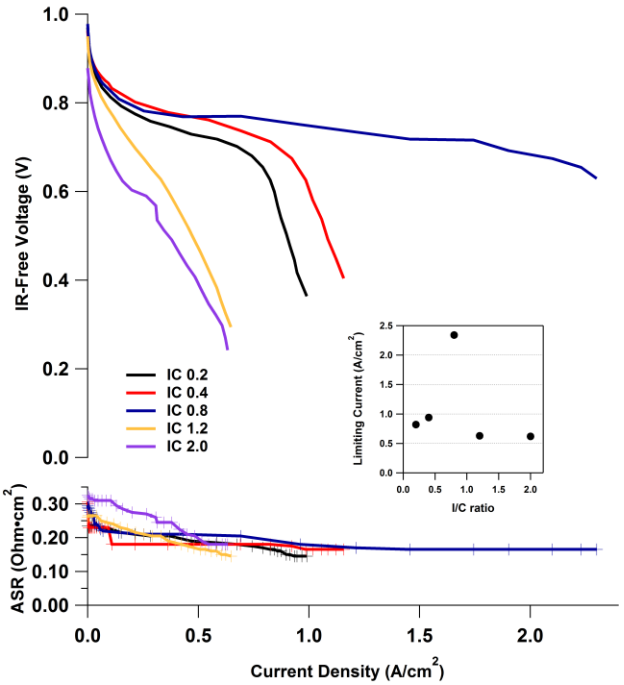

b)

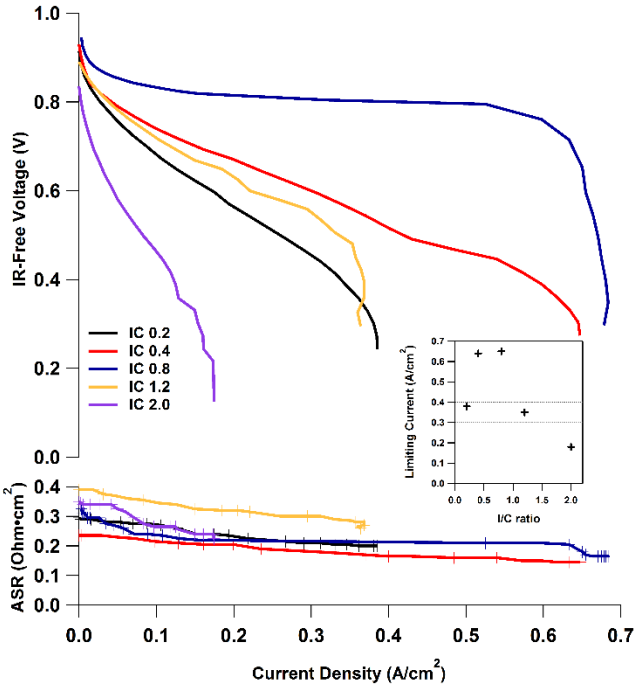

Figure 4.15 Polarization curve of different I/C ratio CL MEAs at 60% RH under a) H_2/O_2 and b) H_2/Air

Under both H_2/O_2 and H_2/Air operation, at lower current density, the fuel cell performance does not change dramatically. The influence of ionomer loading becomes more pronounced as the current density increases. An increase in ionomer loading improves the cell behavior up to I/C=0.8 (*IP* 36%) after which, the introduction of more ionomer diminishes the performance. Comparing this with the prior reports about similar studies on Nafion loading (*NFP*) in the cathode CL, Uchida et al. [115] found that a 33% of *NFP* lead to the optimum cell performance, while Paganin et al. [137], Antolini [138] and E. Passalacqua [97] reported the prime *NFP* to be 30-35%, 22%-40% and 33% respectively. Thus, our results are similar to those obtained with Nafion in this respect.

4.5 Proton Conductivity

To study the proton conductivity of the CLs, AC impedance spectra were acquired with a Biologic SP-150 potentiostat. Hydrogen was fed to the anode/reference/counter electrode and nitrogen through the cathode/working electrode which was potentiostated at 0.2 V vs $E_{reference}$. The frequency ranged from 0.5 Hz to 20,000 Hz with a voltage perturbation of 30mV voltage perturbation. Five spectra were collected at each I/C ratio and RH level to guarantee the reproducibility.

To extract the effective proton conductivity/resistivity from the impedance response, a porous catalyst layer electrode transmission line model was applied. As discussed in the previous chapter, it is assumed that the impedance of the hydrogen electrode is negligible, and the impedance corresponds to the transport of the proton that is produced by the hydrogen evolution occurring on the nitrogen electrode. Z fit and Z sim in the EC-LAB

software were used to analyze the EIS spectra. Figure 4.16 shows the elements inside the cathode porous electrode [79], the model consists of both electronic ($R_{electronic}$) and ionic resistance ($R_{ionomer}$) inside the CL connected by capacitive elements (C_i). Under H_2/N_2 operation, the charge transfer resistance (R_{ct}) is ignored. A representative Nyquist plot obtained with the 0.8 I/C ratio 3M ionomer CL is shown in Figure 4.17. The inductance (L) element in the transmission line model represents a system artifact and was added into the model for completion and improvement of accuracy of the fit. R represents the sum of ohmic resistances of the cell components including the gas diffusion layer, membrane, graphite plates and the contact resistance between each interface. The element Z in the equivalent circuit represents the De Levie porous electrode behavior[80]. For a large number of elements in the transmission line, the impedance of the Z element becomes identical to a finite length diffusion element, and can be described as below:

$$Z_{CL} = R_{CL}\frac{\coth\sqrt{j2\pi f\tau}}{\sqrt{j2\pi f\tau}} \qquad (4.4)$$

R_{CL} is the ohmic resistance across the portion of catalyst layer that is involved in the charging process, j is an imaginary unit and τ is the diffusion time constant. R_{CL} is frequency dependent since at higher frequency the shorter perturbation only penetrates the near membrane CL interface area and therefore only this short area will be involved in the charging process. The catalyst layer electronic conductivity effectively shorts out the ionic pathway. Meanwhile, at lower operating frequency, the sinusoidal voltage pulse can extend its reach deeper from the interface into the CL, involving a larger portion of the CL in the charging process increasing the R_{CL} due to the longer ionic path.

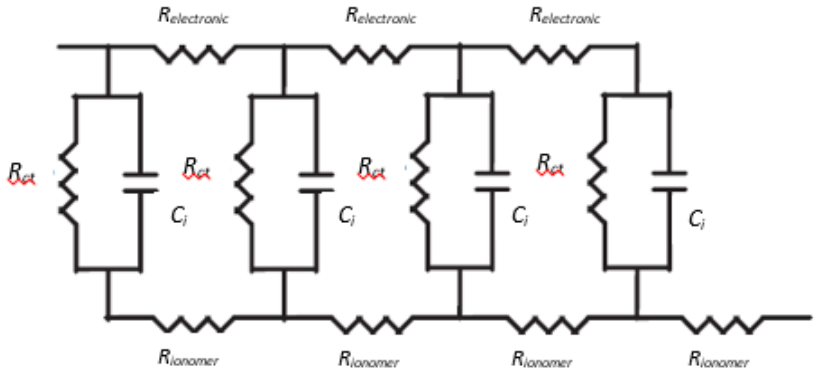

Figure 4.16 Transmission line model of a porous electrode [97]

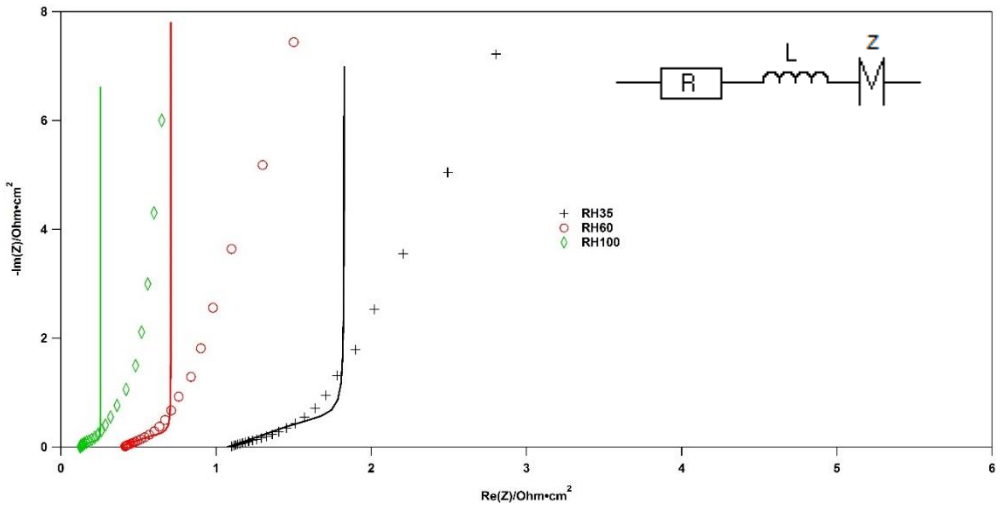

Figure 4.17 Nyquist Plot of I/C=0.8 3M ionomer cathode at 35%, 60% and 100% relative humidity levels and the equivalent circuit fit. The fit to experimental data is shown as solid line.

The inductance (L) element in the transmission line model represents a system artifact and was added into the model for completion and improvement of accuracy. R represents the ohmic resistance of the total cell components including the gas diffusion layer, membrane, graphite plates and the contact resistance in between each interface. Following a Taylor-series expansion of equation 4.4, neglecting third and higher order terms results in

$$Z_{CL} = \frac{R_{CL}}{3} + \frac{R_{CL}}{j2\pi f\tau} \quad (4.5)$$

Therefore, as the frequency approaches zero, the resistance is reduced to one third of the value of R_{CL}. This allows the estimation of the proton resistivity and conductivity in the cathode using a graphical fitting method [108].

As shown in Figure 4.16, the resistors representing the ionic resistance and capacitor representing the CL capacitance are arranged in a ladder-type structure. When the number of elements is infinite and all the resistors and capacitances possess the same value, this equivalent circuit can also be described as a finite length diffusion element. In this study, an equivalent circuit that contains a diffusion element was used to fit the AC impedance data.

The experimental results do deviate from the fitted lines and the deviation becomes more dramatic as the RH decreases. Several reasons have been proposed and discussed by previous studies to cause such deviation [77, 79, 81, 112-114], and are discussed in the CL proton conductivity chapter in this thesis.

The HFR can be extracted from the Nyquist plot in order to calculate the membrane resistivity. HFR is the sum of the proton resistance in the membrane $R_{membrane}$ and the electronic resistance $R_{contact}$ throughout the fuel cell hardware, which is largely due to the contact resistance between the GDL and flow field. The HFR value is obtained by extrapolating the high frequency Nyquist plot end to the real impedance axis intercept. The value of $R_{contact}$ is usually on the order of 25m$\Omega \cdot cm^2$ [107, 139]. $R_{membrane}$ was calculated following the equation below:

$$R_{membrane} = HRF - R_{contact} \quad (4.6)$$

To calculate the membrane resistivity, the RH-dependent membrane thickness is required. Even though the nominal thickness of Nafion 212 is known to be 50μm at 25°C and 50% RH, the actual thickness of the membrane changes due to the water uptake, especially at saturated conditions. Previous studies have developed the relationship between the membrane's water uptake and the cell's RH and temperature [140], described as the following:

$$\lambda = \left[1 + RH^2 \times 0.2352\left(\frac{T-30}{30}\right)\right](14.22RH^3 - 18.92RH^2 + 13.41RH) \quad (4.7)$$

Assuming that the membrane expansion only happens in the through-plane direction since the in-plane expansion is limited by the GDL area. Therefore, the change in membrane thickness can be related to the change in volume [141]:

$$\frac{t_{membrane,wet} - t_{membrane.dry}}{t_{membrane,dry}} = \frac{\Delta V_{membrane}}{V_{membrane,dry}} = \frac{M_{water} \times d_{membrane,dry} \times \lambda}{d_{water} \times EW} \quad (4.8)$$

Therefore, the membrane thickness at certain RH level can be estimated:

$$t_{membrane,wet} = t_{membrane,dry}\left(1 + \frac{M_{water} \times d_{membrane,dry} \times \lambda}{d_{water} \times EW}\right) \quad (4.9)$$

$t_{membrane,wet}$ is the hydrated membrane thickness; $t_{membrane,dry}$ is the dry membrane's thickness; M_{water} is the molecular weight of water (18g/mol); $d_{membrane,dry}$ is the density of the dry Nafion membrane which is 2g/cm^3 for perfluorosulfionic ionomers [142]; *EW* is the equivalent weight of the polymer which is 1100g/mol; d_{water} is water's density (0.97g/cm^3 at 80°C). Since the membrane's thickness is 50μm at 25°C and 50% RH, the dry membrane's thickness can be calculated to be 44μm. From there, the thickness of membrane at certain humidity levels can be calculated. Table 2 shows the water uptake and thickness of Nafion 212 dependent to the RH level. Note that this calculation method of the membrane thickness is under the assumption that the water is present in its free liquid form inside the membrane. Therefore the total volume of the hydrated ionomer is a sum of the volume of the dry membrane and that of the water. This assumption, however, is debatable. It has been previously reported [124] that water was present in three different forms in the membrane according to the humidity level. Bai's study [123, 124] indicated that water is packed tightly to the sulfonic site at low humidity level ($\lambda<2$). Therefore the added water leads to a smaller volume increment than its liquid form. It is after $\lambda>6$, when the water exist in its liquid state inside the membrane. Following this conclusion, the membrane thickness calculation could lead to an error margin in the lower RH levels. Nonetheless, the simplifying approximation is only used to estimate membrane conductivity and has little bearing on the CL results.

The membrane resistivity is then calculated:

$$\rho_{membrane} = \frac{R_{membrane}}{t_{membrane,wet}} \quad (4.10)$$

Figure 4.18 shows the dependence of membrane proton resistivity on the cathode I/C ratio and RH. The resistivity was expected to only be influenced by the relative humidity and stay relatively constant throughout different ionomer contents in the cathode.

However, at lower I/C ratio (<0.5) and 35% RH, there is a difference from the expected value. Two possible reasons can cause such deviation. The first one would be, as mentioned above, at low RH level, the water molecules bind onto the ionomer sulfonic sites and exhibits a non-liquid form. Therefore, error was introduced by using equation 4.9 to calculate the membrane's thickness. Second, this can be due to the transmission line model's deviation from the actual circuit [78]. Therefore, a concise measurement through the R+L+Z transmission line can only be obtained at higher I/C ratios.

The proton resistivity and conductivity were then obtained from the fitted R_{CL} from the Nyquist plot, following the formula below:

$$\rho_{H^+,cath} = \frac{R_{CL}}{t_{cath}} \quad (4.11)$$

$$\delta_{H^+,cath} = \frac{1}{\rho_{H^+,cath}} \quad (4.12)$$

The cathode thickness t_{cath} is 28±2 μm/(mg_C/cm^2) for CLs with I/C ratios smaller than 3 [109].

Table 2. Water uptake and thickness of Nafion 212 at different RH levels.

RH%	$\lambda_{Nafion212}$	$t_{membrane,wet}$ (μm)
35%	3.1	48.6
50%	4.1	50.1
60%	4.9	51.3
80%	7.4	55.0
100%	12.1	62.0

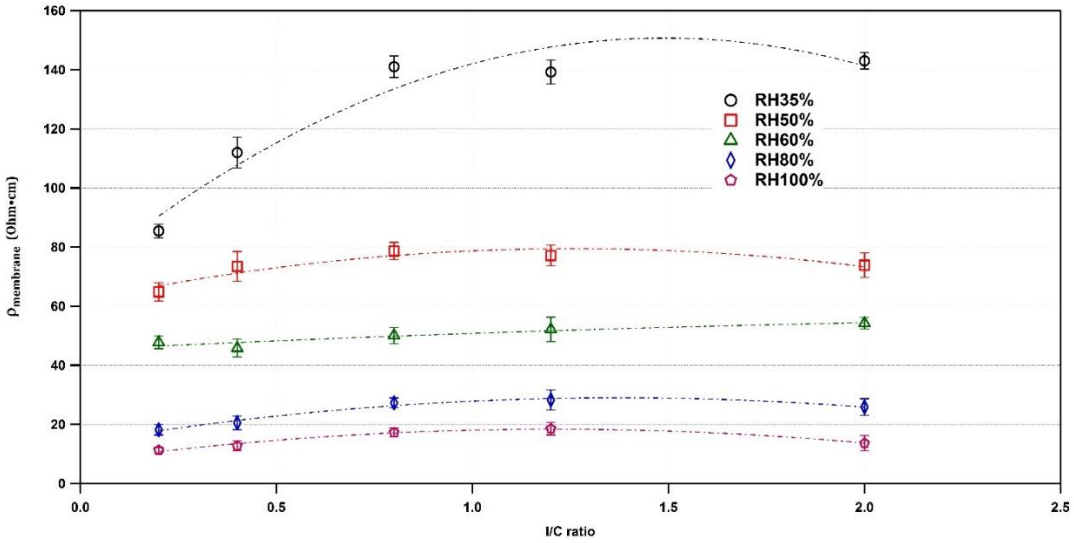

Figure 4.18 Membrane Resistivity at various cathode I/C ratios and RH levels.

Figure 4.19 and 4.20 illustrate the dependence of the CL proton resistivity and conductivity on cathode I/C ratio and RH. The dependence on I/C ratio is stronger at lower RH level (<80%). The conductivity suffers a 5-10 fold loss as the I/C ratio decreases from 2 to 0.2. This can be caused by the interruption of the ionomer structure at lower ionomer content. Compared to the relatively constant value of the membrane resistivity throughout different I/C ratios (as shown in Figure 4.18), it is clear that the significant decrease in the CL proton conductivity is the main contributor to the cell's proton conductivity loss at lower ionomer content. At the same time, the proton conductivity increases along with the RH level. At 80% and 100% RH, the resistivity was too small to be measured accurately at higher I/C ratio (>0.8). During the AC impedance spectrum measurement, there is no reintroduction of water into the cell, unlike in the polarization experiment. This can explain why, even though the ionomer conductivity increases along with the RH level, the polarization performance drops when the RH rises above 60%. As the RH increases from 35% to 60%, the introduction of water humidifies the electrolyte membrane and the recast ionomer film in the CL, increasing their conductivities. As the cell reaches a more saturated humidity level, the performance is reduced over most of the current density range. This suggests that the water introduced by the reactant gas and cell reaction causes difficulties for gas transport from the GDL/CL interface into the CL or vice versa. Therefore, the oxygen diffusion to the catalyst was hindered, causing excessive mass transport and CL ionomer ohmic loss.

Comparing the proton conductivity of the I/C < 0.8 CLs with that of the EW825 3M ionomer membranes (Figure 4.21), the proton resistance in the CLs is significantly higher

than the bulk membrane. This indicates that a high ohmic (ionic) resistance occurs during the cell operation and is mainly contributed by the proton transport through the catalyst layer. In other words, one might expect a larger ohmic loss in the CL compared to that the proton exchange membrane. Furthermore, the difference in the proton conductivity between the bulk membrane and thin film ionomer in the CL implies that there is a difference in the conduction mechanism between the recast ionomer and the bulk membrane. This difference can be attributed to the nano-structural differences between the two ionomer forms. For example, it is assumed that the hydrophilic sulfonic groups on the ionomer side chains are facing out in the ionomer aqueous solution, as the carbon backbone is curved into a cylindrical structure. As the Pt/C powder is introduced to the ionomer, these outward sulfonic groups interact with the functional groups on the Pt and carbon surface, possibly undergoing hydrogen bonding and other electrostatic reactions. These interactions lessen the amount of water uptake in the CL, which was discovered during the water uptake experiment mentioned earlier. Therefore, compared to the bulk membrane, there is presumably less amount of "bulk-like" water structure inside the CL. And since the Grotthus mechanism occurs amongst the "bulk-like" ionic clusters swelled with water, this proton-hopping mechanism should contribute more strongly in the membrane than in the CL. As the I/C ratio increases (>0.8), the proton conductivity of the ionomer in the CL is comparable with that of the membrane. This could be due to the higher ionomer content in the CL building a thicker ionomer film along the carbon agglomerates, and therefore accesses similar properties to the bulk membrane. This is consistent with the previous discussion in the water uptake analysis and with observations from microscopy.

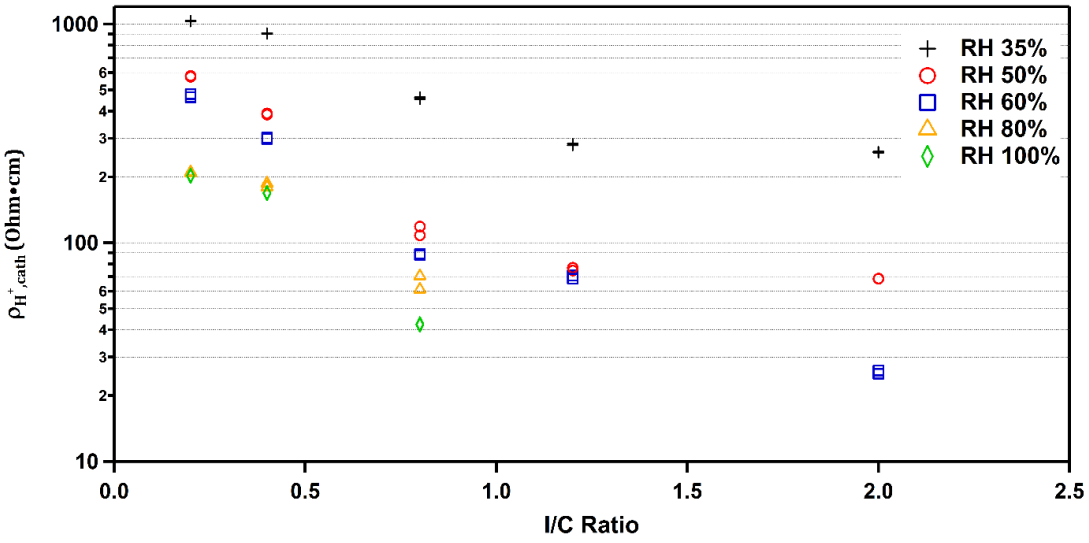

Figure 4.19 Dependence of proton resistivity on I/C ratios and relative humidity levels.

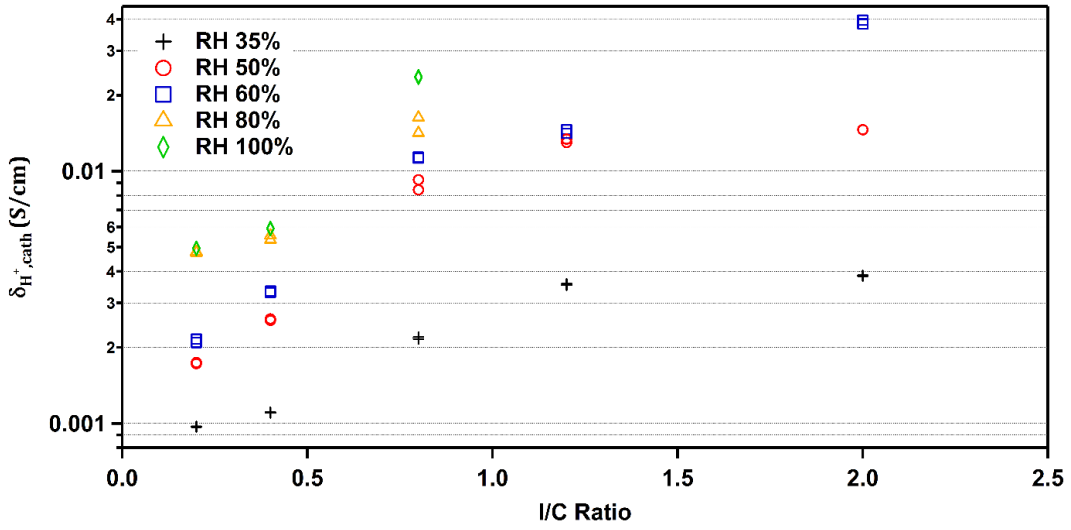

Figure 4.20 Dependence of proton conductivity on I/C ratios and relative humidity levels.

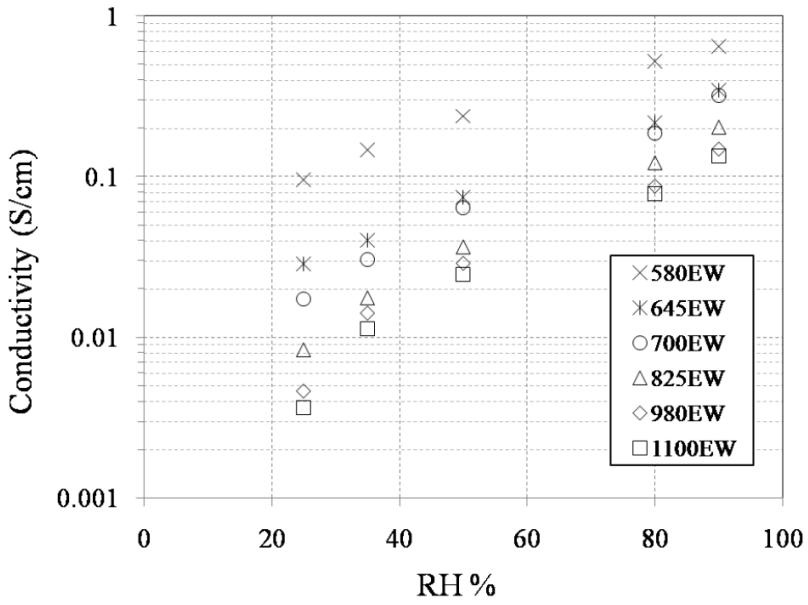

Figure 4.21 Proton conductivity of 3M ionomer as a function of relative humidity at 80°C. [127]

4.6 Tortuosity

The effective tortuosity of the in-house made CL was calculated to help better understand its intrinsic properties. First, the connection between the proton conductivity of the CL and membrane can be formulated as below [42]:

$$\delta_{H^+,cath} = \delta_{membrane} \frac{\varepsilon_i}{\tau} \quad (4.13)$$

Where, $\delta_{H^+,cath}$ and $\delta_{membrane}$ are the CL and membrane proton conductivity, respectively; ε_i is the volume fraction of the ionomer in the electrode which can be evaluated, and τ is the tortuosity. To be noted, $\delta_{membrane}$ represents the proton conductivity of the film form of the ionomer. Since different kinds of ionomer were used in the MEAs during this experiment, the value of membrane proton conductivity was based on previous studies from our group [124, 127].

Equation 4.13 can be rewritten to calculate the tortuosity:

$$\tau = \frac{\delta_{membrane} \times \varepsilon_i}{\delta_{H^+,cath}} = \frac{\rho_{H^+,cath} \times \varepsilon_i}{\rho_{membrane}} \quad (4.14)$$

First, to evaluate the ionomer volume fraction in the electrode [78]:

$$\varepsilon_i = \frac{V_{I,wet}}{V_{cath}} = \left(\frac{I}{C}\right)\left(\frac{m_c A}{m_{I,dry}}\right)\left(\frac{V_{I,wet}}{V_{cath}}\right) \quad (4.15)$$

$V_{I,wet}$ is the humidified ionomer volume; *I/C* is the ionomer to carbon weight ratio; m_c is the carbon loading in the CL (mg_C/cm^2); *A* is the active working area in the MEA, which is $5cm^2$ in this study; $m_{I,dry}$ is the weight of the completely dry ionomer (mg); and V_{cath} is the volume of the cathode CL, obtained as the following:

$$V_{cath} = A \times t_{cath} = A \times f_t \times m_C \quad (4.16)$$

f_t is 28±2 μm/(mg$_C$/cm^2) for CLs with I/C<3. Meanwhile, $V_{I,wet}$ can be calculated from:

$$V_{I,wet} = V_{I,dry} \times \left(1 + \frac{M_W d_{I.dry} \lambda_{CL}}{d_W \times EW}\right) = \frac{m_{I,dry}}{d_{I,dry}} \times (1 + \frac{M_W d_{I.dry} \lambda_{CL}}{d_W \times EW}) \quad (4.17)$$

Where, $d_{I,dry}$ is the density of the dry ionomer, which is 2g/cm^3 as mentioned before; d_W is the water density which is 0.97g/cm^3 at 80°C; λ_{CL} is the water uptake of 3M ionomer CL and EW is the equivalent weight of the ionomer (825g/mol$_{H^+}$).

Combining equation 4.15, 4.16 and 4.17 results in:

$$\varepsilon_i = (\frac{I}{C}) \frac{1}{f_t d_{I,dry}} (1 + \frac{M_W d_{I.dry} \lambda_{CL}}{d_W \times EW}) \quad (4.18)$$

The proton resistivity $\rho_{membrane}$ of EW 825 3M ionomer membrane are shown in Table3.

Table 3. Proton resistivity of EW 825 3M ionomer membrane [124, 127].

RH	**35%**	**50%**	**60%**	**80%**	**100%**
$\boldsymbol{\rho_{membrane}}$ **(Ω·cm)**	55.6	26.3	19.6	8.3	3.4

Figure 4.22 illustrates the proton conduction tortuosity of different I/C ratio CLs as a function of the RH level. As shown, the tortuosity approaches unity after RH reaches 60%. Likely, as the water content increases, more clusters of sulfonic acid sites are connected with water molecules, constructing a less sinuous pathway for the proton transport. Moreover, the tortuosity decreases as the I/C ratio increases. Since the actual percolating ionomer network is closely related to the actual cell working condition, the tortuosity vs the ionomer volume fraction is plotted in Figure 4.23. It further implies that at a certain RH level, the decrease in ionomer volume fraction can cause a disruption in the proton conduction network. This finding agrees with the previous morphology and porosity studies. As shown in Figure 4.3, at lower ionomer content, the ionomer covers around the carbon agglomerates, leaving a large amount of unfilled porous structures in the electrode. Therefore, the proton has to travel around the carbon agglomerates, along the edge of the cylindrical pore structures. Meanwhile, as shown in Figures 4.3c and d, as the I/C ratio increases, pores are being filled with ionomer, building a polymer network amongst the secondary pores. Assuming that the ORR takes place in the secondary pores [31, 115], the protons produced from the anode can travel across the pores through the ionomer and reach the reaction sites more efficiently. The decrease in tortuosity at higher ionomer content further proves that the ionomer network does act as a shortcut for the proton conduction.

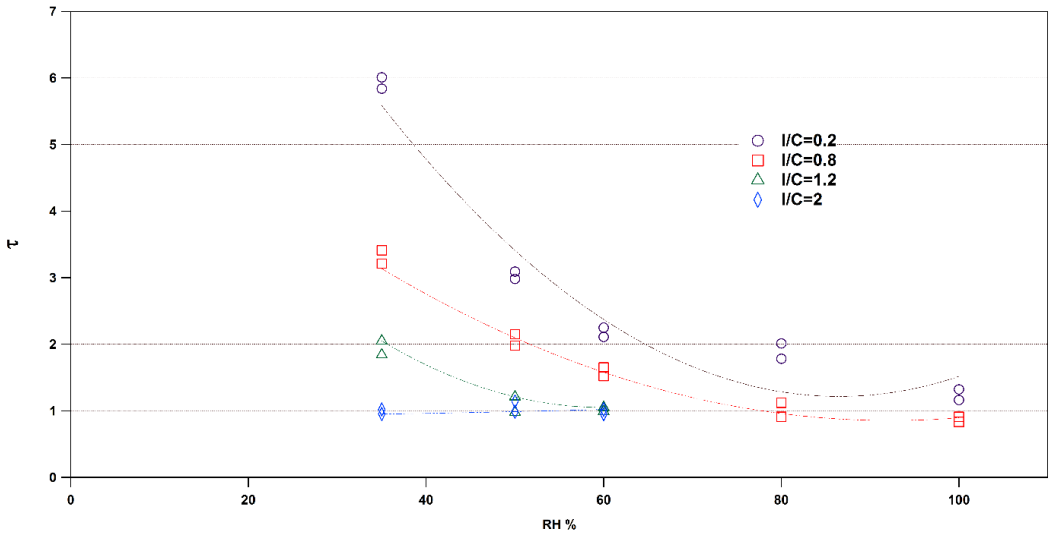

Figure 4.22 Proton conduction tortuosity vs the relative humidity level for I/C=0.2, 0.8, 1.2 and 2 3M CL fuel cells.

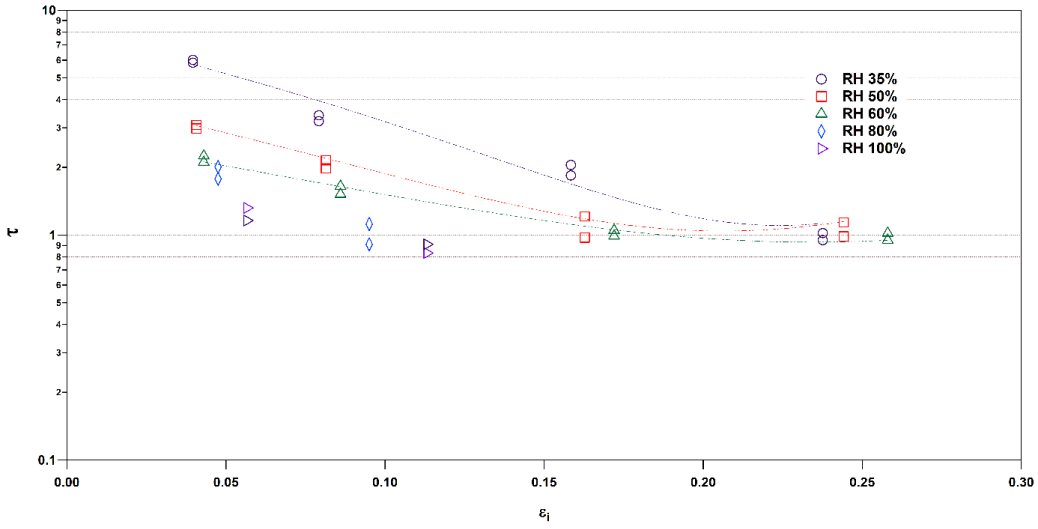

Figure 4.23 Proton conduction tortuosity vs the ionomer volume fraction at 35%, 50%, 60%, 80% and 100% RH.

4.7 Thermal Studies

The properties of Nafion and CL have been studied extensively for low-temperature operation. However, more fuel cell applications require the system to operate at an elevated temperature range, i.e. the radiator technology requires the operation temperature to be well above 100°C [143]. Methanol/air fuel cells exploit higher temperature to limit the catalyst poisoning and methanol cross-over as well as promoting the kinetics of the electrochemical reaction [144]. Therefore, the thermal stability of the proton exchange membrane and CL requires further analysis. Thermal degradation of proton exchange ionomers has been reported [44, 45, 119, 145]. According to the evaluation at Asahi Kasei [119], the 3M ionomer (EW800) membrane possesses a significantly higher decomposition temperature in air (362°C) and argon (393°C) atmosphere than the Nafion (EW950) membrane (319°C in air and 317°C in argon). However, there is a limited amount of work focused on the CL properties at elevated temperature. Previous work has revealed that the presence of Pt will shift the PTFE's decomposition to a lower temperature [44, 45, 127]. In this chapter, the thermal behavior of CL and its components were studied through TGA and DSC. The stability and decomposition was further investigated, and possible interactions between components were revealed and discussed.

4.7.1 TGA Studies

This study shows more details of the interaction between 3M ionomer and the Pt and carbon in the CL. Figure 4.24 represents the comparison of the TGA curves of EW865 3M ionomer membrane and free standing 3Mionomer/Pt/Vulcan XC-72 CL. The operation was

executed under nitrogen atmosphere at 10°C/min. The experiment was executed under nitrogen instead of air to prevent the carbon reacting with oxygen at higher temperature catalyzed by the Pt particles.

The TGA curve shows three distinctive mass loss regions in the 3M ionomer membrane. A small mass loss (<3 wt%) occurs over a broad range from 200°C to 410°C which is mainly attributed to the water content in the membrane. The membrane was pretreated to proton form and vacuum dried at 80°C before undergoing the gravimetric analysis, and therefore a very limited amount of water was detected. The second loss is between 410°C and 460°C followed by the third weight loss region from 460°C to 520°C. According to previous thermal stability studies on Nafion ionomer [44. 45, 145], the second weight loss stage is caused by the desulfonation process of the acidic side chain, releasing sulfur dioxide. The third and final loss region is attributed to further side-chain and final polymer backbone decomposition [146]. Also, compared to the Nafion TGA curve from previous studies (Figure 4.25) [127], the 3M ionomer decomposes at a more elevated temperature, indicating its better thermal stability. This coincides with many previous reports on this PFSA [13, 44, 74, 119].

For the 3M CL, two main mass loss regions were revealed. The first loss appears between 200°C to 400°C and the second weight loss happens in the range of 400°C to 480°C. As shown in Figure 4.24, in the second region, the weight drop is more intense and the sample loses approximately 46% of its weight. Since in this I/C=1, Pt:C 30:70 CL, the ionomer weight percentage is around 42%, the second mass loss region is attributed to the 3M ionomer decomposition. Therefore, the offset temperature of 3M ionomer was shifted

from 410°C to 400°C with the presence of Pt, a minimal difference. Furthermore, above 480°C, the TGA curve reaches a plateau, which indicates the complete decomposition of ionomer with only Pt and carbon left. Meanwhile the mass in the TGA curve of the 3M ionomer membrane continues to decrease as the temperature increases above 480°C. This implies that the ionomer completely decomposes at a lower temperature in the CL with the presence of Pt.

4.7.2 DSC Studies

Differential scanning calorimetry (DSC) was used to analyze the CL and its components further. The experiments were executed below 200°C, to avoid the decomposition of CL and ionomer that was indicated by the TGA study. 3M ionomer thermal behavior from -50°C to 170°C was studied under nitrogen atmosphere, with a heating rate of 5°C/min. The sample was heated up twice, with the second run performed immediately after the first one. During the first heating, as shown in Figure 4.26, water entrapped in the polymer membrane evaporated at around 100°C, displaying an endothermic peak on the DSC curve.

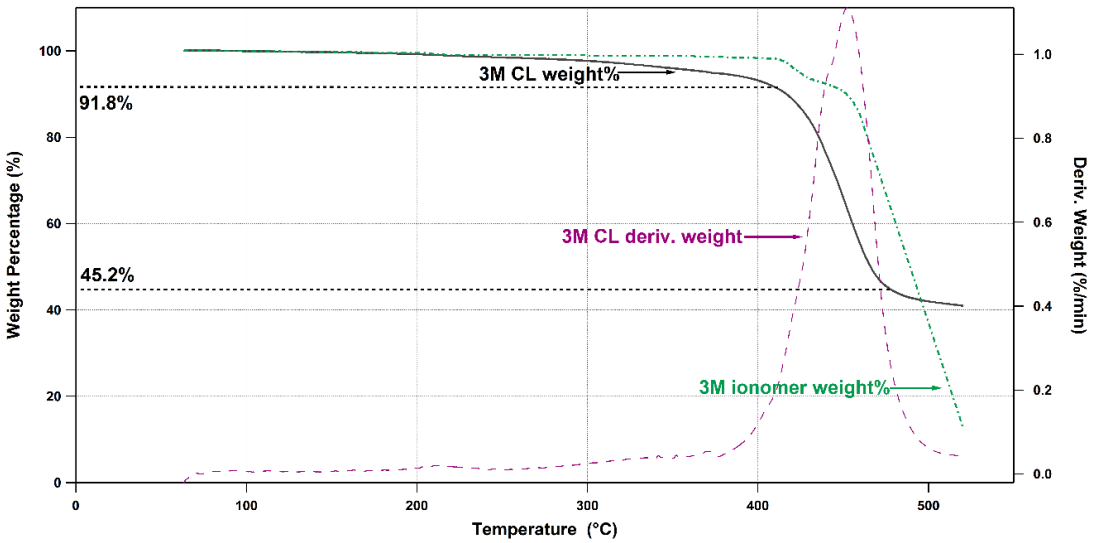

Figure 4.24 TGA traces of 3M ionomer membrane and free standing 3M ionomer CL with 41wt% of ionomer (I/C=1). Samples were heated under nitrogen atmosphere at 10°C/min.

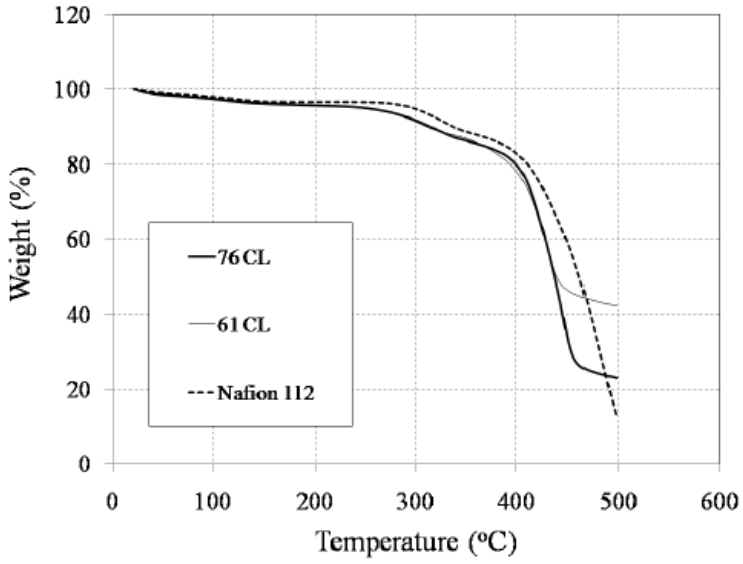

Figure 4.25 TGA traces of Nafion membrane and CLs from previous study [127]. Samples were heated under nitrogen atmosphere at 5°C/min.

The absence of this evaporation peak was not observed during the 2nd heating process, which indicated the complete evaporation of water during the 1st heating cycle. Previous studies have also reported an endothermic peak during the 2nd heating run for Nafion membranes [147- 150]. This was attributed to structural changes inside the ionomer, i.e. the ionomer clusters shifting from order to disorder [147- 149] or molecular rearrangement inside the polymer [150]. However, this endothermic behavior was impossible to observe during the first heating process because of the intense water evaporation, nor was it detected in the second heating process. This implies that either the disordered 3M ionomer groups did not form back into an ordered structure during the cooling process, or the disordering of the ionomer happens at a higher temperature than Nafion.

Further thermal experiments were executed to investigate the CL sample. Previously, Sun [127] observed an exothermic peak around 125°C during the DSC study of a Nafion CL. Each individual component of the CL was then examined under the same condition without such exothermic behavior reoccurring. Nor was it detected in the Pt/ Vulcan XC-72 powder. Therefore, it was assumed that this was caused by some sort of interaction between the sulfonic acid group and the functional groups on the carbon surface. Our study is a continuation of that investigation on the possible causes of this exothermic behavior.

A CL sample with 3M ionomer was examined, as shown in green solid line in Figure 4.27. The CL ink was prepared by mixing 30% Pt/ Vulcan XC-72 and 3M ionomer in alcohol solution. The ink was then dropped into the aluminum DSC sample holder and held at room temperature until the isopropanol evaporated. The DSC was ran under nitrogen environment at 5°C/min.

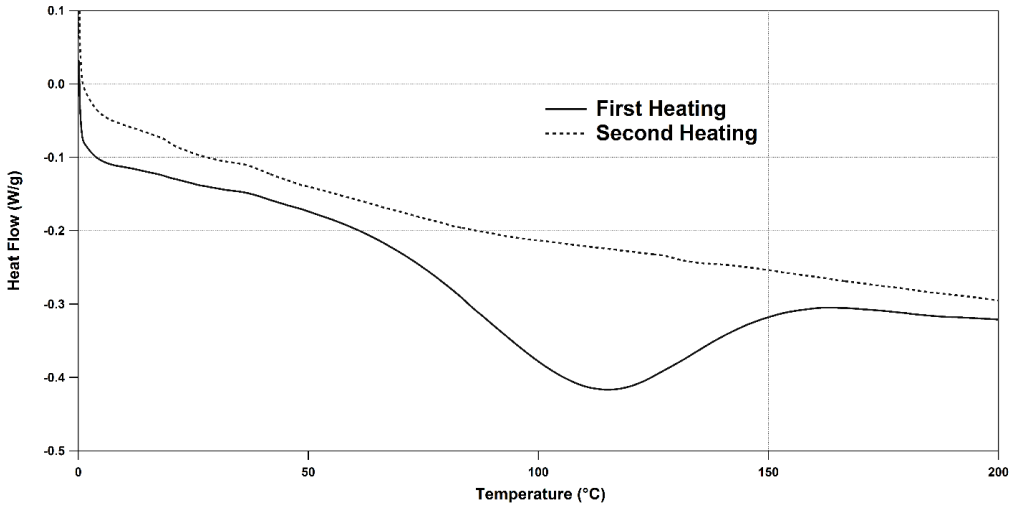

Figure 4.26 Heat flow of 3M ionomer during its first and second heating cycle under nitrogen at 5°C/min.

An endothermic feature was observed around 100°C, which is attributed to a combination of water evaporation and structural changes in the ionic cluster. Around 140°C, similar to Sun's previous report on Nafion CL, an exothermic peak was detected. To further investigate the compounds that lead to such reaction, each individual component was examined. Figure 4.27 illustrates that only in Pt and 3M ionomer mixtures does such an exothermic peak reappear.

The first hypothesis was the existence of interaction between the sulfonic acid groups in the ionomer and the Pt surface, i.e. chemical/physical adsorption during the ink preparation. To further explore this matter, Pt black powder was mixed with 3M ionomer in water solution, Nafion solution in alcohol solution (EW1100) and highly sulfonated poly (arylene ether sulfone) BPSH ionomer in DMF solution. As shown in Figure 4.28, the exothermic reaction was observed in each of these mixtures except the Pt/3M ionomer in water solution. This absence leads us to reevaluate our previous assumption of an interaction between the ionomer and Pt. Perhaps the exothermic behavior could be some sort of chemical reaction between the Pt and the alcoholic solution used during the ink preparation.

Following the presumption above, Pt black powder was mixed with several commonly used solutions for CL ink preparation. A small amount of Pt powder was placed in the aluminum DSC holder and wetted with a drop a DI water. The pan was then filled with the corresponding solution and placed on a hot plate to allow the solution to evaporate. The DSC curves with exothermic peaks, as shown in Figure 4.29, further indicated the presence of interaction between isopropanol, n-propanol, glycerol and dimethylformamide (DMF).

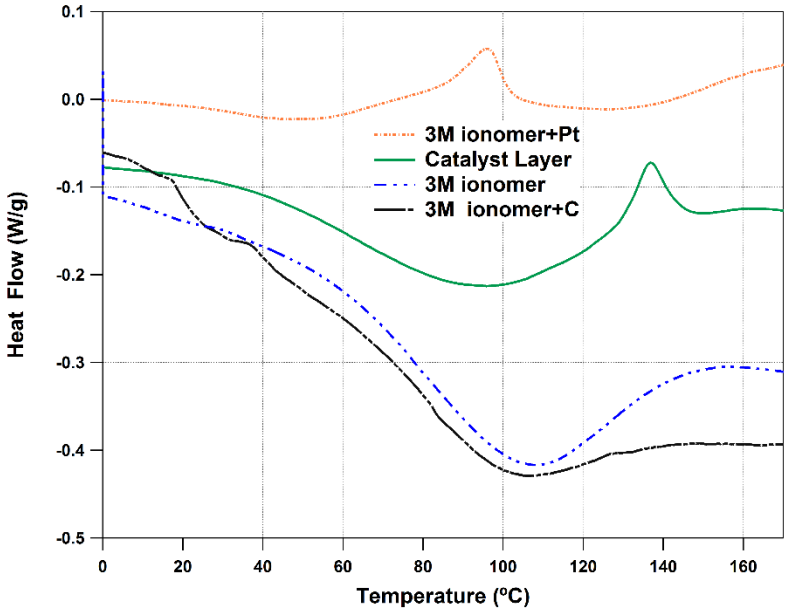

Figure 4.27 DSC curves of 3M CL and its components cross-referenced under nitrogen at 5°C/min.

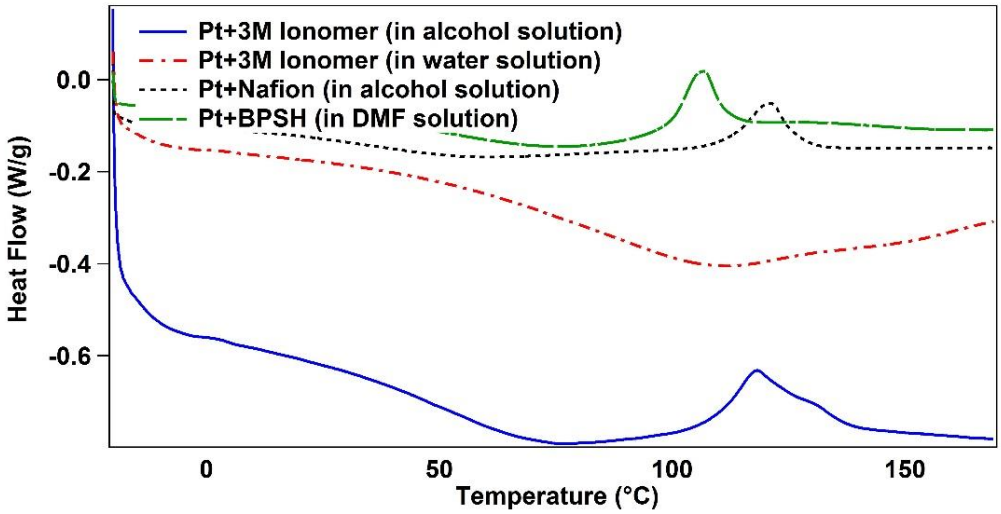

Figure 4.28 DSC curves of CLs with various ionomers under nitrogen at 5°C/min.

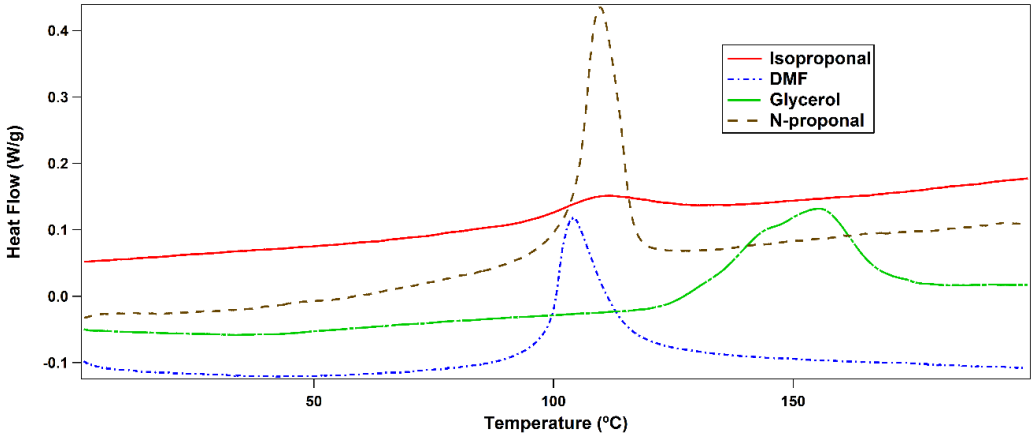

Figure 4.29 DSC curves of platinum and different commonly used solutions under nitrogen at 5°C/min.

One conjecture is that, during the Pt/solution mixing in the DSC sample pan, the molecules in the solution, i.e. isopropanol molecules, were adsorbed onto the Pt surface. This led to a chemical reaction as the temperature elevated during the DSC heating process, e.g. formation of CO_2. Similar adsorption phenomena have been reported and studied previously [151- 153]. The interaction between the metal surface and adsorbate molecules are identified as two types: physisorption and chemisorption. During physisorption, the dynamics are driven by weak attractions between atoms and electrostatic interaction, whereas in chemisorption, the adsorption energy is significantly higher and may even cause distortion in the adsorbed molecule. In the case of alcohol adsorption onto the Pt surface, the adsorption mechanism is still under debate [151, 154]. Our thermal study shows that the adsorbed molecules decomposes above 100°C, which is above the 80°C fuel cell operation temperature. Several questions come to mind. How would this interaction affect the Pt's electrochemical surface area (ECSA)? Would the adsorbed functional group influence the ionomer distribution around the Pt particles? To our knowledge, investigations on such matters have yet to be reported.

4.8 Difficulties

There are several issues that emerge from the structural and electrochemical studies on the in-house made 3M ionomer CLs.

The main challenge in this chapter occurred in the MEA preparation during the electrochemical testing. Several different preparation methods were utilized for the fuel cell fabrication. We first used the common thin film CL method introduced by Wilson [34].

The CL ink was simply painted onto a $5cm^2$ fiberglass decal layer by layer. The CL was placed in an oven at 60°C for 30 minutes after every layer, allowing the alcohol solution to fully evaporate. The sample was then weighed to calculate the Pt loading achieved from each layer. This was repeated until the required Pt loading was reached. The CL was then hot-pressed against a piece of pretreated 4cm x 6cm Nafion 212 membrane at 120°C, 1000kg for 10 minutes. However, the CL would not transfer onto the Nafion membrane. Different combinations of temperature and pressing time were tested with no transfer improvement. The Nafion 212 membrane was further altered into sodium form in order to withhold a higher temperature during hot-pressing. However, this still did not enhance the CL transfer. The CL ink was then directly painted onto a MPL carbon paper, and hot-pressed against the Nafion membrane. Similar issues still occurred. The catalyst coated GDLs were loosely attached onto the membrane which could lead to severe contact resistance. Therefore, we chose to directly hand-spray the CL ink onto the membrane electrolyte. This technique assures a firm attachment between the CL and membrane, and delivers a relatively consistent MEA samples. However, during the hand-spraying process, error can be introduced in two ways. One is the Pt/C could adhere to the inner wall of the spraying unit, which could lead to an inconsistency in I/C ratio throughout the CL. Second, the catalyst coated membrane was weight before and after the spraying process to determine the Pt loading from the weight gain. During the process of transporting the coated membrane from the 80°C hot plate to the scale, the dried membrane can quickly absorb water and introduce error to the calculation for the Pt loading.

Due to the above difficulties we faced during the experiments, a more automatic and stable CL fabrication process would help better guarantee the steady performance of a fuel cell unit.

Chapter 5

Free-Standing 3M Ionomer CLs

The investigation on in-house made 3M ionomer CLs implied the possibility of instability in lab-scale, hand prepared CL samples. A simple way to circumvent such an issue is to fabricate the CL on a larger scale on an automated level. Therefore, 3M Company provided us with machine-made free-standing CLs. Each free-standing CL sheet is 15cmx38cm in dimension. Most information was enclosed with the product. However, certain aspects regarding to the sample material and preparation methods were not provided to us, i.e. samples of raw components (Pt/C powder, ionomer solution), protocol of the CL fabrication.

5.1 Sample Information

The physical and electrochemical properties were studied for free-standing 3M ionomer CLs directly supplied by the 3M company. Three different samples were provided, all directly attached to a polymer backing. The specific information on backing material was not enclosed though it is an inert liner. Table 4 displays the properties of the three samples.

All CL samples are prepared with EA carbon and EW 825 3M PFSA ionomer. They possess identical Pt loadings and I/C ratios with different Pt:C contents. Theoretically, the higher Pt:C ratio samples should be thinner. SEM was used to verify the sample thicknesses, shown in Figure 5.1. The samples were carefully peeled from the backing and attached to SEM sample holders with 3M carbon tape in order to examine the cross-sections.

Table 4. Some properties and information of the 3M free-standing CLs.

Pt:C ratio	Pt loading (mg/cm^2)	Carbon	EW	I/C ratio	Catalyst thickness (μm)
30:70	0.25	EA Carbon	825	1	19.08
50:50	0.25	EA Carbon	825	1	7.62
70:30	0.26	EA Carbon	825	1	3.67

Multiple areas were measured and the average value was used to present the sample thickness. The results are included in Table 4. Since the thickness of the higher Pt:C CL is low and all samples obtain the same Pt mg per square centimeter loading, one would expect the 70:30 Pt:C sample can significantly reduce the ohmic loss.

5.2 Morphology

The near surface structures of the free-standing samples were observed first under SEM. According to the topography shown in Figure 5.2, in the CLs, the 3M ionomer network formed along the carbon agglomerates or particles, forming a porous structure. A secondary pore network was developed, providing a pathway for the reactant gas which greatly affects the mass transfer overpotential. This is comparable with the in-house made 3M ionomer CLs and typical CLs used in nowadays fuel cell applications.

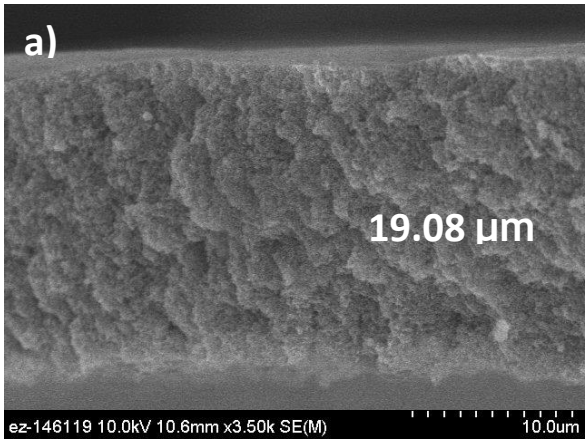

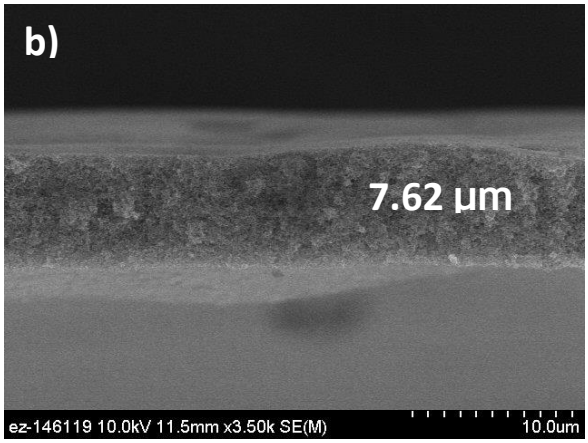

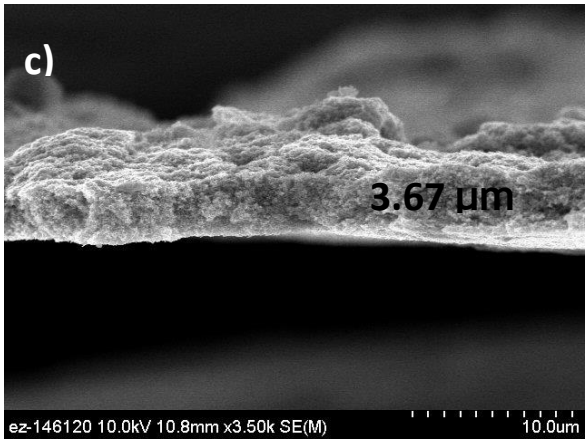

Figure 5.1 Cross-sections of free-standing 3M CLs with 30:70 Pt:C a); 50:50 Pt:C b) and 70:30 Pt:C.

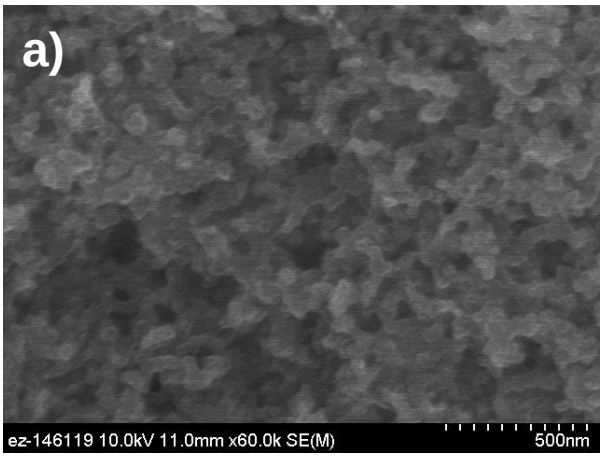

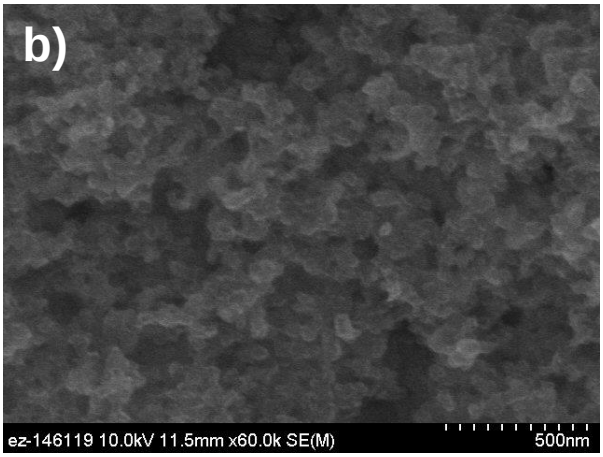

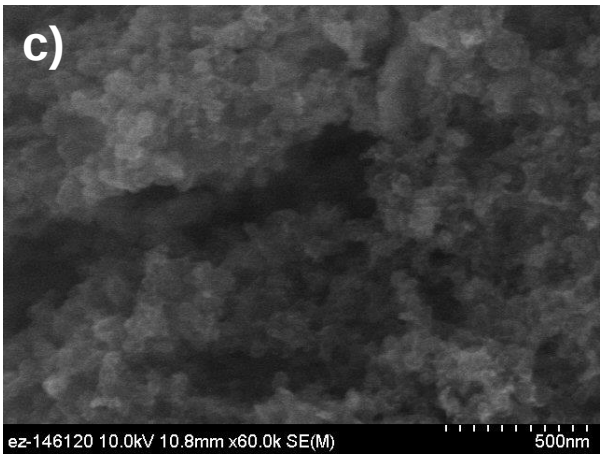

Figure 5.2 SEM images of the free-standing 3M CLs at a) 30:70 Pt/C; b) 50:50 Pt:C and c) 70:30 Pt/C.

Due to the resolution of SEM method, it is difficult to observe the Pt particles under the microscopic images. However, compared to the 70:30 Pt:C CL, we did detect a more continues porous structure amongst the 30:70 and 50:50 CL samples. This could indicate that the ionomer is going through a more strenuous process to bind the CL at higher Pt content.

To examine the CL structures in more detail. TEM was used to study the effect of the Pt loading in the CL. Figure 5.3 shows the fully-embedded free-standing samples. First of all, distinct from the CLs with Vulcan XC-72R carbon, the EA carbon exhibits a ribbon-like hollow structure. Energy dispersive X-ray spectroscopy (EDS) under scanning transmission electron microscopes (STEM) further reveals the component distribution inside the CL. As shown in Figure 5.4, we can detect the pseudo-cylinder carbon agglomerates (red), along with the Pt particles supported on the EA carbon (blue) and ionomer covering over the carbon agglomerates (green)., Both individual Pt particles and coalesced Pt agglomerates were detected in the microscopic images. Second, pores were observed amongst the carbon agglomerates, varying from 5nm to over 100nm in diameter. Third, a large amount of ionomer is distributed around the carbon, along the edge of the larger pores. This implies that the ionomer prefers to bond with the carbon over the Pt, which can be due to some sort of interaction between the functional groups on the carbon surface and the sulfonic groups on the ionomer side chains. On the other hand, the images confirm the existence of ionomer in the secondary pores in the CL, which concurs with the porosity study of the in-house made 3M CL.

Figure 5.3 TEM images of free-standing 3M CLs containing a)Pt:C 30:70; b)Pt:C 50:50; c) Pt:C.

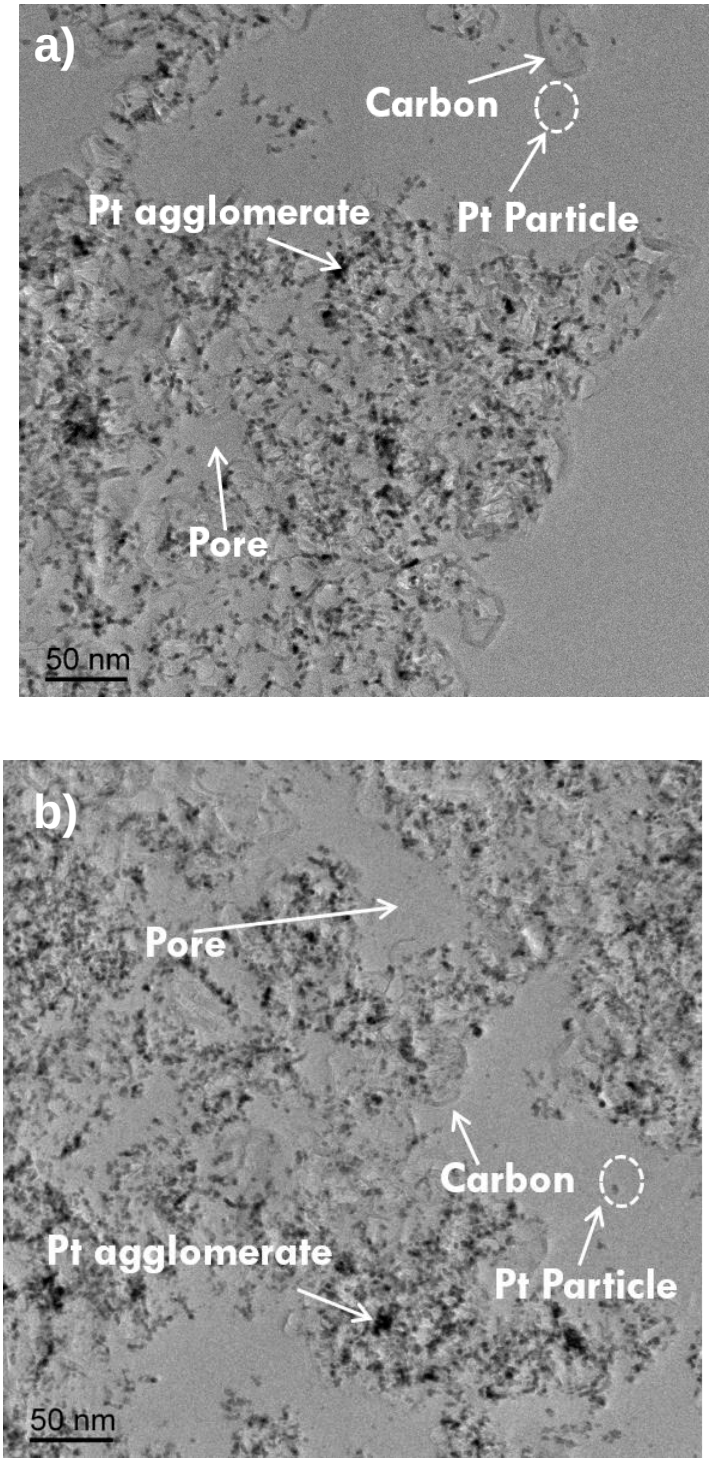

Figure 5.3 continued.

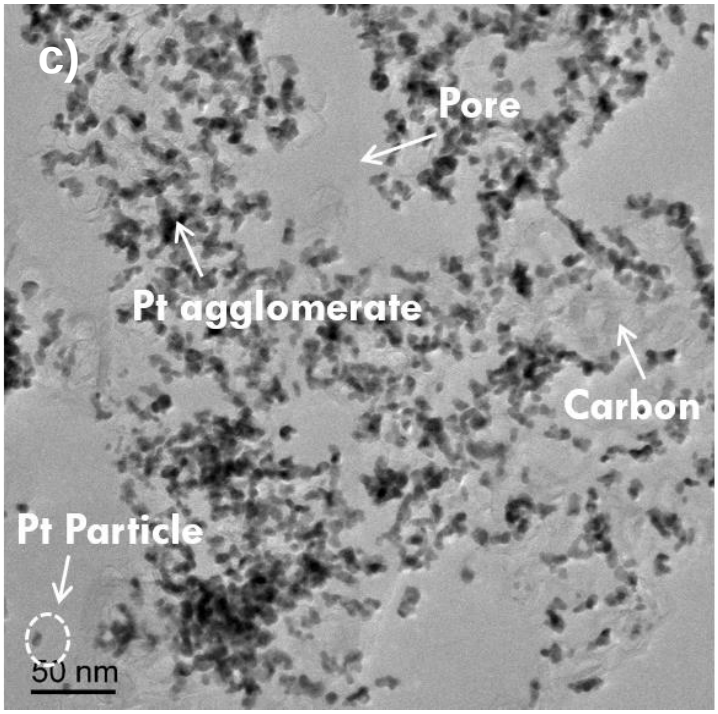

Figure 5.3 continued.

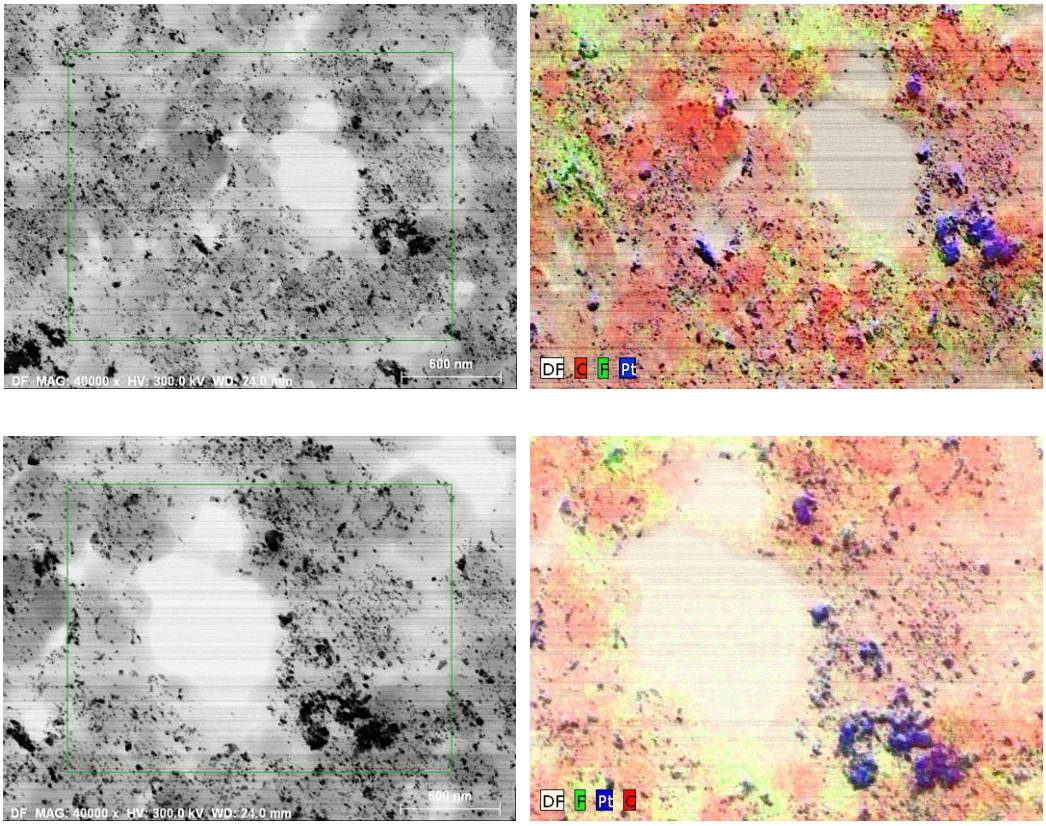

Figure 5.4 EDS image of 50:50 Pt:C CL for composition identification

Under higher magnitude (Figure 5.5), the graphitic layers with spacing in between can be detected. The darker components are Pt nanoparticles and agglomerates. As seen in the higher magnitude images (Figure 5.5), Pt particles can be observed, dispersed on the carbon support. Also, some Pt nano-particles agglomerated on the carbon surface. Furthermore, the Pt dispersed more evenly in the 30:70 and 50:50 Pt:C CLs, building more fine pores than the 70:30 sample. The Pt particle and agglomeration counts confirm this finding, as displayed in Figure 5.6 and 5.7. Since the electrochemical reaction takes place in the 3-phase interface created by Pt, ionomer and carbon, the elevated amount of metal clusters in the high Pt content CLs could cause a larger unutilized Pt surface area. At the same time, the larger amount of secondary pores in the 70:30 provides a more effortless pathway for the reactant gas and water transport, therefore, reducing the mass transfer resistance.

5.3 Porosity

To analyze the porosity of the samples, the free-standing CLs were first carefully peeled from the backing, then packed into the BET sample tube. To avoid contamination during the nitrogen adsorption process, the samples were first outgassed at an elevated temperature (120°C). Nitrogen adsorption and desorption were then performed on each sample, yielding the isotherm shown below in Figure 5.8.

Several points are noteworthy. First of all, the physical adsorption is the familiar type II isotherm, according to the IUPAC classification [121]. This isotherm suggests that the sample is undergoing a multilayer adsorption process, indicating the presence of nonporous or macroporous structure.

Figure 5.5 Higher mag TEM images of free-standing 3M CLs with a) Pt:C 30:70; b) Pt:C 50:50; c) Pt:C 70:30.

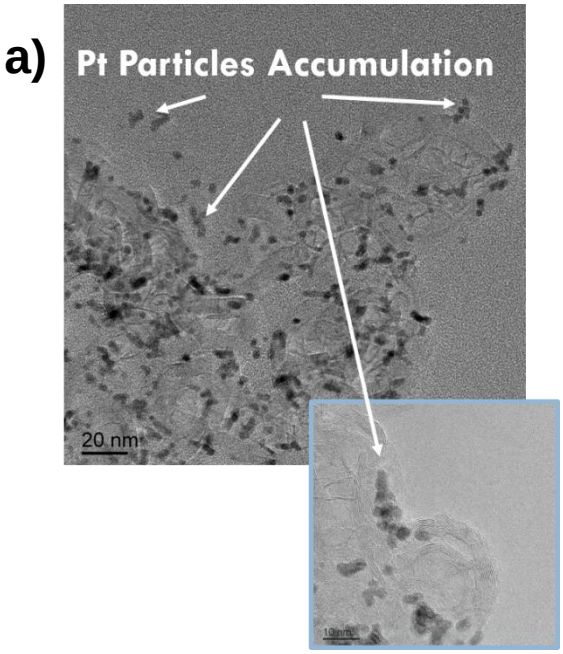

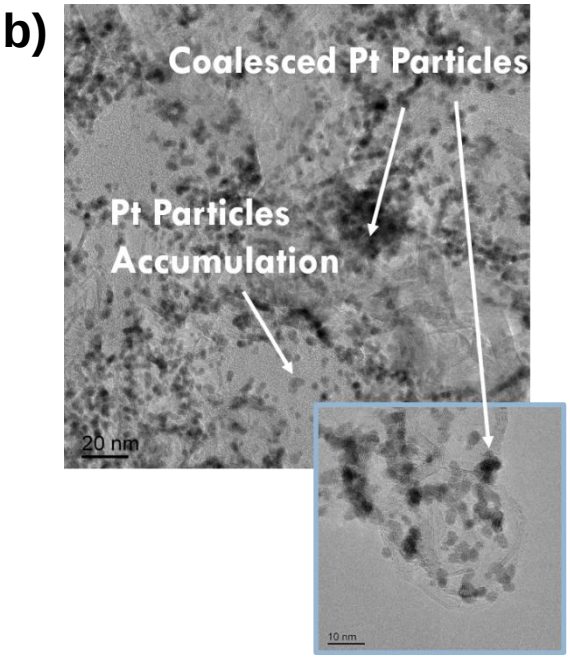

Figure 5.5 continued.

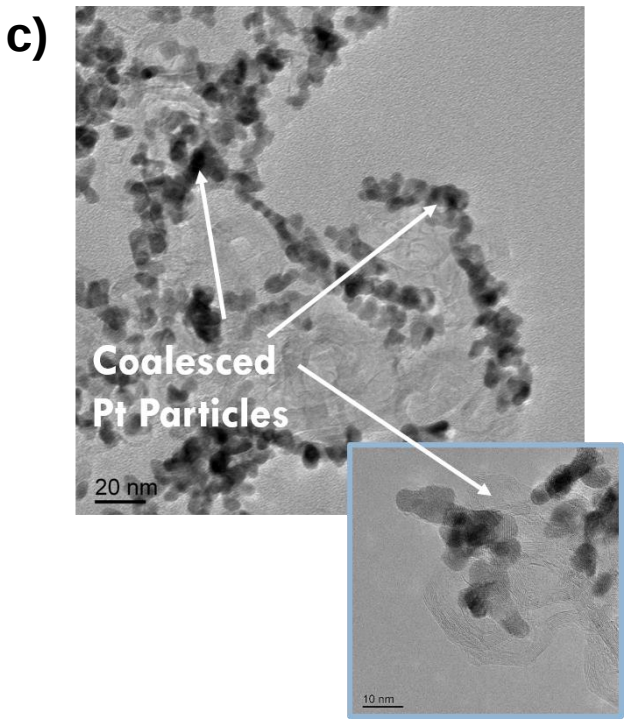

Figure 5.5 continued.

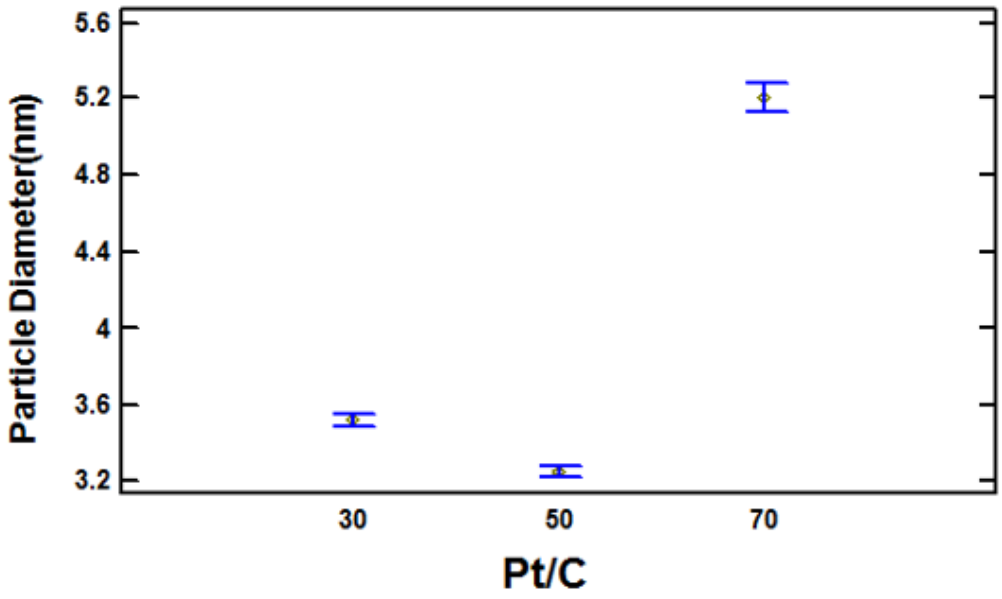

Figure 5.6 Diameter of the Pt particles measured through ImageJ

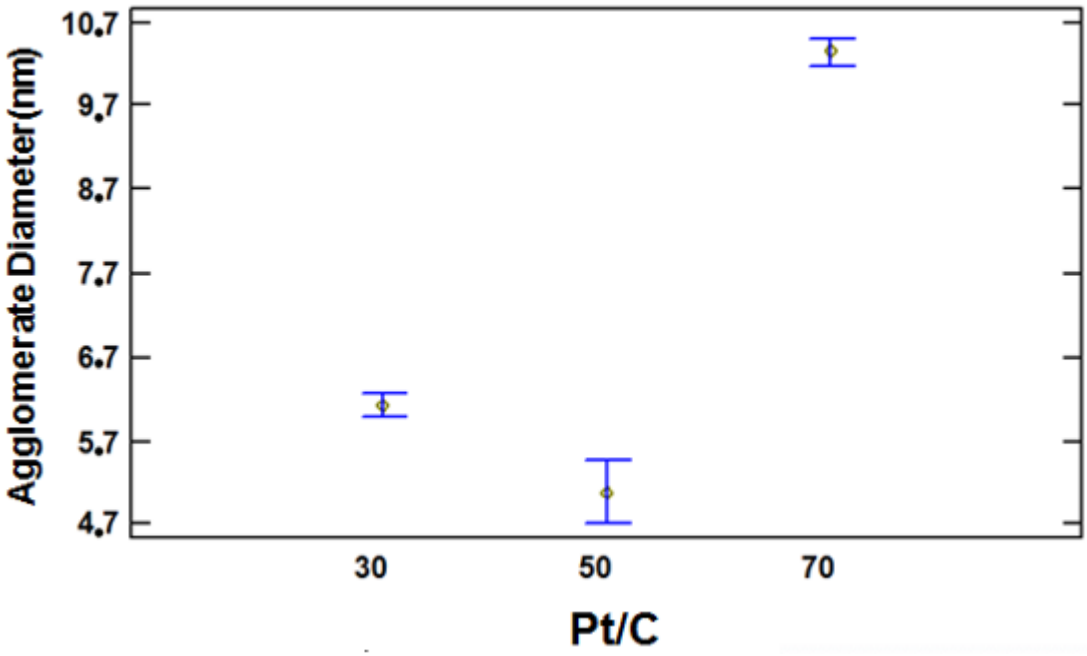

Figure 5.7 Diameter of the Pt agglomerate measured through ImageJ threshold feature

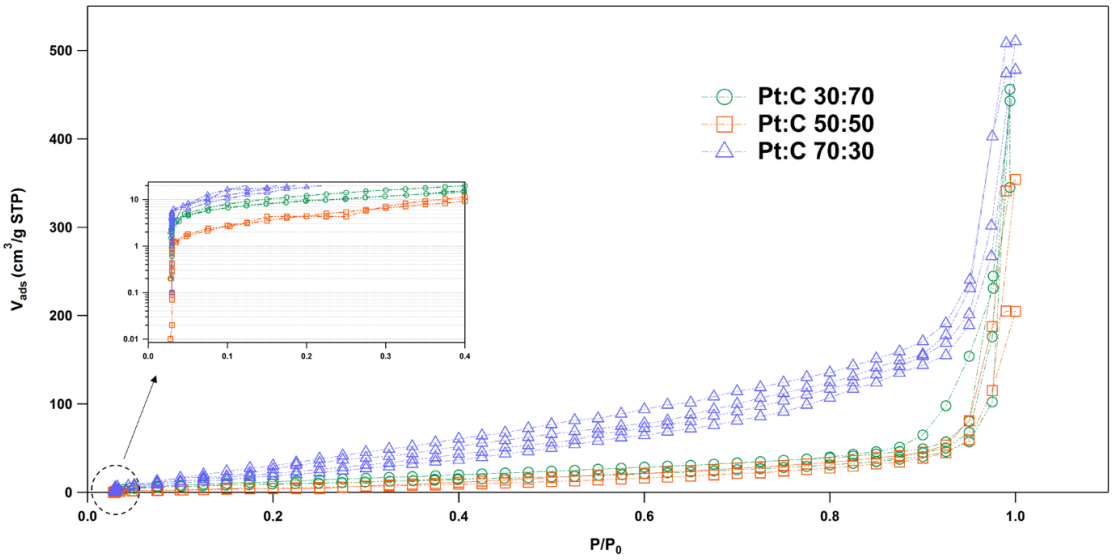

Figure 5.8 Isotherm of the free-standing 3M CLs

In this case, according to the previous morphology study, macroporous surface more likely fits the sample profiles. Second, for the 70:30 Pt:C, a larger amount of nitrogen had been absorbed, implying a more porous structure, which coincides with the previous TEM images. Third, the steep rise in the low partial pressure region indicates the presence of micropores (<2nm). As the partial pressure increase, an inflection point is observed, indicating the start of the multilayer adsorption. In the high partial pressure region, the steep rise is caused by condensation on the apparatus walls near the saturated vapor pressure. The isotherm did not reach a plateau region, suggesting the presence of macropores. Meanwhile, adsorption hysteresis provides us with more information about the mesopores. According to the IUPAC classification, the free-standing CLs follow the H3 type hysteresis, which can be formed due to the existence of wide capillaries with narrow openings between parallel graphitic plates. As data shows, all the CLs exhibit the same types of isotherm and hysteresis. This suggests that, though the Pt:C ratio affects the Pt distribution and agglomeration on the carbon support that was observed in the microscopic study, it does not change the overall CL porous structure, which is a network of meso- and macro-pores amongst carbon agglomerate with micropores within the graphitic walls.

Multipoint BET and BJH method were used to analyze the total surface area and pore size distribution, respectively. As illustrated in Figure 5.9, we perceived a significant loss in the amount of primary pores (<40nm) as the Pt:C ratio decreased. This is especially noticeable from the 70:30 Pt:C CL. If it is assumed that the 3M ionomer mostly exist in the larger secondary pores (40nm-1000nm) [31], the main cause of such a difference in the

primary pore count is the Pt and carbon distribution. As shown in the previous morphology study, the Pt coalesced more intensely in the 70:30 Pt:C sample. This lead to the carbon ribbons forming into a cluster, with Pt agglomerates attached on the surface, as shown in Figure 5.10. The primary pores are constructed between the carbon walls inside these clusters, and therefore show higher quantity in the 70:30 Pt:C CL. These exposed surfaces inside the primary walls also results in a higher surface area during the BET analysis.

5.4 Water Uptake

The water uptake of the free-standing CLs was measured. To prepare the samples, the three different CLs were first transferred from the original backing onto Kapton film by hot pressing at 120°C for 15 minutes. The Kapton-lined samples were then cut into approximately 2.5cm x 2.5cm pieces, suspended over P_2O_5 at room temperature to dry for 7 days. The completely dried out CL slips were then weighed, and further on suspended over LiCl solution with various water activities for 7 days. After the samples reached equilibrium, they were finally weighed and the water uptake was calculated, following the same method used for the in-house made 3M CLs.

The ionomer weight percentage was calculated to be 41.18%, 33.33% and 23.08% for the 30:70 Pt/C, 50:50 Pt/C and 70:30 Pt/C CL, respectively. As shown in Figure 5.11, the 30:70 CL reaches a water uptake of λ=5.2, meanwhile as 50:50 reaches λ=6.1 and 70:30 reaches λ=8.4. For PTFE ionomers, it is typically assumed that swelling occurs when λ>6.

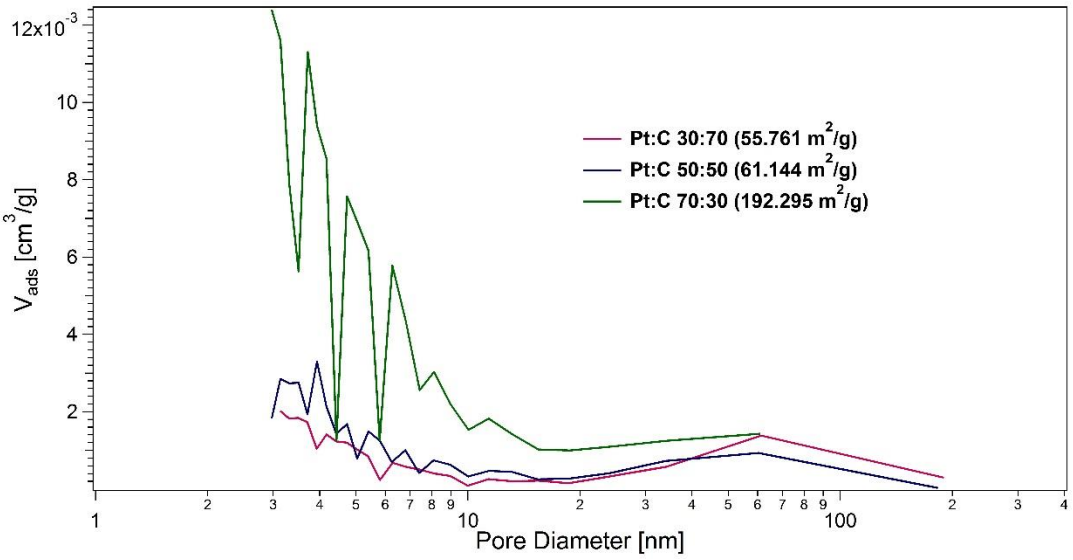

Figure 5.9 Pore size distribution of free-standing 3M CL

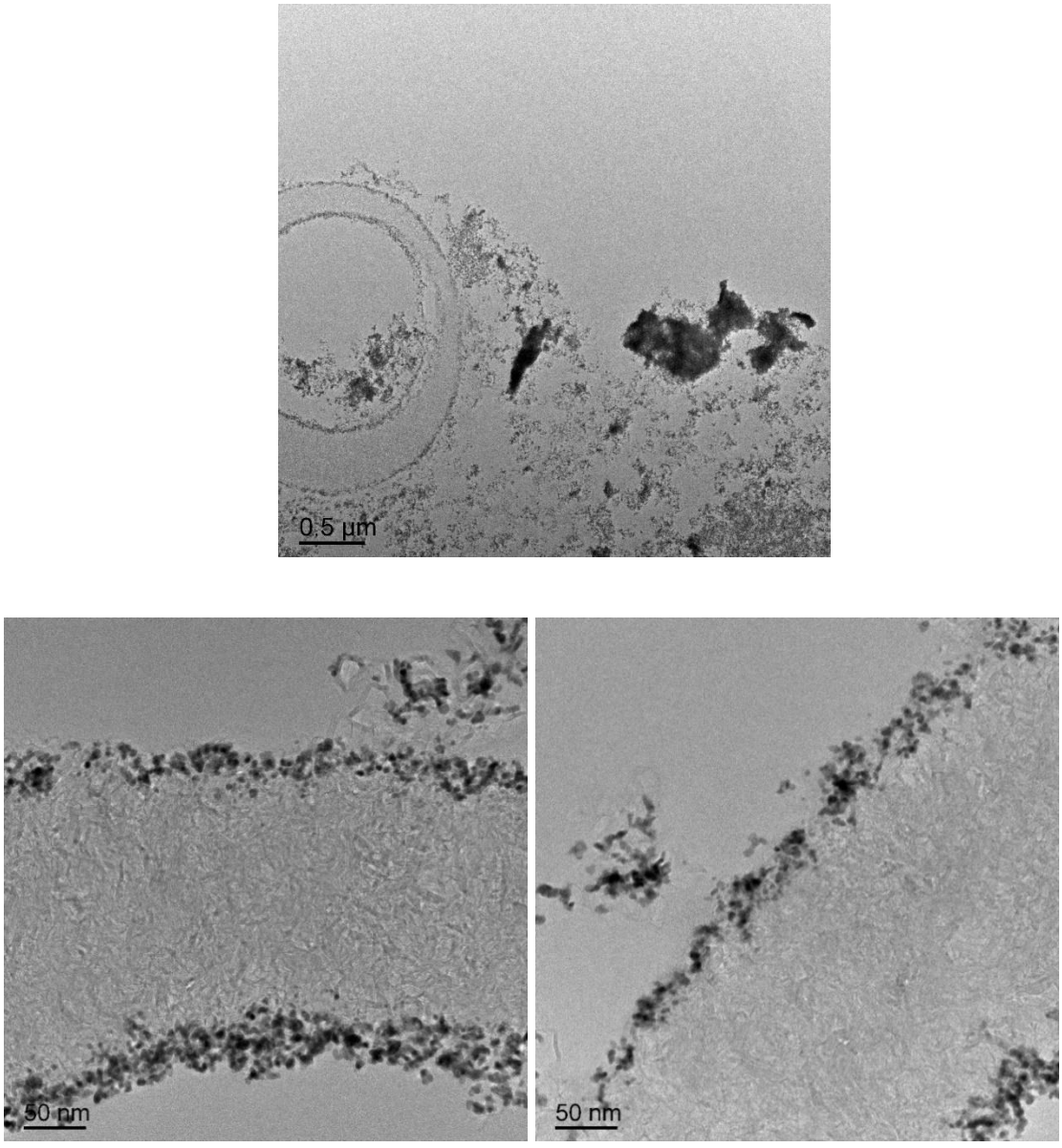

Figure 5.10 TEM images of Pt agglomeration attached to the surface of carbon clusters in 70:20 Pt:C free standing CLs.

Compared to the water uptake experiment carried out with the in-house 3M CLs, which showed, at a certain Pt:C ratio, λ increased as the ionomer content rose, the free-standing electrodes showed quite the opposite. This implies that the Pt content has an impact on the internal morphology of the 3M ionomer, an impact that is more severe than the ionomer loading. One can assume that the ionomer chains self-align differently on the Pt surface and the carbon surface. Whereas, the ionomer chains assemble into a more compact and oriented structure on the carbon surface. On the one hand, such structure obtains higher mechanical strength and less "gap" in between the ionomer chains, therefore limiting the swelling. One the other hand, more sulfonic sites could be embedded inside these film structure, weakening the water uptake. Meanwhile, the ionomer forms a looser nanostructure around the Pt surface. Therefore, providing more void spaces for the ionomer swelling and extending more active groups for water. A schematic expression is illustrated in Chapter 6.1.5, Figure 6.2.

Compared to the EW 825 3M ionomer membrane [124], the water uptake of the recast ionomer film is lower than in the bulk membrane. As discussed in the previous water uptake study with the in-house CLs, this is due to the interaction between the sulfonic acid groups and the functional groups on the surface of the carbon and Pt.

Finally, in the lower water activity region, 70:30 Pt:C CL exhibits higher water uptake than the membrane, which is due to the looser ionomer packing in the CL structure allowing more water uptake.

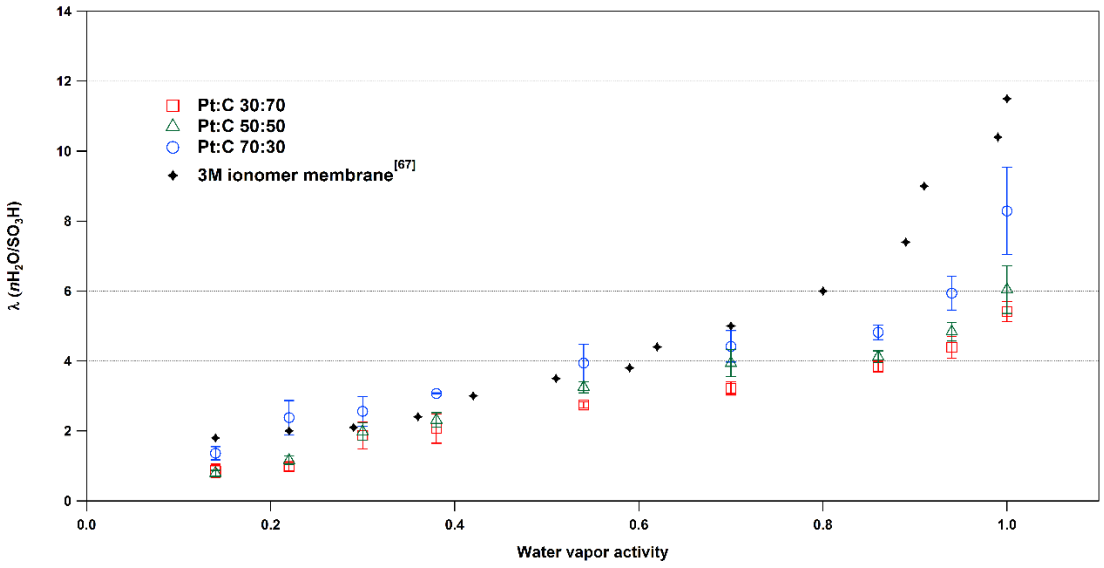

Figure 5.11 Water uptake isopiestic curve of the free-standing 3M CLs

5.5 Polarization Studies

To investigate the electrochemical performance of the free-standing 3M CLs, polarization study was carried out. The 3M CL was first cut into 5cm^2 square pieces, then hot pressed onto a 5cm^2 Sigracet 25 BC PTFE treated woven carbon paper with a microporous layer (MPL) at 140°C for 10 minutes. To fabricate the standard anode, Nafion catalyst ink was prepared (I/C=1, Pt: Vulcan carbon=30:70), then spray painted onto a 5cm^2 Sigracet 25 BC MPL carbon paper to a 0.2 mg/cm^2 Pt loading. A very thin layer of Nafion layer was then sprayed onto the anode and cathode electrodes (20μL 5*wt*% Nafion solution, Ion Power) to improve the connection between the electrodes and membrane. The pair of electrodes was hot-pressed onto a pre-treated Nafion 212 membrane. The MEA was then assembled into a single cell fuel cell hardware.

To study the polarization behavior, measurements in both H_2/O_2 and H_2/air were performed at an 80°C cell temperature, and 13psi/13psi backpressure. The inert gas flow is 100sccm/100sccm for H_2/O_2 and 100sccm/200sccm for H_2/air. Each cell system was conditioned overnight at 60% RH.

As shown in Figure 5.12 and 5.13, except for the Pt:C 50:50 cell under H_2/air operation, according to the IR corrected polarization curves, at lower overpotential (cell working potential>0.7V), the dryer the cell, the lower the current output. This occurs since, at the low humidity level, less water is adsorbed onto the hydrophilic sites in the 3M ionomer. Since the proton transport is confined to the hydrated sites, both the ionomer inside the CL and the proton exchange membrane offer lower proton conductivity at lower RH level.

However, as the overpotential increases (cell working potential<0.7V), the cells at lower RH levels (<50%) show larger current output than those operating under higher RH. This improvement of the cell performance under low RH level can be due to the reactive formation of water at higher overpotential. The effect of water production can be further confirmed by the drop of area specific resistance (ASR) along with the decrease of the working potential, which is especially pronounced amongst the lower RH level cells. As the cell voltage decreases, more water is created by the ORR in the cathode. On one hand, the additional water can humidify the drier ionomer in the lower RH cells; on the other hand, in the already humidified fuel cells, the excess water can cause blockage of the reactant gas transport, lowering the performance.

Furthermore, similar to the in-house made 3M CLs, the optimum performance of the cell occurs in the RH level range of 35%-70%. Compared to typical Nafion CLs' peak performance at 100% RH, the 3M ionomer allows the cell to operate effectively under dryer conditions. Also, the improvement of performance in the RH 35% cell indicates that the 3M CLs are fairly sensitive to the water content inside the operating system. This is further justified by the fact that the cells operating at high RH levels (>80%) suffer sudden current drop in the mass transfer region.

Comparing the polarization curves of the three different Pt:C ratio CLs, as shown in Figure 5.14, no significant difference was observed in the kinetic and ohmic loss region. If we assume that all samples obtain a well-developed proton conducting network, one should expect that the higher Pt:C ratio CL cell would have a better performance in the ohmic loss region, since the CL is thinner. However, this was not observed in this study. This implies

that the protons do not travel unimpeded through the CL. Instead, they conduct through the tortuous ionic pathway, which, most likely, is more sinuous at higher Pt:C ratio.

Furthermore, the cell reaches a rather low limiting current (~1.5A/cm^2 under H_2/O_2 and ~0.8A/cm^2 under H_2/air). This implies that the oxygen faces transport impedance at lower current density than expected. There are two proposed reasons that could lead to such issues. One is that the ionomer in the CL reaches its swelling point at a lower at a relatively low over potential, and the excessive water does not attach onto the 3M ionomer, but linger in the pores structures. Without efficient removal, the "trapped" water greatly hinders the oxygen from reaching the reaction sites, therefore causing the increasing mass loss. Another possible origin of the low limiting current is the MPL. According to previous studies, the water transport is greatly influenced by the several MPL parameters, such as its thickness, pore size, porosity distribution and hydrophility [155]. The cathode electrode was prepared by hot pressing the free-standing CL onto the MPL first, then hot-pressed onto the Nafion membrane. During the two hot-pressing processes, the MPL structure could be altered or even damaged, affecting the parameters mentioned above. Alternatively, water could be trapped at the MPL/CL interface.

5.6 Proton Conductivity

The cathode proton conductivity was measured for the free-standing 3M ionomer fuel cells. We were able to obtain results from CLs with 30:70 and 50:50 Pt:C ratio, however, the sample with 70:30 Pt:C ratio has not yielded reasonable impedance spectra data for conductivity calculation. Continued research is being done as this thesis is being produced.

Figure 5.12 Polarization Curve and area specific resistance of free standing 3M ionomer CL fuel cells at various relative humidity. Inlet gas: H_2/O_2; flow rate: 100sccm/100sccm; cell temperature: 80°C; back pressure: 13psi/13psi.

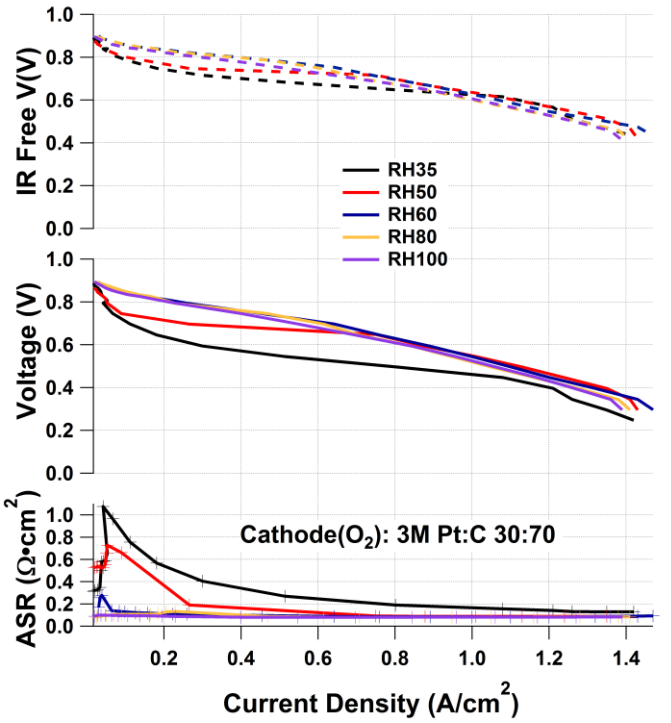

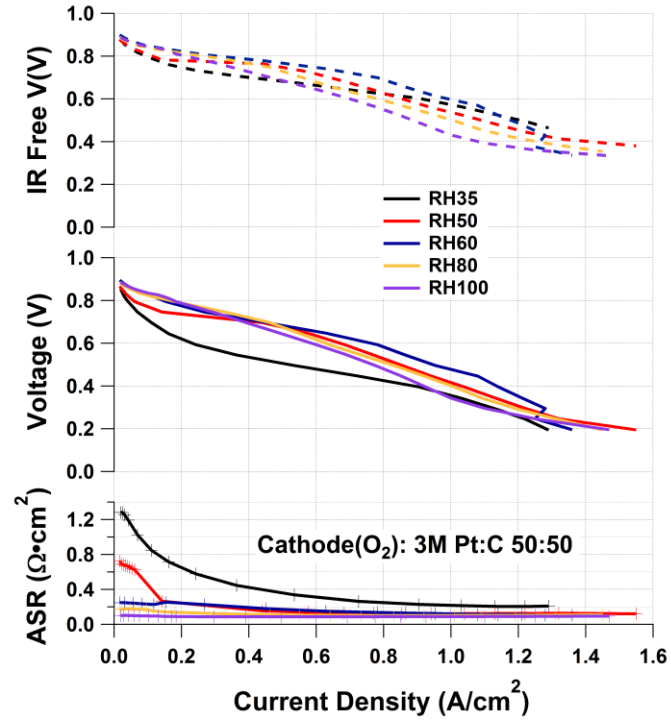

Figure 5.12 Continued.

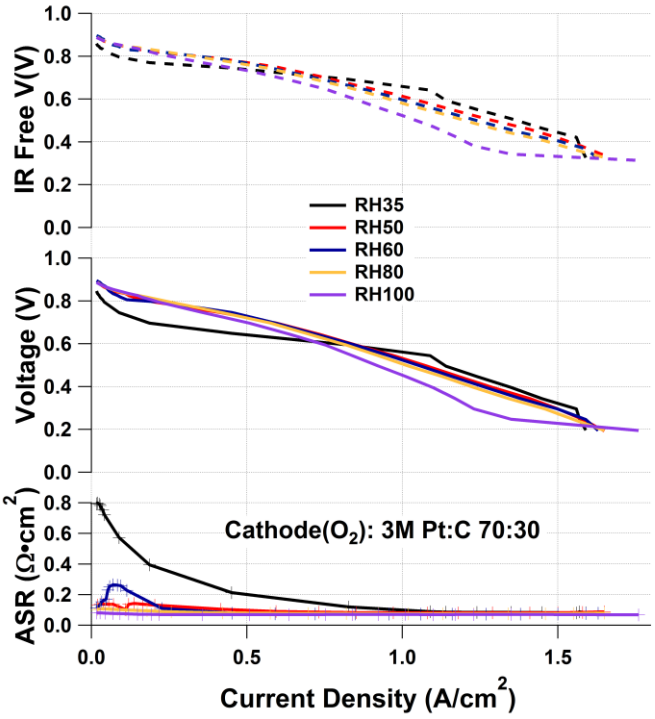

Figure 5.12 Continued.

Figure 5.13 Polarization Curve and area specific resistance of free standing 3M ionomer CL fuel cells at various relative humidity. Inlet gas: H_2/Air; flow rate: 100sccm/200sccm; cell temperature: 80°C; back pressure: 13psi/13psi.

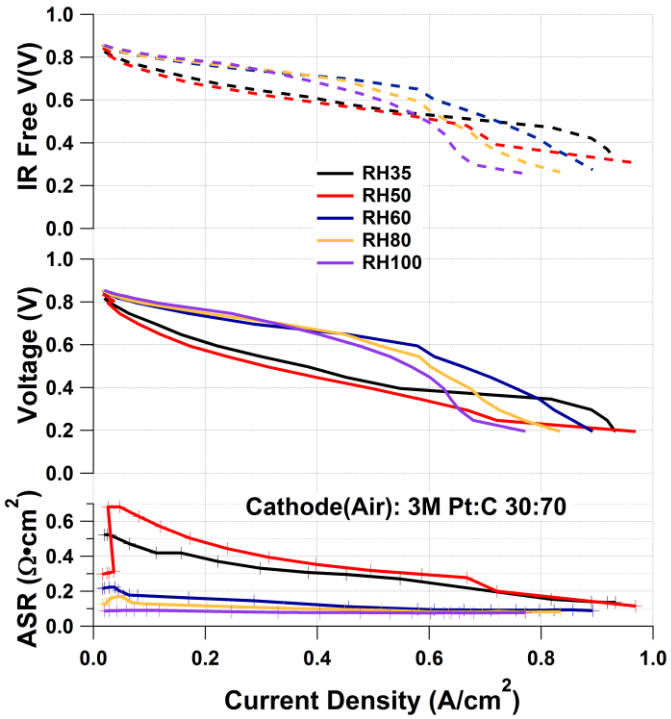

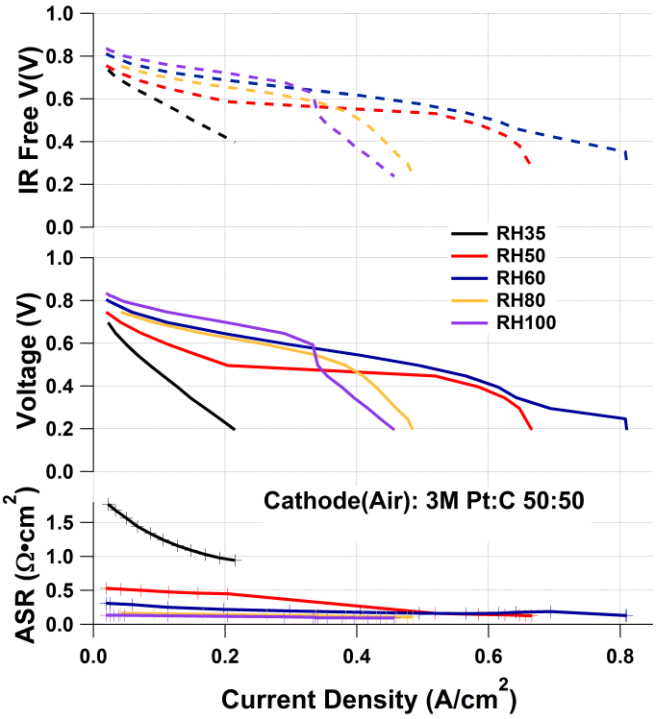

Figure 5.13 Continued

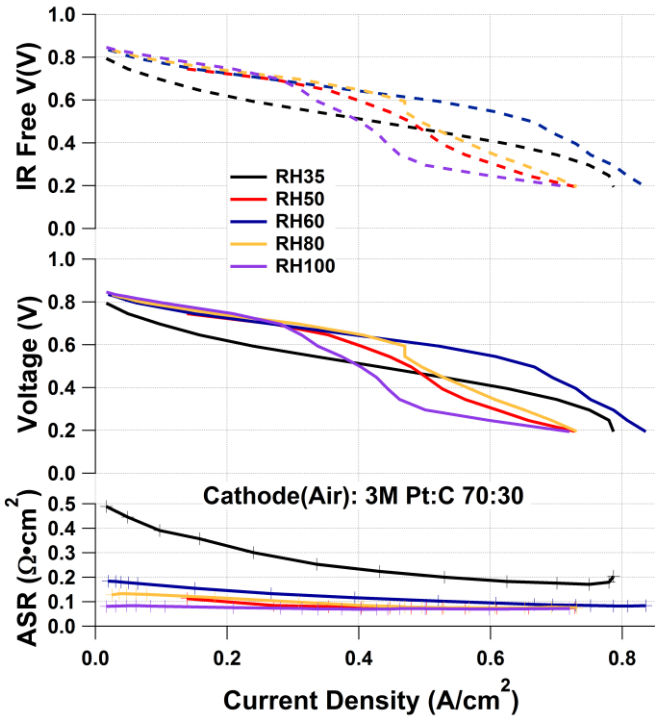

Figure 5.13 Continued.

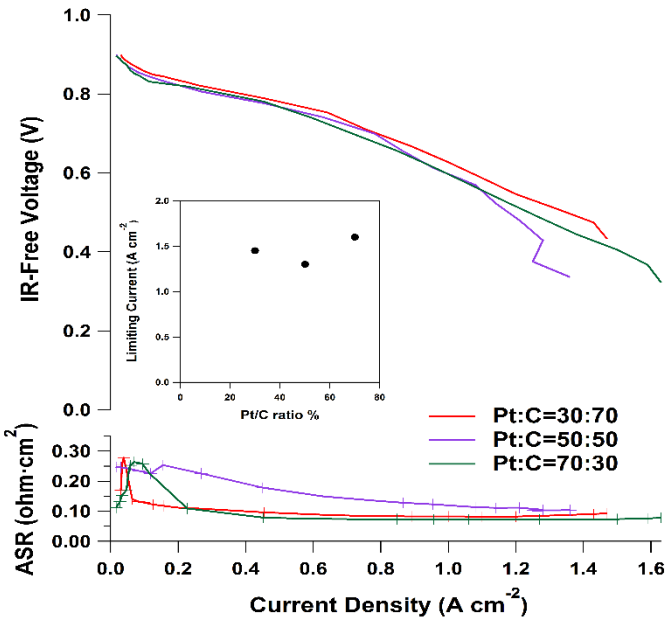

Figure 5.14 Polarization Curves of the free-standing CLs with different Pt: C ratios under H_2/O_2 operation at 60% RH, IR corrected voltage is displayed.

According to the result shown in Figure 5.15 and 5.16, compared to the 100% RH working condition, the proton conductivity suffers a tenfold loss at 35% RH. This is identical to decrease in the proton conductivity of 3M ionomer membrane. This implies that during the cell operation, as RH decreases, both the CL and membrane suffer equally for their conductivity. Furthermore, as shown in Figure 4.20 and 4.21, the membrane conductivity reaches 0.3 S/cm at saturated humidity level as the in-house made I/C=0.8 CL only reaches ~0.03 S/cm. Compared to the 30:70 free-standing CL's 0.08 S/cm, the CL is still the main contributor to the ohmic loss during fuel cell operation.

There is a difference in conductivity amongst different Pt:C ratios at a certain RH%. Under the assumption that the proton conductivity is an intrinsic property of the ionomer that should be independent to the cathode thickness, the Pt to carbon ratio probably affects the ionomer distribution and intrinsic morphology in the CL. As the Pt:C ratio increases, the Pt particles form bigger agglomerates on the carbon surface. Therefore it is assumed that the ionomer has a more difficult time to form a continuous network around the Pt particles than the carbon, which agrees with the previous EDS images (Figure 5.4).

5.7 Tortuosity

Similar to the calculation in chapter 4.5, the tortuosity of the free-standing 3M CL were determined using equation 4.18. However, the thickness of the CL, t_{cath}, is available for the experimental data acquired from the SEM image which slightly changes the volume fraction calculation following equation 5.1:

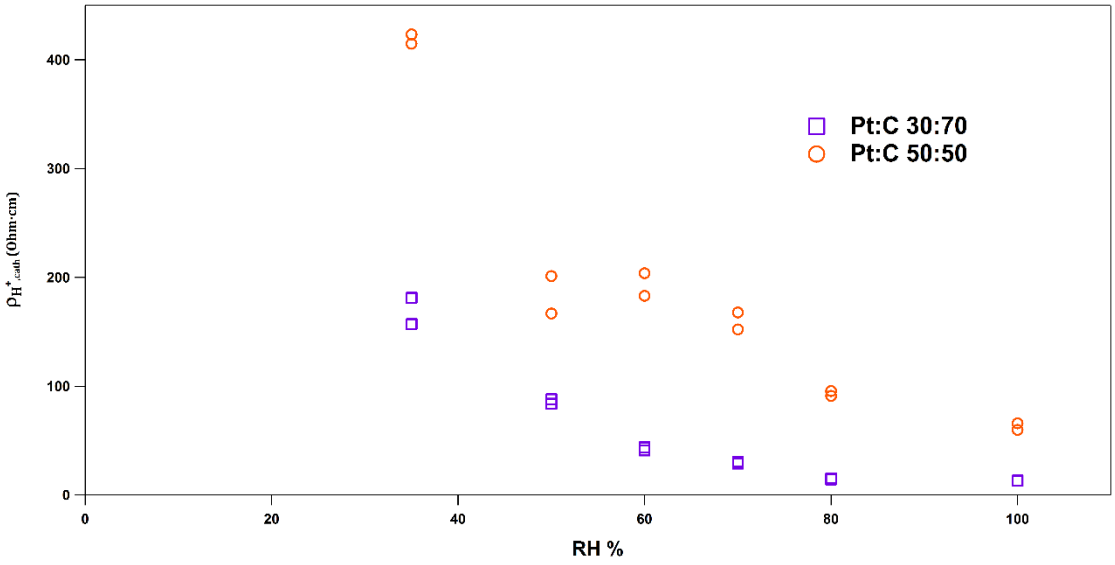

Figure 5.15 Proton resistivity of the free-standing 3M CL MEAs

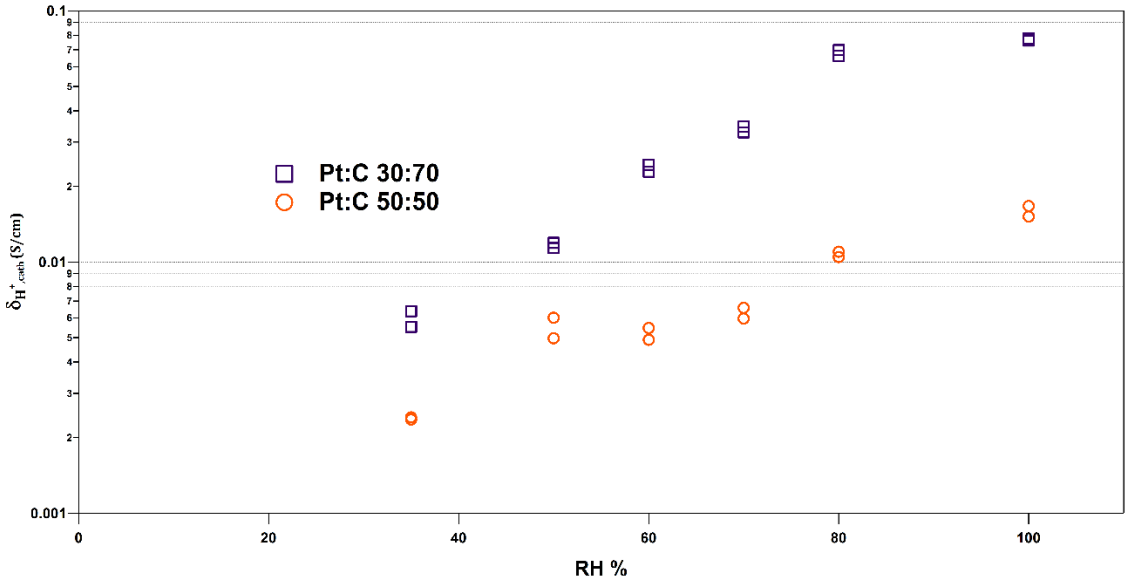

Figure 5.16 Proton conductivity of the free-standing 3M CL MEAs

$$\varepsilon_i = \left(\frac{I}{C}\right)\frac{10m_C}{t_{cath}d_{I,dry}}\left(1+\frac{M_W d_{I.dry}\lambda_{CL}}{d_W \times EW}\right) \qquad (5.1)$$

Where, m_c is the carbon loading in the CL (mg_c/cm^2); and t_{cath} is the CL thickness in unit of μm.

As shown in Figure 5.17, for both CLs with different Pt:C ratios, the tortuosity reaches unity as the cell reaches saturation. This indicates that, under significant humidification, the route of proton conducting between two points in the CL is close to a straight line, hence passing through the shortest distance. In contrast, under low RH conditions, the proton transport through a more tortuous pathway. This may happen because under dryer conditions a larger amount of the sulfonic sites in the ionomer network associated with water molecules and therefore cannot take part in the proton transport. Alternatively, the pathways for transport may be broken up as the RH decreases because the polymer shrinks and connectivity is interrupted. This is implied by the work of Sun et al. According to this, as the RH level increases the ionomer network forms a more continuous route for the proton travel.

Furthermore, both the proton conductivity and tortuosity study indicate that the proton transport faces less resistance as the RH level increases. Therefore, the decline of performance observed in the polarization study at higher RH level is not a result of the proton transfer. It is more likely due to the mass transfer resistance driven by the excessive amount of water.

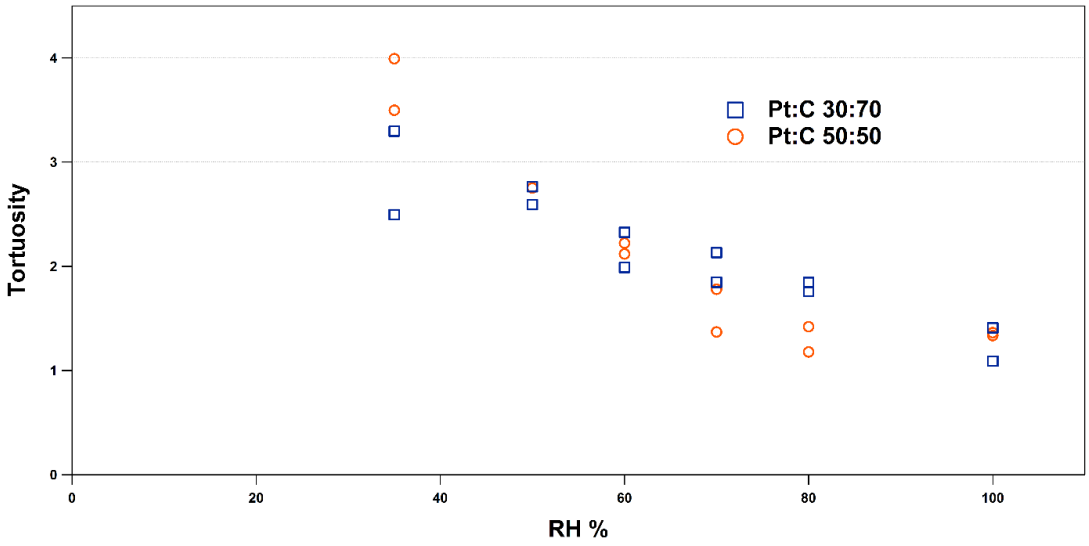

Figure 5.17 Proton Conduction Tortuosity of the free standing 3M CLs at various RH levels.

5.8 Difficulties

We faced several difficult issues during the characterization studies of the free-standing 3M CL samples. For one, several attempts were made to investigate the ionomer distribution through TEM imaging. However, as mentioned before, it is difficult to differentiate the epoxy resin from ionomer since both exhibit amorphous structures in the microscopic images. Therefore, the commonly used full-embedding method was not feasible for our purpose. The first and most straightforward solution was to use the partial embedding technique. However, as shown in Figure 5.18 b), compared to a workable section (Figure 5.18 a), this partially embedded local structure was incomplete, with the non-embedded area broken off, defeating the whole purpose. A new method similar to the partial-embedding was proposed to prepare an un-embedded sample under room-temperature. However, no CL section was detected under the TEM, as shown in Figure 5.18 c. We suspect that the fragile compound was destroyed during the microtome slicing. Furthermore, we attempted to cut the sample directly in the cryo-state. However, as shown in Figure 5.18 d, the tenuous nature of the free-standing CL leads to shattering. Tiny broken-off sections of the sample were observed spreading over the lacey carbon grid, failing to preserve the original structure.

Figure 5.18 Attempts to prepare non-fully embedded free-standing 3M CLs. a) a feasible sample section for investigation prepared by the fully embedding technique; b) partially embedded CL sample with the un-embedded area broken off; c) Samples prepared by a novel method resulting in the entire CL peeling off; d) Samples prepared under cryo-state microtome with the CL fractured and flaked off.

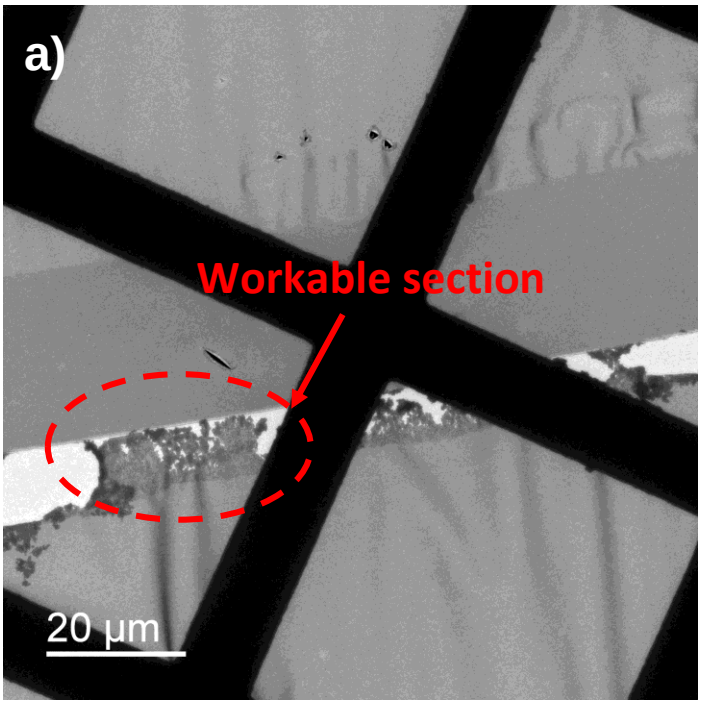

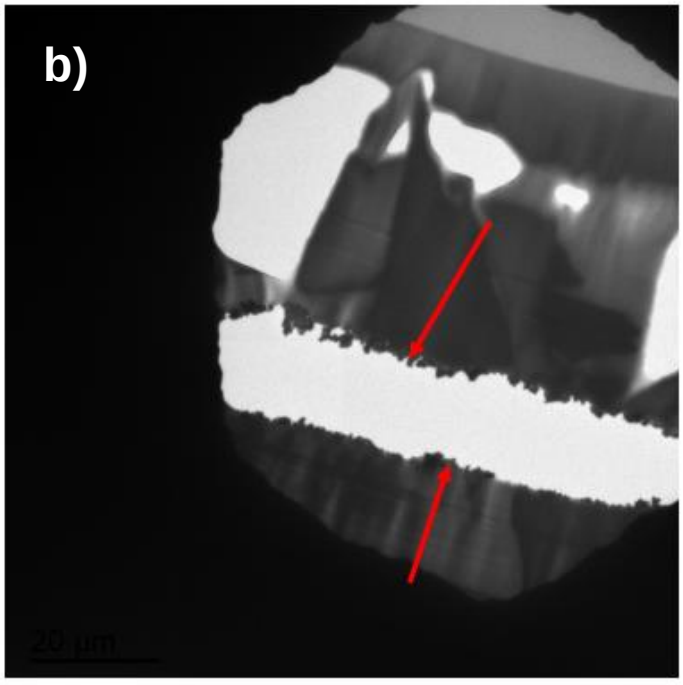

Figure 5.18 continued.

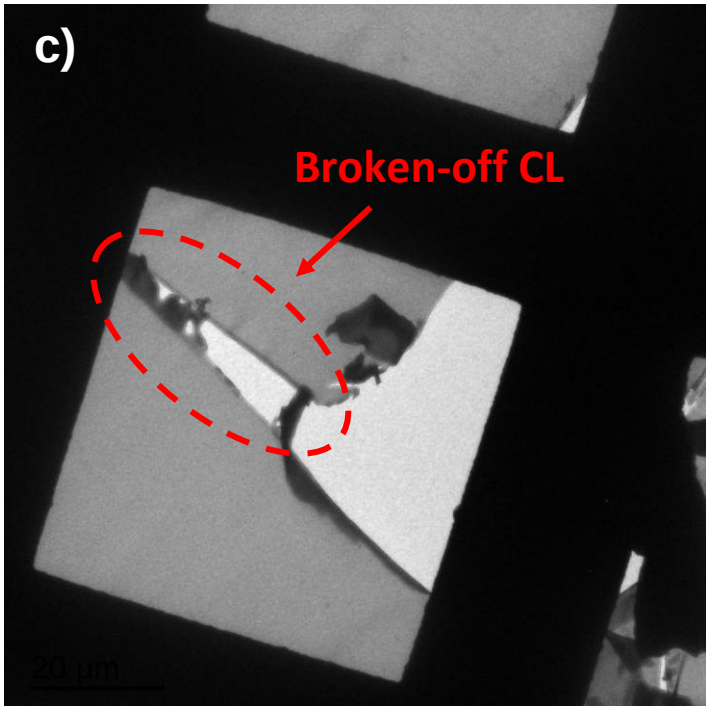

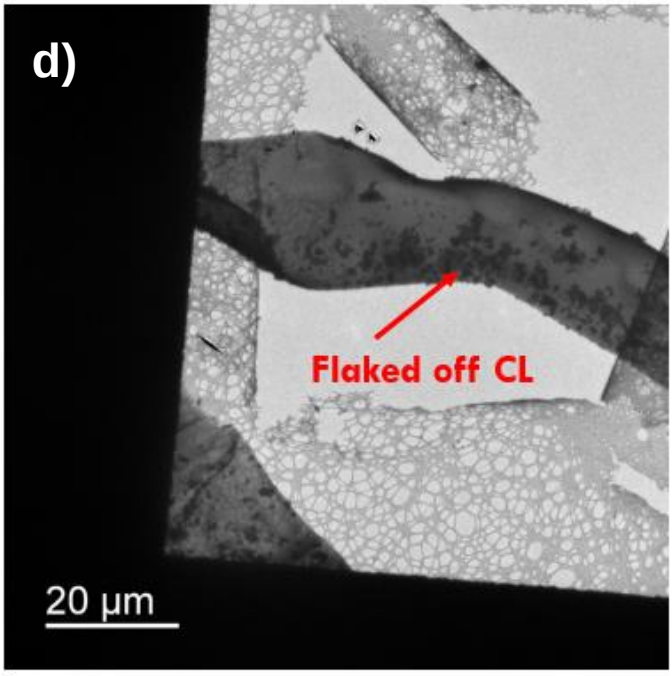

Figure 5.18 continued.

5.9 Comparison between In-house Made and Free-Standing 3M Ionomer CL

The microstructure and performance of the in-house made and 3M prepared free-standing CLs are compared in this sub-chapter. A list of measured CL samples and several properties are listed in Table 5.

First, the I/C=0.8 and 1.2 in-house made CL and the Pt:C 30:70 free-standing CL exhibit comparable BET total surface area and water uptake. This, on some level, validates the accuracy of the in-house CL preparation process. However, the 30:70 free-standing CL showed a higher proton conductivity, which could be due to the variant CL fabrication method and carbon support. However, specific information was not provided from 3M regarding to the above two subjects, therefore further discussion is restricted.

The water uptake of the in-house and free-standing CLs were measured and compared in Figure 5.19. The CLs exhibit an overall lower water uptake than the bulk membrane. This implies a variance in the nanostructure of the ionomer between thin film and membrane. One can assume that the interaction between the ionomer sulfonic groups and the Pt/C surface lessens the amount of active sites for the water molecules to attach onto. As the I/C ratio increases, the ionomer film over the Pt/C agglomerations thickens and behaves more similarly to the bulk membrane. Also, the water uptake increases along with the growth of Pt:C ratio, which suggests a larger amount of "freed-up" sulfonic sites in high Pt:C loading CLs. This implies that the ionomer active site prefers to bond with carbon over Pt.

Table 5. A list of the measured CLs in this thesis.

	I/C ratio	Pt:C ratio	Pt loading (mg/cm^2)	BET surface area (m^2/g)	Limiting current density under H_2/O_2 (A/cm^2)
In-house made CL	0.2	30:70	0.4	98.14	0.8
	0.4	30:70	0.4	—	0.9
	0.8	30:70	0.4	57.34	2.3
	1.2	30:70	0.4	—	0.6
	2	30:70	0.4	31.65	0.6
Free-standing CL	1	30:70	0.25	55.76	1.4
	1	50:50	0.25	61.14	1.6
	1	70:30	0.26	192.30	1.3

Table 5. A list of the measured CLs in this thesis continued.

	I/C ratio	Pt:C ratio	Water uptake at 100% RH	Proton conductivity at 100% RH (S/cm)
In-house made CL	0.2	30:70	3.3	0.005
	0.4	30:70	—	0.006
	0.8	30:70	4.9	0.024
	1.2	30:70	5.3	—
	2	30:70	7.2	—
Free-standing CL	1	30:70	5.4	0.078
	1	50:50	6.0	0.017
	1	70:30	8.3	—

Polarization curves are compared at 60% under H_2/O_2 at 80°C, as shown in 5.20. There are several points to be noted. First, for the in-house made CLs, the I/C 0.8 sample exhibits the best overall performance and the largest limiting current. The greater variance between the polarization curves in the in-house made samples can imply several things: On the one hand, the change in I/C ratio has a significantly greater effect on the cell performance than does the Pt/C ratio, especially for the limiting current. On the other hand, the automated fabrication technique used for the free-standing 3M samples better guarantees consistent properties of the CLs.

The proton conductivity and tortuosity study on the in-house made CL showed an improvement in conductivity as the I/C ratio and RH% increases, as shown in Figure 5.21. In association with the porosity study, this indicates that the larger amount of ionomer fills the secondary pores, constructing a more continuous ionomer network and providing a less tortuous proton conduction pathway. On the other hand, as the humidity level increases, more bulk-like water forms in the ionomer. The rise in proton conductivity implies that the existence of the bulk-like water possibly enforces the Grotthuss transport, therefore altering the proton conducting mechanism. Furthermore, from the free-standing CL study, an influence of Pt:C ratio on the proton conductivity was observed. This indicates that the Pt:C ratio also affects the intrinsic nanostructure of the ionomer film.

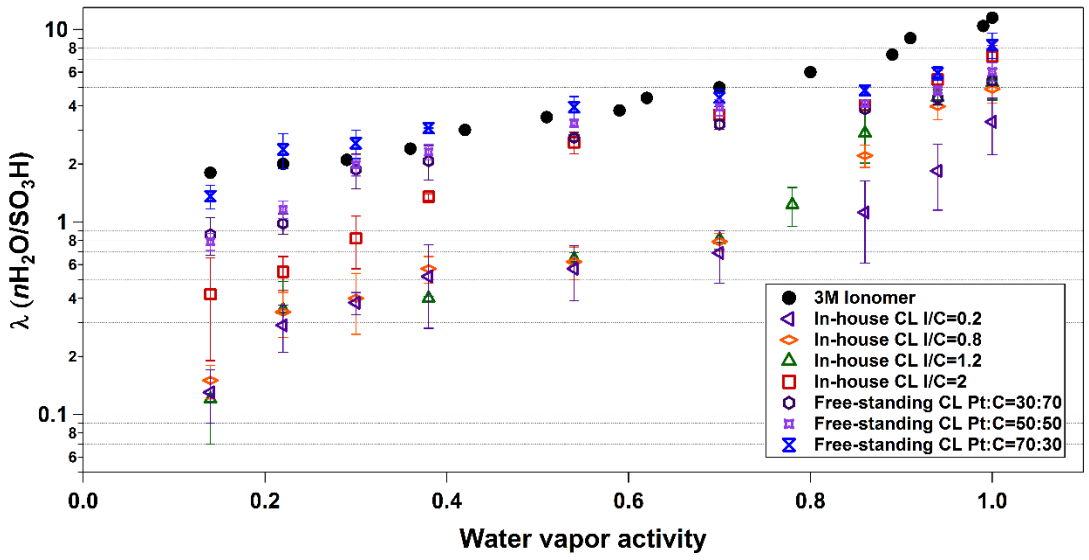

Figure 5.19 Water uptake of 3M membrane, in-house made CL and free-standing CL.

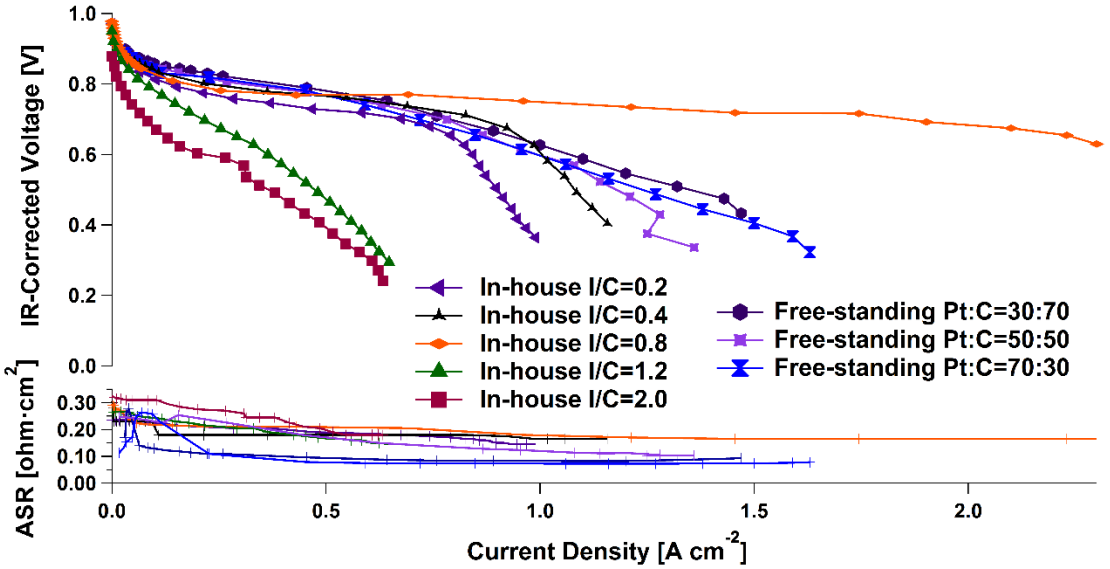

Figure 5.20 Comparison between the polarization curves of in-house and free-standing CLs. Inlet gas: H_2/O_2; cell temperature: 80°C; back pressure: 13psi/13psi; RH level: 60%.

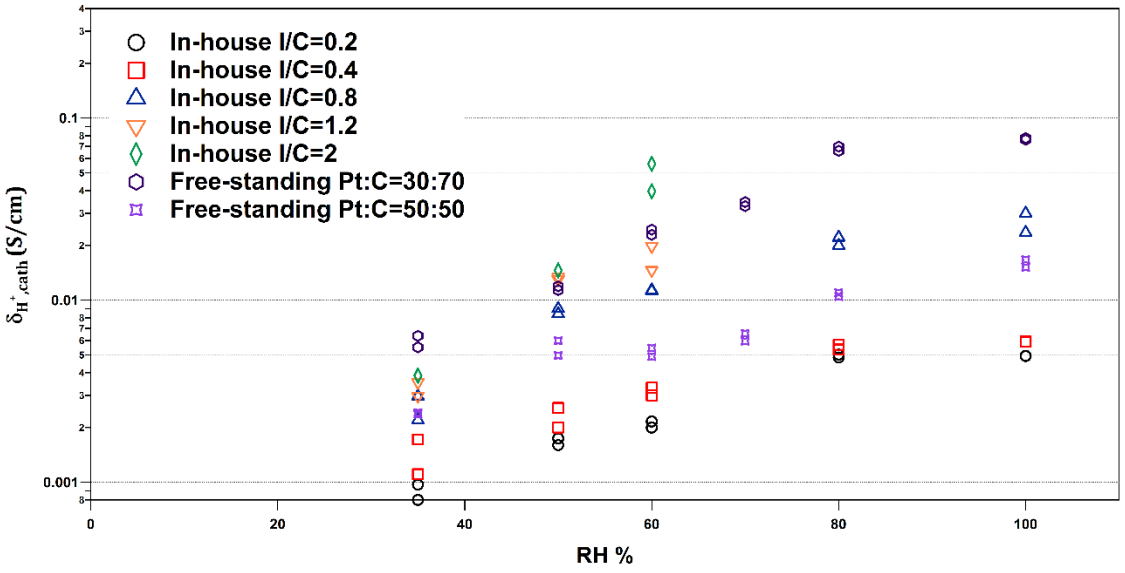

Figure 5.21 Proton conductivity of in-house made and free-standing CLs.

Chapter 6

Conclusions and Suggestions on Future Work

6.1 Conclusion

To design an optimum CL for the PEM fuel cell, the effect on oxygen mass transfer, water transport, platinum coverage and proton conductivity all have to come into account. For example, a larger amount of 3M ionomer loading can ensure a better developed proton conducting network. As a tradeoff, the ionomer reduces the specific volume of the secondary pores, hindering the oxygen mass transport, which can lead to a massive drop in cell performance at higher current density. Therefore, the CL design problem is to balance the pros and cons of each individual factor according to the application demand.

Sets of structural and electrochemical data of 3M ionomer CLs were provided and discussed in the last two chapters. Structure wise, the morphology was examined with electron microscopic techniques, the porosity was investigated with a nitrogen adsorption technique and water uptake was measured to provide more insight on the recast ionomer film in the catalyst structure. Performance wise, polarization curves and EIS data were measured, from which CL proton conductivity and the proton conducting tortuosity was calculated.

6.1.1 Microstructure

The TEM images revealed the CL microstructure as Pt on carbon agglomerations bound together with ionomer. Pt exists in both single particle and agglomeration forms and

tends to coalesce more intensely in the higher Pt:C ratio sample. Pores of different magnitudes have been observed amongst the carbon agglomerates. Along the edge of the larger pores, the ionomer covers the carbon and forms a film around the pore walls. Meanwhile it was difficult to detect the presence of ionomer in the smaller pores due to the amorphous structure of both the Vulcan-XC 72 carbon and ionomer. Furthermore, the CLs with lower I/C ratio has a less complete ionomer filling. In the higher ionomer content samples, an ionomer network can be constructed inside the larger pores.

The nitrogen adsorption technique revealed all the CL samples to be type-two adsorption and H3 type hysteresis. This indicates the CL porous structures all contain micro-, meso- and macro-pores that are different in shapes and inter-connected, which coincides with the SEM and TEM findings. A significant decrease in the amount of micro-, meso- and macropores appeared as 3M ionomer was introduced into the Pt/C powder. As the ionomer content increased, we observed volume drops in all three types of pores, which indicated that a larger ionomer content depresses the pore formation either through actual filling or forcing the Pt/C particles to be more compact. Furthermore, the amount of micro-pores increased significantly at 70:30 Pt:C ratio. This agreed with our microscopy findings, in which the large amount of Pt leads to extensive Pt agglomeration on the edge of clusters of carbon “ribbons”.

6.1.2 Water Uptake

Several studies have been published on the water uptake by thin films of ionomers with contrasting findings. Kongkanand [131] reported the thinner ionomer film (33nm) had a

slightly smaller water uptake than the thicker film (500nm), whereas Dishari [86] reported that thinner ionomer film took up more water and displayed less 'antiplasticization' than the thicker membranes. Kusoglu et al. [38] studied the water uptake by the CL from both vapor and liquid phases. From water vapor e, the uptake of water by the CL was significantly lower than that of the bulk membrane (~λ=4 versus 10 at 95% RH). A similar finding was also reported by Iden *et al.* [128]. Our study showed a lower water uptake in the CL than in the bulk membrane. We proposed that the surface influence of the Pt/C agglomerates on the ionomer distribution is the main cause of the decrease in water uptake. As the ionomer content increases in the in-house made CLs, the water uptake value increases, suggesting that the ionomer further away from the carbon surface is less influenced by the surface influence and possesses similar intrinsic nanostructure as the bulk membrane. Meanwhile, from the free-standing 3M CLs, the Pt:C ratio surprisingly has a stronger effect on the CL water uptake than does the ionomer content. This suggests that the ionomer forms a looser structure around the Pt particles.

6.1.3 Electrochemical Performance

To investigate the performance of 3M CLs, polarization experiments were executed along with the estimation of the CL proton conductivity and proton conducting tortuosity. To summarize our findings:

1. PEMFCs containing 3M ionomer CLs reach peak performance around 60% RH. In contrast to the traditional Nafion fuel cells, as the 3M cells reach a saturated humidity level, they show a dramatic mass transfer losses. This loss was observed

in cells using both PTFE treated carbon paper and a microporous layer as GDLs which indicates that the 3M CL is quite sensitive to extensive water content. On the one hand, this can be due to the low water uptake of CLs, resulting in a larger amount of water being trapped in the CL instead of being attached onto the ionomer. On the other hand, this can imply slower water transport in the 3M CLs.

2. According to the polarization performance study, the optimum I/C ratio for 30:70 Pt:C 3M CLs is 0.8. Even though larger ionomer loading increases the proton conductivity and constructs a less tortuous proton transporting pathway, the extensive filling of the secondary pores strongly hinders the oxygen and water transport.

3. The CL proton conductivity was calculated and shown to be 10 fold lower than that of the bulk membrane, causing it to be the main contributor to ohmic loss during fuel cell operation, also suggesting a difference in intrinsic structure and proton conducting mechanism between the thin ionomer film and bulk membrane.

4. The proton conduction tortuosity further justifies the microscopic findings, where a higher I/C ratio leads to a better developed and less sinuous proton pathway.

6.1.4 Thermal Studies

According to the thermogravimetric behavior, the decomposition of the CL shifted to a lower temperature than for the 3M ionomer with the presence of catalytic particles. During the DSC study, the CL prepared from alcoholic based ink exhibited a distinct exothermal behavior in the range of 100°C -140°C. This was determined to be caused by

an interaction between the Pt particles and the alcoholic solution, i.e. the alcohol adsorbed onto the Pt surface during ink preparation, which leads to CO_2 formation at elevated temperature.

6.1.5 A Proposed CL Formation Process

According to our above studies, a formation process is proposed according to our findings, illustrated in Figure 6.1 and 6.2. In the ink solution where the IPA wt% is higher than 70%, the 3M ionomer particles are well dispersed and exist in a rod-like structure [61], as shown on the upper left in Figure 6.1. As Pt/C particles are introduced into the solution, a bonding process begins. For the early adsorption layers, the ionomer polymer molecules attach onto the carbon through the interaction between sulfonic acid group and functional groups, probably undergoing a hydrogen reaction. The ionomer covers around the Pt particles, not building a strong bond like it does with the carbon support, leaving a gap in between the ionomer and Pt. Therefore, as the Pt:C ratio increases, a more porous structure is constructed. At high Pt:C ratio (70:30), the ionomer structure can become discontinuous, severely lowering the CL proton conductivity. It has been proposed that the dominant proton conduction mechanism amongst these thin films is the surface diffusion (vehicle) mechanism [110]. As more ionomer adsorbs onto the Pt/C agglomerates, the ionomer film over the carbon becomes thicker and exhibits properties more similar to the bulk-like membrane. More sulfonic groups that are not interacting with the carbon provides more active sites for water uptake and proton conduction. Also, at high RH level, a larger amount of sulfonic acid groups can interact with bulk-form water, fortifying the Grotthuss conducting mechanism.

In this model, it was assumed that during the CL formation, the sulfonic groups tend to attach to the carbon surface rather than the Pt. This assumption was supported by several findings in this study:

1. The EDS image (Figure 5.4) showed a more intense distribution of ionomer along the carbon edge of the larger pores.

2. A build-up in BET total surface area, amount of micro- and meso-pores (2nm-50nm) as the Pt:C ratio increases. This can be due to the gap between the ionomer film and Pt particles.

3. The higher water uptake at elevated Pt:C ratio suggests the introduction of more Pt results in larger amounts of "freed-up" ionomer sites, implying a weak bonding between the active sites and Pt surface.

4. The increase in proton conductivity from 30:70 Pt:C CL to 50:50 Pt:C CL implies the ionomer is frustrated in constructing a continuous structure over the larger Pt agglomerates. However, this argument should be further examined by obtaining the performance data of 70:30 Pt:C CLs.

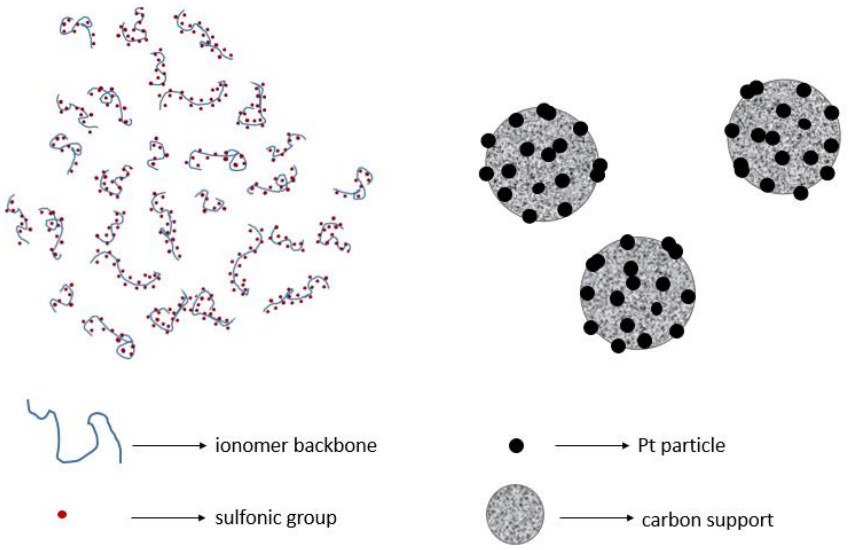

Figure 6.1 Illustration of 3M ionomer and Pt on carbon support.

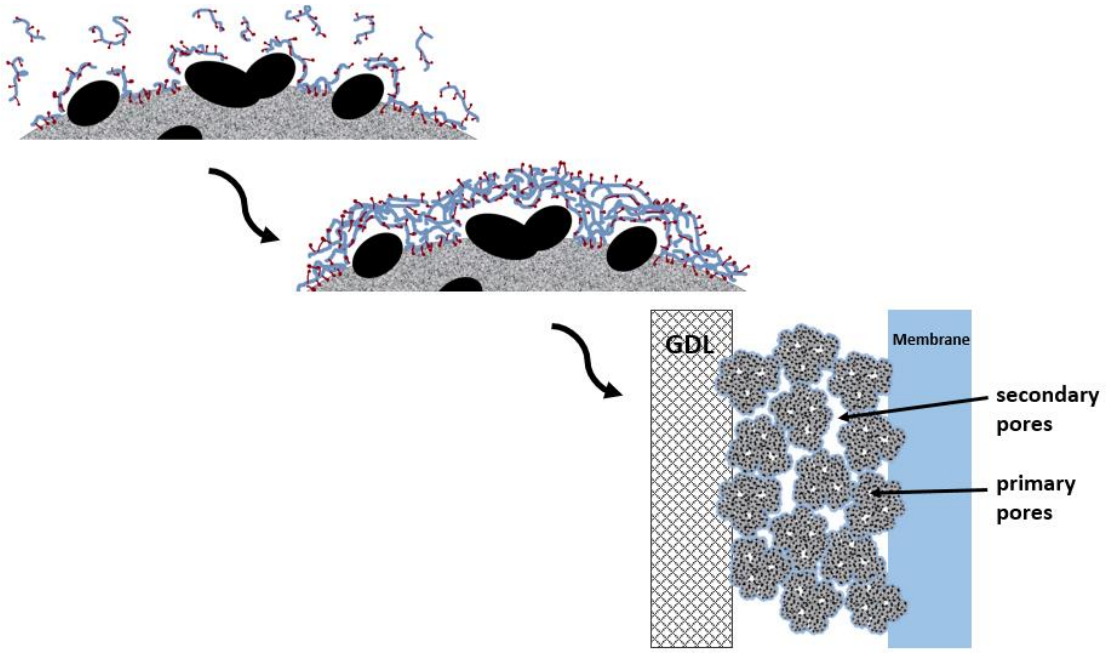

Figure 6.2 Illustration of the 3M ionomer adsorbing onto the Pt/C surface.

6.2 Recommendation for Future Work

Here are several suggestions on future work to further investigate the properties of PEM CLs.

6.2.1 Microstructure

TEM graphic analysis was executed to study the morphology of the CLs. Along with the utilization of ImageJ software, we were able to quantify the Pt particle and agglomerate sizes. However, as mentioned in sub-chapter 5.9, we faced the challenge of preparing non-embedded free-standing CL samples. Further effort is required to construct a feasible TEM sample preparation protocol. Also, the EDS allows us to directly visualize the distribution of individual components in the CL. However, obtaining high quality EDS images under STEM can be difficult, possibly caused by resolution issues. Electron Energy Loss Spectroscopy (EELS) could be complementary to the structural characterization at a higher resolution. Furthermore, the morphology studies in this thesis focused on the pre-used CLs. Studies on post-mortem samples could provide insights on the durability and decomposition of the electrode. Also, for the free-standing CL samples, it would be worthy to examine the raw Pt/C and EA carbon in order to investigate the formation of the intense Pt agglomeration observed at 70:30 Pt:C ratio.

Nitrogen adsorption was carried out to investigate the total surface area and pore size distribution. This technique represents the micro-, meso- and macro- pores in the sample. However, larger pores were observed in the macroscopic images which were failed to being

assessed in the porosity study. The mercury porosimetry technique would be a well-qualified supplement for such matters, since it detects pores from 3nm to 14μm [61].

6.2.2 Electrochemical Studies

Different models and graphical approaches have been discussed in chapter 3. Results showed that the line model with CPE provided better fit for the Nyquist plot. However, the accuracy of converting the real impedance to CL resistance needs to be further examined. Modeling work can evaluate this by comparing the graphically fitted results and the actual assigned resistance value.

During the polarization study, a severe mass transfer loss was observed in the 3M CL samples. This implies that water management is an important issue for 3M CL fuel cell units. The water transport in such CLs should be investigated, i.e. the nature of the water transport between the recast thin film ionomer inside the CL and the tortuosity of the diffusion pathway. Moreover, our water-uptake and proton conductivity study suggests a different conducting mechanism between the thin film ionomer and bulk membrane. Further research should be carried out on the intrinsic nanostructure of the thin ionomer film and what effects the formation of certain nanostructures. Moreover, more insight on the three-phase structure development can be provided through the measurement of electrochemical surface area (ECSA). For instance, we expect little increase in ECSA from the 70:30 Pt:C free-standing CL compared to the 30:70 CL despite the larger amount of Pt, since the Pt aggregation disrupts the ionomer coverage.

6.2.3 Thermal Studies

The DSC study implied that the molecules from the commonly used solvents can adsorb onto the Pt surface during ink preparation. The nature of such interactions (whether it is physisorption or chemisorption) should be studied. Fourier transform infrared spectroscopy (FTIR) can be a useful instrument for such investigation. Furthermore, the effect of such adsorption on the Pt catalytic activity should be explored. For example, the ECSA of CL prepared from alcohol based solution and water based solution can be compared as can the kinetic parameters.

References

[1] Grove, W. R. The Correlation of Physical Forces; Longman, Green, Longman,Roberts & Green, London, 1862.

[2] Hydrogen Fuel Cell – M. Suma & D. Ganga Bhavani. At http://www.yuvaengineers.com/hydrogen-fuel-cell-%E2%80%93-m-suma-d-ganga-bhavani/

[3] DOE Types of Fuel Cells. At http://www1.eere.energy.gov/hydrogenandfuelcells/fuelcells/fc_types.html

[4] Merle, G., Wessling, M., & Nijmeijer, K. (2011). Anion exchange membranes for alkaline fuel cells: A review. *Journal of Membrane Science*, *377*(1-2), 1–35.

[5] Mclean, G. F., Niet, T., & Djilali, N. (2002). An assessment of alkaline fuel cell technology, *27*, 507–526.

[6] Ryan O'Hayre, Sun-Won Cha, Whitney Colella, Fritz B. Prinz. (2006). Fuel Cell Fundamentals, p.262.

[7] Appleby, A.J., Ed. *Fuel Cells: Trends in Research and Applications;* Hempisphere Publishing Corp.: New York, 1987.

[8] Appleby, A.J.; Fouelkes, R.L., Fuel Cell Handbook, Van Nostrand Reinhold, New York, 1989.

[9] Chen E.; In *Fuel Cell Technology Handbook,* Hoogers, G, Ed. CRC Press: New York, 2003.

[10] Horschehofer, J.H.; Stauffer, D.B.; Engleman, R.R., *Fuel Cells: A Handbook for the Department of Energ;* B/T Books: Orinda, CA, 1996; p1-1.

[11] Peighambardoust, S. J., Rowshanzamir, S., & Amjadi, M. (2010). *Review of the proton exchange membranes for fuel cell applications*. *International Journal of Hydrogen Energy* (Vol. 35, pp. 9349–9384). Elsevier Ltd.

[12] Rajalakshmi N, Dhathathreyan KS. Catalyst layer in PEMFC electrodes: fabrication, characterization and analysis. Chem Eng J 2007;129:31–40.

[13] Hickner, M. a, Ghassemi, H., Kim, Y. S., Einsla, B. R., & McGrath, J. E. (2004). Alternative polymer systems for proton exchange membranes (PEMs). *Chemical Reviews*, *104*(10), 4587–611.

[14] Costamagna P, Srinivasan S. Quantum jumps in the PEMFC science and technology from the 1960 to the year 2000 part I. Fundamental scientific aspects. J Power Sourc 2001, 102: 242-52.

[15] Rikukawa M, Sanui K. Proton-conducting polymer electrolyte membranes based on hydrocarbon polymers. Prog Polym Sci 2000;25:1463-502.

[16] Gebel, G. Polymer 2000, 41 (15), 5829−5838.

[17] Page, K. A.; Cable, K. M.; Moore, R. B. Macromolecules 2005, 38 (15), 6472−6484.

[18] Page, K. A.; Landis, F. A.; Phillips, A. K.; Moore, R. B. Macromolecules 2006, 39 (11), 3939−3946.

[19] Soc, J. E., The, A., Society, E., Springer, T. E., Zawodzinski, T. A., & Gottesfeld, S. (1991). Polymer Electrolyte Fuel Cell Model, 138(8), 2334–2342.

[20] Litster, S., & McLean, G. (2004). PEM fuel cell electrodes. Journal of Power Sources, 130(1-2), 61–76.

[21] R. P. Iczkiwski and M. B. Cutlip, J. Electrochem. Soc., 127, 1433 (1980).

[22] R. O'Hayre and F. B. Prinz, J. Electrochem. Soc., 151, A756 (2004).

[23] J. Fleig, J. Power Sources, 125, 228 (2002).

[24] O'Hayre, R., Barnett, D. M., & Prinz, F. B. (2005). The Triple Phase Boundary. Journal of The Electrochemical Society, 152(2), A439.

[25] Zhang, J. (2008). PEM Fuel Cell Electrocatalysts and Catalyst Layers: Fundementals and Applications.

[26] Haug, A. T., White, R. E., Weidner, J. W., Huang, W., Shi, S., Stoner, T., & Rana, N. (2002). Increasing Proton Exchange Membrane Fuel Cell Catalyst Effectiveness through Sputter Deposition. Journal of The Electrochemical Society, 149(3), A280.

[27] Schultz T, Sundmacher K. Mass, charge and energy transport phenomena in a polymer electrolyte membrane (PEM) used in a direct methanol fuel cell (DMFC): modelling and experimental validation of fluxes. J Membrane Sci 2006;276:272–85.

[28] Cha SY, Lee WM. Performance of proton exchange membrane fuel cell electrodes prepared by direct decomposition of ultrathin platinum on the membrane surface. J Electrochem Soc 1999;146:4055–60.

[29] O'Hayre R, Lee SJ, Cha SW, Prinz FB. A sharp peak in the performance of sputtered platinum fuel cells at ultra-low platinum loading. J Power Sources 2002;109:483–93.

[30] Wee, J.-H., Lee, K.-Y., & Kim, S. H. (2007). Fabrication methods for low-Pt-loading electrocatalysts in proton exchange membrane fuel cell systems. Journal of Power Sources, 165(2), 667–677.

[31] Uchida, M., Fukuoka, Y., Sugawara, Y., Eda, N., & Ohta, A. (1996). Effects of Microstructure of Carbon Support in the Catalyst Layer on the Performance of Polymer-Electrolyte Fuel Cells. Journal of The Electrochemical Society, 143(7), 2245.

[32] Wei, Z. D., Ran, H. B., Liu, X. A., Liu, Y., Sun, C. X., Chan, S. H., & Shen, P. K. (2006). Numerical analysis of Pt utilization in PEMFC catalyst layer using random cluster model. Electrochimica Acta, 51(15), 3091–3096.

[33] Zoheir N. Farhat, Modeling of catalyst layer microstructural refinement and catalyst utilization in a PEM fuel cell, Journal of Power Sources, Volume 138, Issues 1–2, 15 November 2004, Pages 68-78, ISSN 0378-7753.

[34] M. S. Wilson, S. G. (1992). Thin-film catalyst layers for polymer electrolyte fuel cell electrodes, 22, 1–7.

[35] Guido Bender, Thomas A Zawodzinski, and Andrew P Saab, "Fabrication of high precision PEFC membrane electrode assemblies," Journal of Power Sources, no. 124, pp. 114-117, 2003.

[36] In-Su Park, Wen Li, Arumugam Manthiram, Fabrication of catalyst-coated membrane-electrode assemblies by doctor blade method and their performance in fuel cells, Journal of Power Sources, Volume 195, Issue 20, 15 October 2010, Pages 7078-7082, ISSN 0378-7753.

[37] HME Dreyer. (2011). A comparison of catalyst application techniques for membrane electrode assemblies in SO2 depolarized electrolysers. Masters in Engineering North West University Potchefstroom Campus, Mechanical Engineering.

[38] Xu Z, Qi Z, Kaufman A. Superior catalysts for proton exchange membrane fuel cells sulfonation of carbon-supported catalysts using sulfate salts. Electrochem. Solid-State Lett 2005;8:A313–5.

[39] Morikawa H, Tsuihiji N, Mitsui T, Kanamura K. Preparation of membrane electrode assembly for fuel cell by using electrophoretic deposition process. J Electrochem Soc 2004;151:A1733–7.

[40] Fernández R, Ferreira-Aparicio P, Daza L. PEMFC electrode preparation: influence of the solvent composition and evaporation rate on the catalytic layer microstructure. J Power Sources 2005;151:18–24.

[41] Passalacqua, E., Lufrano, F., Squadrito, G., Patti, a, & Giorgi, L. (2001). Nafion content in the catalyst layer of polymer electrolyte fuel cells: effects on structure and performance. Electrochimica Acta, 46(6), 799–805.

[42] Xie, J., Xu, F., Wood III, D. L., More, K. L., Zawodzinski, T. a., & Smith, W. H. (2010). Influence of ionomer content on the structure and performance of PEFC membrane electrode assemblies. Electrochimica Acta, 55(24), 7404–7412.

[43] Stevens A, Dahn JR. Thermal degradation of the support in carbon-supported platinum electrocatalysts for PEM fuel cells. Carbon 2005;43:179–88.

[44] Baturina, O. a., Aubuchon, S. R., & Wynne, K. J. (2006). Thermal Stability in Air of Pt/C Catalysts and PEM Fuel Cell Catalyst Layers. Chemistry of Materials, 18(6), 1498–1504.

[45] Samms, S. R., Wasmus, S., & Savineil, R. F. (1996). Thermal Stability of Nafion ® in Simulated Fuel Cell Environments, 143(5), 1498–1504.

[46] Matter PH, Zhang L, Ozkan US. The role of nanostructure in nitrogen-containing carbon catalysts for the oxygen reduction reaction. J Catal 2006;239:83–96.

[47] Tang H, Qi ZG, Ramani M, Elter JF. PEM fuel cell cathode carbon corrosion due to the formation of air/fuel boundary at the anode. J Power Sources 2006;158:1306–12.

[48] Stevens A, Dahn JR. Thermal degradation of the support in carbon-supported platinum electrocatalysts for PEM fuel cells. Carbon 2005;43:179–88.

[49] Auer, E., Freund, A., Pietsch, J., Tacke, T. Carbons as supports for industrial precious metal catalysts (1998) Applied Catalysis A: General, 173 (2), pp. 259-271.

[50] Ermete Antolini, Carbon supports for low-temperature fuel cell catalysts, Applied Catalysis B: Environmental, Volume 88, Issues 1–2, 29 April 2009, Pages 1-24, ISSN 0926-3373

[51] McBreen, J., Olender, H., Srinivasan, S., Kordesch, K.V. Carbon supports for phosphoric acid fuel cell electrocatalysts: alternative materials and methods of evaluation (1981) Journal of Applied Electrochemistry, 11 (6), pp. 787-796.

[52] Rao, V., Simonov, P.A., Savinova, E.R., Plaksin, G.V., Cherepanova, S.V., Kryukova, G.N., Stimming, U. The influence of carbon support porosity on the activity of PtRu/Sibunit anode catalysts for methanol oxidation (2005) Journal of Power Sources, 145 (2), pp. 178-187.

[53] F. Rodríguez-Reinoso, I. Rodríguez-Ramos, C. Moreno-Castilla, A. Guerrero-Ruiz, J.D. López-González, Platinum catalysts supported on activated carbons: I. Preparation and characterization, Journal of Catalysis, Volume 99, Issue 1, May 1986, Pages 171-183.

[54] Radovic. L. R. and Rodriauez-Reinoso, F., Chemistrv and Physics of Carbon, Vol. 25, ed. P. A. Thrower. Marcel Dekker, New York, 1997; p. 243.

[55] Derbyshire, F., de Beer, V. H. J., Abotsi, G. M. K., Scaroni, A. W., Solar, J. M. and Skrovanek, D. J., Appl. Catal., 1986, 27, 117.

[56] Prado-Burguete, C., Linares-Solano, A., Rodriguez-Reinoso, F. and Salinas-Martibez de Lecea, C., J. Catal., 1989, 115, 98.

[57] Prado-Burguete, C., Linares-Solano, A., Rodriguez-Reinoso, F. and Salinas-Martinez de Lecea, C., J. Catal., 1991, 128, 397.

[58] Francisco Rodríguez-reinoso, The role of carbon materials in heterogeneous catalysis, Carbon, Volume 36, Issue 3, 1998, Pages 159-175.

[59] L. Rubatat, A. L. Rollet, G. Gebel, and O. Diat, Macromolecules 35, 4050.

[60] L. Rubatat, G. Gebel and O. Diat, Macromolecules 37, 7772, (2004).

[61] Ngo, T. T., Yu, T. L., & Lin, H.-L. (2013). Influence of the composition of isopropyl alcohol/water mixture solvents in catalyst ink solutions on proton exchange membrane fuel cell performance. Journal of Power Sources, 225, 293–303.

[62] S. Nomula, and S. L. Cooper, Macromolecules, 34, 925 (2001).

[63] C.-H. Ma, T. L. Yu, H.-L. Lin, Y.-T. Huang, Y.-L. Chen, and U.-S. Jeng, Polymer , 50, 1764 (2009).

[64] S. H. Chan and W. A. Tun, Catalyst Layer Models for Proton Exchange Membrane Fuel Cells, Chemical Engineering Technology, 24, 51 (2001).

[65] Wonseok Yoon and Adam Z. Weber, Modeling Low-Platinum-Loading Effects in Fuel Cell Catalyst Layers, Journal of The Electrochemical Society, 158, B1007 (2011).

[66] M. Eikerling, A.A. Kornyshev, Modelling the performance of the cathode catalyst layer of polymer electrolyte fuel cells, Journal of Electroanalytical Chemistry, Volume 453, Issues 1–2, 14 August 1998, Pages 89-106.

[67] M. Eikerling, Water Management in Cathode Catalyst Layers of PEM Fuel Cells-A Structure-Based Model, Journal of The Electrochemical Society, 153, E58 (2006).

[68] Datong Song, Qianpu Wang, Zhongsheng Liua, Titichai Navessin, and Steven Holdcroft, Numerical study of PEM fuel cell cathode with non-uniform catalyst layer, Electrochimica Acta, 50, 731 (2004).

[69] . J. Marquis and M. O. Coppens, Achieving Ultra-high Platinum Utilization via Optimization of PEM Fuel Cell Cathode Catalyst layer Microstructure, Chemical Engineering Science, 102, 151 (2013).

[70] P. Jain, L. T. Biegler, and M. S. Jhon, Optimization of Polymer Electrolyte Fuel Cell Cathodes, Electrochemical and Solid-State Letters, 11, B193 (2008).

[71] Hao, L., Moriyama, K., Gu, W., & Wang, C.-Y. (2015). Modeling and Experimental Validation of Pt Loading and Electrode Composition Effects in PEM Fuel Cells. Journal of the Electrochemical Society, 162(8), F854–F867.

[72] Thomas A. Greszler, David Caulk, and Puneet Sinha, The Impact of Platinum Loading on Oxygen Transport Resistance, Journal of The Electrochemical Society, 159, F831 (2012).

[73] William K. Epting, Shawn Litster, Effects of an agglomerate size distribution on the PEFC agglomerate model, International Journal of Hydrogen Energy, Volume 37, Issue 10, May 2012, Pages 8505-8511.

[74] Ikeda, M.; Uematsu, N.; Saitou, H.; Hoshi, N.; Hattori, M.; Iijima, H. "Novel fluorinated polymer electrolyte for fuel cell", Polymer Preprints, Japan 2005, 54, 2, 4521–4522.

[75] T. Mashio, K. Malek, M. Eikerling, A. Ohma, H. Kanesaka, and K. Shinohara, J. Phys. Chem. C, 114, 13739 (2010).

[76] More, K. L. DOE Hydrogen Program Annual Progress Report, Nov 2005.

[77] Malevich, D., Jayasankar, B. R., Halliop, E., Pharoah, J. G., Peppley, B. a., & Karan, K. (2012). On the Determination of PEM Fuel Cell Catalyst Layer Resistance from Impedance Measurement in H2/N2 Cells. Journal of the Electrochemical Society, 159(12), F888–F895.

[78] Liu, Y., Murphy, M. W., Baker, D. R., Gu, W., Ji, C., Jorne, J., & Gasteiger, H. a. (2009). Proton Conduction and Oxygen Reduction Kinetics in PEM Fuel Cell Cathodes: Effects of Ionomer-to-Carbon Ratio and Relative Humidity. Journal of The Electrochemical Society, 156(8), B970.

[79] Young, a. P., Stumper, J., & Gyenge, E. (2009). Characterizing the Structural Degradation in a PEMFC Cathode Catalyst Layer: Carbon Corrosion. Journal of The Electrochemical Society, 156(8), B913.

[80] Levie, R. D. (1964). On porous electrodes. Electrochimica Acta, 9 (November 1963), 1231.

[81] Cimenti, M., Bessarabov, D., Tam, M., & Stumper, J. (2010). Investigation of Proton Transport in the Catalyst Layer of PEM Fuel Cells by Electrochemical Impedance Spectroscopy. ECS Transactions, 28(23), 147–157.

[82] Jang, J. H., Jeon, S., Cho, J. H., Kim, S.-K., Lee, S.-Y., Cho, E., … Lim, T.-H. (2009). Complex Capacitance Analysis of Ionic Resistance and Interfacial Capacitance in

PEMFC and DMFC Catalyst Layers. Journal of The Electrochemical Society, 156(11), B1293.

[83] Boyer, C., Gamburzev, S., Velev, O., Srinivasan, S., & Appleby, A. J. (1998). Measurements of proton conductivity in the active layer of PEM fuel cell gas diffusion electrodes. Science, 43(24).

[84] Transactions, E. C. S., & Society, T. E. (2011). Understanding the Ionomer Structure and the Proton Conduction Mechanism in PEFC Catalyst Layer: Adsorbed Nafion on Model Substrate Devproshad K. Paul, 41(1), 1393–1406.

[85] Siroma, Z., Kakitsubo, R., Fujiwara, N., Ioroi, T., Yamazaki, S., & Yasuda, K. (2009). Depression of proton conductivity in recast Nafion® film measured on flat substrate. Journal of Power Sources, 189(2), 994–998.

[86] Eastman, S. A.; Kim, S.; Page, K. A.; Rowe, B. W.; Kang, S.; Soles, C. L. Effect of Confinement on Structure, Water Solubility, and Water Transport in Nafion Thin Films. Macromolecules 2012, 45, 7920−7930.

[87] Krtil, P.; Trojanek, A.; Samec, Z. J. Kinetics of Water Sorption in Nafion Thin Films - Quartz Crystal Microbalance Study, Phys. Chem. B 2001, 105 (33), 7979−7983.

[88] Dishari, S. K.; Hickner, M. A. Antiplasticization and Water Uptake of Nafion Thin Films. ACS Macro Lett. 2012, 291−295.

[89] Fairbridge, J. R. D. avnir. C. W. (1994). Recommendations for the characterization of porous solids. Pure&Appl. Chem., 66(8), 1739–1758.

[90] K.S.W. Sing, D.H. Everett, R.A.W. Haul, L. Moscou, R.A. Pierotti, J. Rouquerol and T. Siemieniewska, Pure and Appl. Chem., vo1.57, n04, pp 603-919, 1985.

[91] IUPAC "Manual on Catalyst Characterization", J. Haber, Pure and Appl. Chem., vo1.63, pp. 1227-1246, 1991.

[92] Fagerlund, G. Determination of specific surface by the BET method. Matériaux et Construction, 1973, Vol.6(3), pp.239-245

[93] S. Brunauer, P. Emmett and E. Teller, J. Amer. Chem. Soc., 60, 309 (1938).

[94] Wu, J., Yuan, X., Wang, H., Blanco, M., Martin, J., & Zhang, J. (2008). Diagnostic tools in PEM fuel cell research: Part I Electrochemical techniques. International Journal of Hydrogen Energy, 33(6), 1735–1746.

[95] Mench, M. (2008). Fuel Cell Engines.

[96] I. D. Raistrick. (1990). Impedance studies of porous electrodes. Electrochimica Acta, 35(10), 1579–1586.

[97] Gomadam, P. M., & Weidner, J. W. (2005). Analysis of electrochemical impedance spectroscopy in proton exchange membrane fuel cells. International Journal of Energy Research, 29(12), 1133–1151.

[98] R. de Levie, in Advances in Electrochemistry and Electrochemical Engineering (Edited by P. Delahay and C. T. Tobias), Vol. 6, p. 329, Interscience, New York, 1967.

[99] Makharia, R., Mathias, M. F., & Baker, D. R. (2005). Measurement of Catalyst Layer Electrolyte Resistance in PEFCs Using Electrochemical Impedance Spectroscopy. Journal of The Electrochemical Society, 152(5), A970.

[100] M. Eikerling and A. A. Kornyshev, J. Electroanal. Chem., 475, 107. (1999).

[101] Neyerlin, K. C., Gu, W., Jorne, J., Clark, A., & Gasteiger, H. a. (2007). Cathode Catalyst Utilization for the ORR in a PEMFC. Journal of The Electrochemical Society, 154(2), B279.

[102] Lefebvre, M. C., Martin, R. B., & Pickup, P. G. (1999). Characterization of Ionic Conductivity Profiles within Proton Exchange Membrane Fuel Cell Gas Diffusion Electrodes by Impedance Spectroscopy, 2(6), 259–261.

[103] Höhne, G., Hemminger, W., & Flammersheim, H.-J. (2003). Differential Scanning Calorimetry.

[104] De Grotthuss, C., Ann Chim 58–54 (1806).

[105] Breslaul, B. R. & Miller, I. F. A Hydrodynamic Model for Electroosmosis. Ind. Eng. Chem. Fundam 10, (1971).

[106] Kreuer, K. D., Rabenau, A. & Weppner, W. Vehicle mechanism, a new model for the interpretation of the conductivity of fast proton conductors. Angew. Chem.-Int. Edit. Engl. 21, 208-209 (1982).

[107] Zawodzinski, T. A., Derouin, C., Radzinski, S., Sherman, R. J., Smith, V. T., Springer, T. E., & Gottesfeld, S. (1993). Water Uptake by and Transport Through Nafion 117 Membranes. Journal of The Electrochemical Society, 140(4), 1041.

[108] M. C. Lefebvre, R. B. Martin, and P. G. Pickup, Electrochem. Solid-State Lett., 2, 259 (1999).

[109] Gu, W., Baker, D. R., Liu, Y., & Gasteiger, H. A. (2010). Proton exchange membrane fuel cell (PEMFC) down-the-channel performance model. Handbook of Fuel Cells-Fundamentals, Technologies and Applications.

[110] Paul, D. K., Fraser, A., & Karan, K. (2011). Towards the understanding of proton conduction mechanism in PEMFC catalyst layer: Conductivity of adsorbed Nafion films. Electrochemistry Communications, 13(8), 774–777.

[111] Iden, H., Ohma, A., & Shinohara, K. (2009). Analysis of Proton Transport in Pseudo Catalyst Layers. Journal of The Electrochemical Society, 156(9), B1078.

[112] K. Ikeda, N. Nonoyama, and Y. Ikogi, Meet. Abstr. - Electrochem. Soc., 902, 975(2009).

[113] Eloot, K., & Debuyck, F. (1995). Calculation of the impedance of noncylindrical pores Part I : Introduction of a matrix calculation method. Journal of Applied Electrochemistry, 25, 326–333.

[114] Eloot, K., & Debuyck, F. (1995). Calculation of the impedance of noncylindrical pores Part II : Experimental verification on pores drilled into stainless steel. Journal of Applied Electrochemistry, 25, 334–339.

[115] M. Uchida, Y. Aoyama, N. Eda, A. Ohta, J. Electrochem. Soc. 142 (1995) 4143.

[116] A. Lasia, Modern Aspects of Electrochemistry, R. E. White, B. E. Conway, and J. O. Bockris, Editors, v. 32, p. 143, Plenum Press, New York (1999).

[117] A. Lasia, in Modern Aspects of Electrochemistry, R. E. White, B. E. Conway, and J. O. Bockris, Editors, v. 32, p. 143, Plenum Press, New York (1999).

[118] J. Bisquert, Phys. Chem. Chem. Phys., 2, 1485 (2000).

[119] S. J., & Yandrasits, M. a. (2006). Proton Exchange Membranes for Fuel Cell Applications. Journal of Macromolecular Science, Part C: Polymer Reviews, 46(3), 219–244.

[120] Leofanti, G., Padovan, M., Tozzola, G., & Venturelli, B. (1998). Surface area and pore texture of catalysts. Catalysis Today, 41(1-3), 207–219.

[121] Kaneko, K. (1994). Determination of pore size and pore size distribution 1 . Adsorbents and catalysts. Journal of Membrane Science, 96(94), 59–89.

[122] Watanabe, M., Tomikawa, M., & Motoo, S. (1985). Experimental analysis of the reaction layer structure in a gas diffusion electrode. Journal of Electroanalytical Chemistry and Interfacial Electrochemistry, 195(1), 81–93.

[123] Bai, Y. (2011). Proton Conductivity and Partial Molar Volume of Different Polymer Electrolyte Membranes. Transactions, E C S Society, The Electrochemical, 41(1), 1545–1553.

[124] Bai, Yujia, "Membrane and Performance Study in Polymer Electrolyte Membrane Fuel Cells and Hydrogen Bromine Redox Flow Batteries." PhD diss., University of Tennessee, 2013.

[125] Soboleva, T., Malek, K., Xie, Z., Navessin, T., & Holdcroft, S. (2011). PEMFC catalyst layers: the role of micropores and mesopores on water sorption and fuel cell activity. ACS Applied Materials & Interfaces, 3(6), 1827–37.

[126] Bass, M., Berman, A., Singh, A., Konovalov, O., & Freger, V. (2010). Surface structure of Nafion in vapor and liquid. The Journal of Physical Chemistry. B, 114(11), 3784–90.

[127] Sun, Che-nan. (2011). Study of Transport Properties and Microstructure of Materials for Polymer Electrolyte Fuel Cells. Doctor of Philosophy, Case Western Reserve University, Materials Science and Engineering.

[128] Iden, H., Sato, K., Ohma, A., & Shinohara, K. (2011). Relationship among Microstructure, Ionomer Property and Proton Transport in Pseudo Catalyst Layers. Journal of The Electrochemical Society, 158(8), B987.

[129] Modestino, M. A., Kusoglu, A., Hexemer, A., Weber, A. Z., & Segalman, R. A. (2012). Controlling Na fi on Structure and Properties via Wetting Interactions.

[130] Kusoglu, a., Kwong, a., Clark, K. T., Gunterman, H. P., & Weber, a. Z. (2012). Water Uptake of Fuel-Cell Catalyst Layers. Journal of the Electrochemical Society, 159(9), F530–F535.

[131] Kongkanand, A. (2011). Interfacial Water Transport Measurements in Nafion Thin Films Using a Quartz-Crystal Microbalance. The Journal of Physical Chemistry C, 115(22), 11318–11325.

[132] Xu, H., Kunz, H. R., & Fenton, J. M. (2007). Analysis of proton exchange membrane fuel cell polarization losses at elevated temperature 120°C and reduced relative humidity. Electrochimica Acta, 52(11), 3525–3533.

[133] Zhang, J., Tang, Y., Song, C., Xia, Z., Li, H., Wang, H., & Zhang, J. (2008). PEM fuel cell relative humidity (RH) and its effect on performance at high temperatures. Electrochimica Acta, 53(16), 5315–5321.

[134] Saleh, M. M., Okajima, T., Hayase, M., Kitamura, F., & Ohsaka, T. (2007). Exploring the effects of symmetrical and asymmetrical relative humidity on the performance of H2/air PEM fuel cell at different temperatures. Journal of Power Sources, 164(2), 503–509.

[135] Jordan, L. ., Shukla, a. ., Behrsing, T., Avery, N. ., Muddle, B. ., & Forsyth, M. (2000). Diffusion layer parameters influencing optimal fuel cell performance. Journal of Power Sources, 86(1-2), 250–254.

[136] Litster, S., Sinton, D., & Djilali, N. (2006). Ex situ visualization of liquid water transport in PEM fuel cell gas diffusion layers. Journal of Power Sources, 154(1), 95–105.

[137] V.A. Paganin, E.A. Ticianelli, E.R. Gonzalez, J. Appl. Electrochem. 26 (1996) 297.

[138] E. Antolini, L. Giorgi, A. Pozio, E. Passalacqua, J. Power Sources 77 (1999) 36142.

[139] Neyerlin, K. C., Gu, W., Jorne, J., & Gasteiger, H. a. (2006). Determination of Catalyst Unique Parameters for the Oxygen Reduction Reaction in a PEMFC. Journal of The Electrochemical Society, 153(10), A1955.

[140] C. K. Mittelsteadt and H. Liu, in Handbook of Fuel Cells, Vol. 5, W. Vielstich, H. A. Gasteiger, and H. Yokokama, Editors, p. 345, Chap. 23, John Wiley & Sons, Chichester, UK (2009).

[141] Y.-H. Lai and D. A. Dillard, in Handbook of Fuel Cells, Vol. 5,W. Vielstich, H. A. Gasteiger, and H. Yokokama, Editors, p. 403, Chap. 27, JohnWiley & Sons, Chichester, UK (2009).

[142] M. Doyle and G. Rajendran, in Handbook of Fuel Cells: Fundamentals, Technology, and Applications, Vol. 3,W. Vielstich, A. Lamm, and H. A. Gasteiger, Editors, Chap. 34, p. 18, John Wiley & Sons, New York (2003).

[143] Beuscher, U.; Cleghorn, S. J. C.; Johnson, W. B. International Journal of Energy Research 2005, 29, 1103.

[144] R. F. Savinell, E. Yeager, D. Tryk, U. Landau, J. S. Wainright, D. Weng, K. Lux, M. Litt, and C. Rogers, This Journal, 141, L46 (1994).

[145] C. A. Wilkie, J. R. Thomsen, and M. L. Mittleman, J. Appl. Sci., 42, 901 (1991).

[146] de Almeida, S. H.; Kawano, Y. Journal of Thermal Analysis and Calorimetry 1999, 58, 569.

[147] H. Tashino, H. Hara, E. Hirasawa, S. Kutsumizu and S. Yano, J. Appl. Polym. Sci., 55 (1995) 131.

[148] K. Tadano, E. Hirasawa, H. Yamamoto and S. Yano, Macromolecules, 22 (1989) 226.

[149] E. Hirasawa, Y. Yamamoto, K. Tadano and S. Yano, J. Appl. Polym. Sci., 42 (1991) 351.

[150] T. Kyu, M. Hashiyama and A. Eisenberg, Can. J. Chem., 61 (1983) 680.

[151] Tarmyshov, K. B., & Müller-Plathe, F. (2007). Interface between platinum(111) and liquid isopropanol (2-propanol): a model for molecular dynamics studies. The Journal of Chemical Physics, 126(7), 074702.

[152] S. Meng, E. G. Wang, and S. W. Gao, J. Chem. Phys 119, 7617 (2003).

[153] S. Meng, E. G. Wang, and S. W. Gao, Phys. Rev. B 69, 195404 (2004).

[154] J. Plsek, P. Hruby, K. Nikiforov, and Z. Knor, Appl. Surf. Sci 252, 1553 (2005).

[155] G. Lin, T.V. Nguyen. J. Electrochem. Soc., 153 (2006), pp. A372–A382.

Vita

Luyue Li was born in Dalian, China. She attended Waldschule elementary school in Geesthacht, Germany from 1993-1996 and Shiyan Elementary School in Dalian, China from 1996-1999. She then continued to Dalian No. 37 middle school and Yuming high school. After graduation, she joined the chemical engineering department of Dalian University of Technology (DUT) in 2005. She received her Bachelor degree in chemical engineering and minor in English in 2010. In August 2010, she started to pursue her PhD degree in Chemical Engineering at University of Tennessee, Knoxville. She joined Dr. Thomas Zawodzinski's research group and has worked in the realm of electrochemistry since 2010.